Advanced Photomask Characterisation for Microlithography

Martin McCallum

A thesis submitted for the degree of Doctor of Philosophy.
The University of Edinburgh.
2006

Abstract

IC manufacturing has been driven, almost since its inception, by the ability to pattern the required circuit features. Over the past forty to fifty years of IC production the industry has built increasingly complex exposure tools and developed techniques that have allowed circuit features to be produced that have dimensions significantly lower than the wavelength of the light used to pattern them. Exposure tool development has been market driven, with several large companies investing heavily in research and development to produce machines that use rapidly decreasing wavelengths of light while increasing the numerical aperture of their lenses. Development of optical techniques has been primarily driven by a combination of both academia and the IC manufacturers. Often the methods developed are both cost effective and highly innovative driving the image formation close to the physical limit. These methods have concentrated in two main areas: modified illumination and advanced photomasks.

This thesis addresses the characterisation of these advanced masks. There are many techniques published that produce advanced masks, but this work deals with two of the primary ones, advanced binary masks and alternating phase-shift masks (altPSM). The work covered studies the methods of extracting the three dimensional structure of these masks and uses simulation to show what effect this has upon the waves propagating through them.

To provide a production process that is robust to day to day instabilities, the mask pattern must be as accurate as possible because defects are typically amplified in the imaging system. The thesis deals with the way in which mask inspection systems image masks and the differences inherent between the way they observe defects and the way that these defects are reproduced when printed on IC patterns. This is a vitally important component of manufacturing as the inspection tool must be calibrated to replicate a much more complex and expensive exposure tool. It is shown through simulation that smaller defects at the centre of a space rather than at the edge result in the limits of CD tolerance being reached and that

the most sensitive position for a defect is not at the edge or centre of the space but rather at a position between these two.

With imaging close to the theoretical limits, there is a non linear transfer of dimensional errors to the wafer. This makes it vitally important that the actual dimension on the photomask is known and on target. However the dimensions on these masks are below that normally imaged by conventional optical dimension measurement systems. The alternative used on wafers, that of scanning electron microscopy (SEM) is not reliable on masks as they have a conducting surface on an insulator. This very structure does however make them suitable for measurement with novel electrical structures. The thesis explores the potential of this technique and compares its accuracy to that of conventional optical and SEM systems showing a 99% correlation. This novel approach to electrical measurement of the mask is then taken forward to explore other possible applications of electrical measurements on photomasks, including overlay, where accuracy with much higher resolution than optical verniers is demonstrated.

Declaration of originality

I hereby declare that the research recorded in this thesis and the thesis itself was composed and originated entirely by myself in the Department of Electronics and Electrical Engineering at The University of Edinburgh.

List your exceptions here and sign before your printed name.

Acknowledgements

The first two people I would like to thank are Dr Tom Stevenson and Professor Anthony Walton, without whom none of this would have happened. I would also like to thank everyone I've worked with at the Scottish Microelectronics Centre especially Stewart Smith, Andreas Tsiamis and Alan Ross.

I have to thank the many people I've collaborated with in industry during the course of my research, most especially to Andrew Hourd of Compugraphics who always goes above and beyond the call of duty. Also to Masaomi Kameyama at Nikon Corp, Kevin Lucas of Synopsys, Peter Zandbergen of NXP, Ron Gordon of ORA, Gil Shelden of Shelden Consulting, Paul Harris of Brewer Science, Tom Pistor at Panoramic Technologies, John Petersen of PAL, Martin Fallon at National Semiconductor and Dave Wilson at Freescale.

The most important person I have to thank is Jane, she lets me off the hook to travel the world (both socially and on business) while keeping us all together as a family and holding a job down. I really do love you that much. To Neil and Anna, you are both my world. To Mum and Dad for giving up so much to get me where I am today.

This is dedicated to both my father and to Alasdair, neither of whom got the chance to do what I've been lucky enough to do.

Acronyms and abbreviations

AFM	Atomic Force Microscope/Microscopy
ARC	Anti-Reflective Coating
ArF	Argon Flouride
AltPSM	Alternating aperture Phase Shifting Mask
CAD	Computer Aided Design
CD	Critical Dimension
CD-SEM	Critical Dimension Scanning Electron Microscopy
DOF	Depth of Focus
DUT	Device Under Test
DUV	Deep Ultra Violet
E-BEAM	Electron Beam
ECD	Electrical Critical Dimension
EMF	Electro-Magnetic Field
FDTD	Finite Difference Time Domain
IC	Integrated Circuit
ICP	Inductively Coupled Plasma
ITRS	International Technology Roadmap for Semiconductors
IPE	Image Placement Error
KrF	Krypton Flouride

MEEF	Mask Error Enhancement Factor
MEMS	Micro-Mechanical Electromechanical Systems
NA	Numerical Aperture
OAI	Off Axis Illumination
OPC	Optical Proximity Correction
PSM	Phase Shifting Mask
RET	Resolution Enhancement Techniques
RIE	Reactive Ion Etch
ROI	Return On Investment
SEM	Scanning Electron Microscope/Microscopy
SMU	Source Monitor Units
UV	Ultra Violet

TABLE OF CONTENTS

Chapter 1
Introduction

This chapter presents a brief examination of the history of microelectronics from the first transistors and integrated circuits to the ever increasing complexity predicted by Moore's law and the associated technology roadmaps. It goes on to introduce the concepts behind the use of microelectronic test structures for process control and characterisation. The chapter ends with a description of the thesis structure and the contents of the chapters that follow.

1.1) Background

The adoption and use of semiconductor integrated circuits has been one of the most startling of these developments in the past fifty years. We have gone from early work such as the work of Shockley to manufacture simple junctions, for resistors or diodes, to complicated three dimensional structures more complex than any skyscraper building. The ease of applicability of the functions provided by these devices has driven their success. Previous to their introduction some of the functions were performed by large machines that occupied entire rooms and were constructed from miles of cables linking racks of valves. What the introduction of semiconductor IC's offered was this in miniature. The valves replaced by transistors, the cables by conductive lines. This vast reduction in the area required for a circuit to be formed not only enabled the entire microelectronics industry but also set the trend for area and dimension reduction that drives the industry to this day.

One of the most significant observers of this early trend was Gordon Moore of Intel who noted in 1965 [1] that there seemed to be a trend, that he forecast would continue, to double the number of devices in an IC every eighteen months. This has become known as Moore's Law. Since that time the IC manufacturing industry has been developing roadmaps [2] for itself in order to maintain this 'law'. These roadmaps started to be formalised in the early 1990's when the Semiconductor Industry Association (SIA), a group of IC device and tool manufacturing companies, organised and published the first National Roadmap for Semiconductors in 1992,

this was then updated in 1994 and 1997. A number of different geographical regions including Europe (EECA), Japan (EIAJ), Korea (KSIA) and Taiwan (TSIA) formed their own industry associations, these groups also published their own roadmaps, however in 1999 they finally all joined to produce and publish the first International Technical Roadmap for Semiconductors (ITRS). This works by having Technical Working Group's (TWG's) for each discipline (e.g. Lithography, Front End Processes, etc) that meet regularly on a regional basis and then once a year as an International TWG to finalise the roadmap for that year. Major updates are generally made every second year with intermediate revisions made in intervening years. The roadmap does not state which lithography solution should be used at each node, but instead suggests lithography technologies that are potential solutions. For each of these technologies it will also offer a guideline to the required features to be imaged at that node and their required tolerances. Expected requirements for major components of each technology, such as photoresist and mask capabilities and performance are also given. What the roadmap also does, is to attempt to highlights areas where problems may occur for each technology by showing where for each node and technology work is ongoing and solutions are known or likely, but also are unknown. One important side effect of the roadmap is to create a common language between competitor IC manufacturers who can use the nodes, dimensions and solutions suggested to talk to each other without disclosing proprietary information. However, it has also created an element of competition where many companies try to 'beat' the roadmap and therefore their competition.

Lithography is seen very much as the 'engine room' of the industry, being the area driving the so called Moore's Law. In the 1980's Ion Implantation processing machines were very much the largest and most expensive in wafer fabrication facilities. However in the 1990's, with the introduction of scanner and DUV technology, lithography tool overtook the implanters in terms of cost. The complexity of these tools also increased greatly especially when, around the turn of the millennium, the features being printed became smaller than the wavelength of light being used to print them. Much of this technology was driven by reduction of the illumination wavelength from 365nm (i-line) down to 248nm (KrF) and then 193nm (ArF). Increase of projection lens Numerical Aperture (NA) to undreamt of levels close to the theoretical maximum of 1.0 also greatly contributed. The use of these two items as the primary drivers can easily be understood if we consider the so called Rayleigh criteria for resolution:

$$\text{Resolution} = k_1 \frac{\lambda}{NA}$$

A key factor that must be considered is the effect of mask technology on the ability to image these small features. Two major areas must be considered: the first of these is the so-called Mask Error Enhancement Factor (MEEF) [3,4]. This is the name given to the non-linear transfer of dimension errors on the mask to the wafer. In imaging as we approach the theoretical limit, i.e. as k_1 approaches 0.25, the errors we see on the mask are in effect amplified. In normal microlithographic imaging we use a 4X reduction lens, this means that any error on the mask is also reduced by a factor of four. However, as we approach the theoretical limit for k_1 the error may only be reduced by a factor of 2 or less, or even amplified in some cases. This effect makes control of the feature dimension on mask extremely important [5]. In previous technologies the on mask dimensions were relatively large and could easily be measured with sufficient accuracy and repeatability with optical tools. However as the dimensions on mask have shrunk these tools are no longer capable. To overcome this industry initially began to use Scanning Electron Microscopes (SEM's) a tool they were familiar with on wafer metrology. Unfortunately the nature of photomasks, that of an ungrounded metal conductor on an insulator, made this a very difficult method to implement successfully as well as being relatively expensive since only the very few leading edge masks required this technique and the tool cost of an SEM can be an order of magnitude larger than its optical predecessor. A large part of the work of this thesis looks at the use of electrical dimension measurement on the mask, at a much cheaper alternative to the use of SEM's.

The second area of mask technology that has required investigation is related to the three dimensional nature of a mask. For situations where the Rayleigh k_1 factor was relatively large, e.g. above 0.7, the mask could be treated as a simple infinitely thin diffraction grating. But as we have further reduced the k_1 this assumption is no longer valid and we must now take into account losses within the mask due primarily to scatter. To understand this we must be able to gather information on the three dimensional nature of the mask substrate and pattern and use this to estimate and understand their effects upon imaging. In this thesis we will describe the use of Atomic Force Microscopy (AFM) to gather much of this and how this data can be input into software to estimate the effect upon the final image printed.

One of the overriding restrictions facing mask technology is related to economics. The estimated size of the yearly budget spend for all lithography equipment and supplies is around $13.5B, however of this only $3.7B is spent on mask technology [6]. The total number of masks produced each year is around 700,000, a figure that has remained steady for around 25 years [6]. Of these masks only a very small percentage, less than 1%, actually require the previously discussed mask metrology, however the cost of these tools is many millions of dollars and so it is very difficult to afford the required tools. Though this matter will not be discussed in this thesis, it may have a significant bearing on future technology and the work described here on electrical mask metrology may provide a significantly cheaper solution to maintain the economic balance.

1.2) Thesis plan

This section briefly outlines the contents of the chapters which follow. Chapter 2 reviews the theory behind microlithographic imaging and simulation. Chapters 3 to 4 investigate the methods of extracting three dimensional information from masks and how this can be used to simulate not only imaging but also mask defect metrology. In chapter 5 novel application of electrical sheet resistance and dimension measurement are explored together with other applications of electrical measurement. Finally, chapter 6 reviews the conclusions made in the previous chapters and suggests possibilities for future work.

Chapter 2. Background. The history behind single wavelength diffraction imaging and its development and application in IC's is discussed, together with how Resolution Enhancement Technologies (RET's) have been applied.

Chapter 3. Determining Mask Effects in Low k_1 Lithography. This chapter examines how AFM can be used to gather three dimensional information on a mask and how this can be used to calculate both the amplitude and phase of a light wave that propagates through it. This data can then be taken and an accurate aerial image from an imaging system calculated.

Chapter 4. Wavelength Dependant Mask Defect Inspection and Printing. One of the key problems in lithography is to ensure that no defects exist upon the master mask that will be reproduced on the IC's. This chapter deals with identifying, through simulation, what the

smallest allowable defect size is in Alternating Aperture Phase-Shifting Masks (altPSM) and how its position relative to circuit pattern features effects this. Defect detection is normally not done at the actinic wavelength (the wavelength at which the mask is used for imaging) and also in 1x imaging systems rather than the 4x reduction stepper or scanner. The difference in how these defects are observed by these defect inspection tools is calculated.

Chapter 5. Electrical Characterisation of Binary and Alternating Aperture Phase-Shifting Masks. The need to understand exactly what are the actual characteristics of dimension and position of features on the mask is becoming increasingly important. In this chapter we will deal with using relatively low cost electrical techniques to establish what these characteristics are.

Chapter 6. Conclusions and Future Work. In this chapter the conclusions drawn from the work reported in the preceding chapters are reviewed. Suggestions for future work on the topics covered in this thesis are also made.

References

[1] G. E. Moore, "Cramming more components onto integrated circuits", Vol. 38, No. 8, Electronics (1965)

[2] International Technology Roadmap for Semiconductors: 2005 Edition. SEMATECH, Austin, TX, USA, (2005). http://www.itrs.net/.

[3] W. Maurer, D. Samuels, "Masks for 0.25-micron lithography", Photomask and X-Ray Mask Technology, SPIE Vol. 2254 (1994), pp. 26-35.

[4] W.Maurer, "Mask specifications for 193 nm lithography", 16th Annual BACUS Symposium on Photomask Technology and Management, SPIE Vol. 2884 (1996), pp. 562-571.

[5] W. Conley, X. Shi, M. Hankinson, M. V. Dusa, R. J. Socha, C. Garza, "Understanding the impact of full-field mask error factor", SPIE Vol. 4000 (2000)

[6] G.V. Shelden, S. Hector, "Mask industry assessment: 2005", SPIE Vol. 5992 (2005)

Chapter 2
Microlithography Development

2.1) Early photolithography

2.1.1) Contact printing

Patterning of IC's has been critical to the development of the microelectronics industry. The earliest devices were patterned using direct contact printing where the mask was in direct contact with the photosensitive material (photoresist) to be imaged and coherent broadband illumination light passed through. This is basically a practical application of Fresnel diffraction gratings [1]. This was used to produce features down to 2μm and has continued in use, mainly in labs for development, to this day. However this technique had two main problems: the first was damage to the photoresist and the second that defects easily became attached to the surface of the mask and would then cause pattern errors on subsequent wafers. These defects were principally from the chemical reaction that took place when the photosensitive polymer was exposed, but other sources included the environment which was much less clean than we see in labs and production facilities today. This technique also relied upon the mask to be correctly patterned in the first place. Contact printing was used for a few years until proximity printing was developed to overcome the damage and defect problems.

In recent years a number of technologies have once again proposed contact printing, the first of these is nanoimprint lithography [2] where a master mask, which has three dimensional topography is brought into close proximity to a wafer. A photosensitive polymer is then introduced into the gap between the mask and wafer and exposed with UV light, the mask is then removed and the patterned polymer left. This technology has similar problems with defects and damage to early contact printing and the additional problem that the mask is effectively a mold, so the depth of each feature on the mask becomes critical as this will be reproduced on the wafer. However, this is a very promising technology for applications in packaging and Micro-Mechanical Electromechanical Systems (MEMS) devices. The second application is in plasmonic imaging [3,4]. In this application UV sources are used to illuminate a mask which

includes a plasmon mask. The work to date has used silver and is very interesting but remains very much in the lab at present.

2.1.2) Proximity printing

Work in the mid 1960's introduced a gap, typically between 20 to 50μm, between the mask and photoresist in order to overcome the problems of damage and defects. This was known as proximity printing and is shown in figure 2.1. It should be considered that due to diffraction the resolution of proximity systems is actually inferior to that of contact printing. However the defect transfer problem had become so critical that this technique was readily adopted in order to overcome this. To help overcome the resolution problems encountered people began for the first time to modify the illumination, using a less coherent light source leading to actual overall improvements in resolution moving the technology below 2μm.

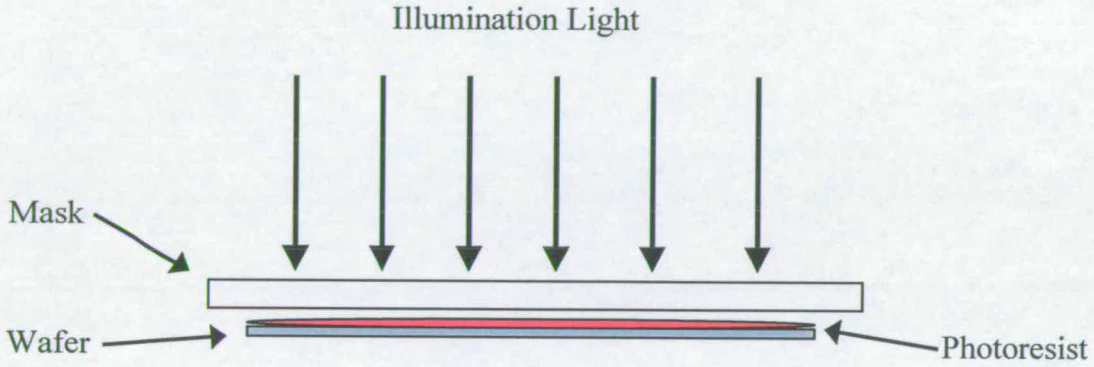

Figure 2.1. Schematic of a proximity printing system.

Proximity was replaced in around 1974 when optical scanning tools were introduced, that continued to use 1x masks but had the wafer a considerable distance from the mask.

2.1.3) 1x Projection Scanners

These tools were first developed and commercialised by Perkin Elmer. To maintain the imaging of the time a 1x all refractive projection system was designed and adopted [5]. However to overcome the large size of optics that would be required to expose the whole wafer at one time they actually only illuminated a portion of the mask at any one time and used scanning to print the whole wafer as is shown in figure 2.2. This technique revolutionised the industry and is still in use today in many older production lines. The exposure systems sold over the years were

primarily developed to cope with the larger wafer sizes being utilised by the industry until the introduction of six inch wafers when wafer steppers overtook them in popularity.

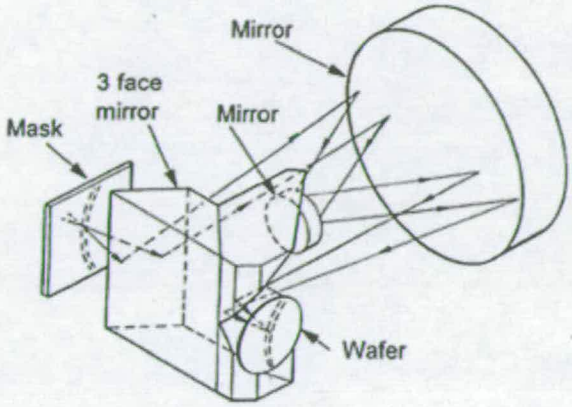

Figure 2.2. 1x Projection scanner projection system.

It is worth considering two of the major developments that these tools brought to the industry that we continue to use to this day. The first is their scanning mechanism where only a portion of the mask was exposed at any one time. This was later developed into the step-and-scan systems we see today that will be discussed later in this chapter. The second is their application of wavelength selection. These tools use a Mercury arc lamp as their illumination source. These produced not a wide band of constant illumination but rather a series of bright peaks from discrete wavelengths listed in table 2.1. The majority of exposures with this type of tool did not use any type of wavelength filtering so all illumination wavelengths were used. However, it was realised that if it was possible to filter out the higher wavelengths and use only low wavelengths the resolution would improve [6]. This was also made easier due to the catadioptic nature of the lens design where chromatic aberrations can be corrected for much more easily than in refractive lens elements. These tools then became the workhorses for development of what became deep ultra-violet (DUV) lithography.

Line label	Wavelength	Location in the electromagnetic spectrum
g-line	435.8nm	Visible
h-line	404.7nm	Visible
i-line	365nm	Mid-ultraviolet
DUV	240-255nm	Deep-ultraviolet (DUV)

Table 2.1. Illumination spectrum of Mercury used in lithography.

2.2) Reduction Photolithography

2.2.1) Step and Repeat Reduction Lithography

Around 1978 the first step-and-repeat systems that utilised a reduction imaging systems were introduced [7]. These systems revolutionised the entire industry through the introduction of two major concepts: the first of these is the use of a step-and-repeat stage. All previous systems had imaged the whole wafer, each device on the wafer having an equivalent master on the mask that was then reproduced. The step-and-repeater, or as it has become known stepper, used the same master pattern that was imaged on the wafer in what became know as an exposure field that only covered a small portion of the wafer. The stage on which the wafer was held then stepped to the next field and an exposure took place, this being repeated until the entire wafer had been exposed. The second concept was to use a reduction imaging system. Until all this time the features on the mask had to be manufactured at the same dimension as that desired on the wafer. Through the use of reduction imaging the features on the mask could be made much more easily as these could be 10x or 5x larger than those on the wafer dependant upon the reduction lens design used. Any error on the dimensions on mask was also greatly reduced through this reduction. Probably the largest benefit was the tolerance created to on-mask defects. Relatively large defects could be tolerated on the mask as they would not be reproduced on the wafer. This was further strengthened through the invention of the pellicle [8], where a thin polyvinyl acetal film was held by a frame a defined distance away from the surface of the mask. Any defects that fell upon the pellicle would then be out of focus. This significant invention was also applied to the 1x projection scanners that were still in production.

Initially many companies developed their own steppers, including Philips [9], Thompson CSF [10] and IBM [11], but the first to be commercialised was by the GCA Corporation of North Andover, Massachusetts, USA [12]. These first GCA tools had a lens numerical aperture (NA) of 0.28, used g-line illumination and had a 10x reduction lens that gave an exposure field of 10mm x 10mm. The market for these systems relatively quickly became substantial and a number of new companies developed and sold wafer steppers, these included Nikon and Canon of Japan, SVGL and Ultratech of the US and ASML of the Netherlands who commercialised the Philips stepper [9]. The majority of these companies quickly adopted g-line illumination and a 5x reduction lens that combined with a five inch mask to produce an exposure field of 15mm x 15mm. The main difference between the tools offered being in the lens NA and their ability to align to existing patterns on the wafer. However, most used the same basic design form shown in figure 2.3.

Over the next few years one of the most significant features was the move from five inch to six inch masks. While keeping the 5x reduction ratio lenses were designed to increase the exposure field size from 15 x 15mm to 20 x 20mm and then eventually 22 x 22mm. This was driven in the tool through higher quality lens manufacture and better design. The outcome of this was to improve the throughput of the exposure tools as less fields required to be exposed on any one wafer.

To satisfy the industry's need to resolve smaller and smaller features, wafer stepper technology developed changing down to i-line in the late 1980's and then to DUV illumination wavelengths in the mid 1990's, the latter initially with mercury arc lamps but then to excimer KrF lasers [13,14]. An interesting side note is that DUV lithography, and in particular the novel chemically amplified photoresists it required, were developed not on stepper technology but on 1x projection scanners [6,15,16].

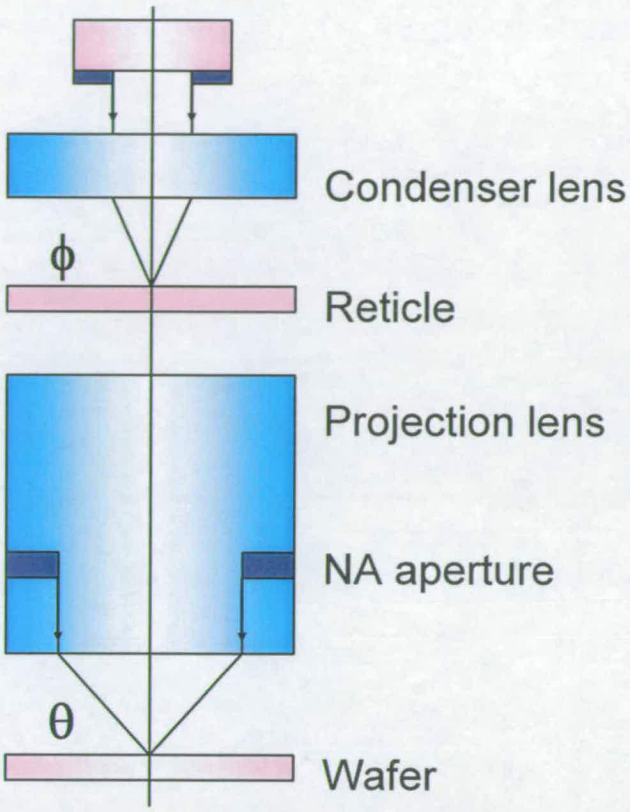

Figure 2.3. Schematic of a reduction wafer stepper.

2.2.2) Step and Scan Technology

In parallel to wavelength reduction the lens NA's were increasing, this put a great deal of pressure on lens technology from design, manufacturing and materials basis. The economics of this meant that even if the desired NA's of over 0.6 could be achieved the lens would be too expensive for IC manufacturers to buy and gain any return on investment (ROI). To overcome this the scanning technique utilised in 1x projection systems [5], was taken and combined with step-and-repeat technology. The advantage this had was to reduce the size of lens required by about one third as can be seen in figure 2.4. This allowed the lenses to be made in a cost-effective way.

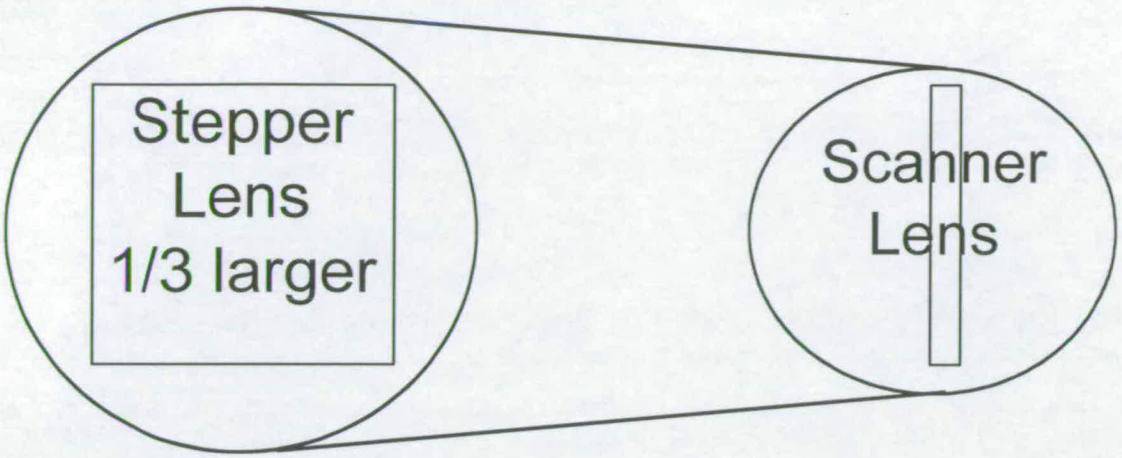

Figure 2.4. Comparison of lens size for a stepper and scanner.

The mask was then scanned in one direction above the exposure slit while the wafer below the projection lens was scanned in the opposite sense. After this exposure field was complete the wafer stage stepped to the next field and the scan process was repeated, a schematic of this scanning is seen in figure 2.5. These tools have become known by the moniker scanners.

One important factor that must be discussed was the magnification and field size change that occurred with the introduction of scanner technology. As was discussed six inch masks were used in combination with 5x reduction to give 22mm fields. Scanners were introduced [17, 18, 19] with a reduction ratio of 4x with the same six inch masks. The length of the scan is limited by the length area of the mask while the width of the field is limited by the lens slit width, i.e. the lens design and manufacturing capability. Since this time lens technology has developed and lens NA's increased.

In the late 1990's development also started of a further reduction in wavelength, ArF lasers [20] producing light at 193.67nm were developed. These enabled development of ArF scanners where lens NA's have been developed above 0.9 and 65nm technology has been achieved [21,22]. Further to this immersion lithography has been developed where water has been put between the end of the projection lens and the wafer, this development has allowed lenses to manufactured with NA's significantly above 1.0 [23,24].

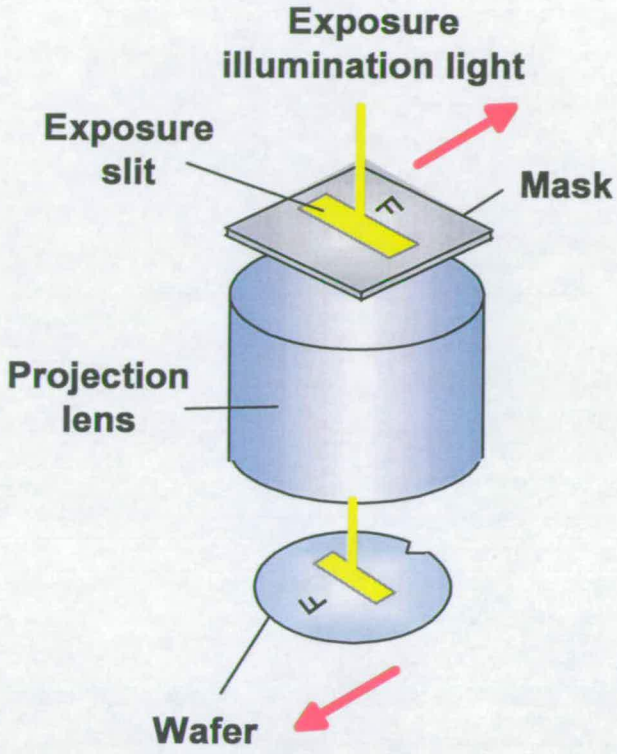

Figure 2.5. Schematic of the scanning exposure mechanism used in state-of-the art systems.

2.3) Resolution Enhancement Technology

It is important to note that it has not only been through the reduction in wavelength and increase in NA that resolution has been enhanced in photolithography. Much of the improvement, especially allowing reduction in the allowable k_1 of the Rayleigh resolution criteria, has been due to what is known as Resolution Enhancement Techniques (RET's). There are many of these but the most common are Off-Axis Illumination (OAI), Phase-Shifting Masks (PSM) and Optical Proximity Correction (OPC). OPC works by either changing the dimension or shape of the mask structure [25] or by adding sub-resolution structures to make a feature artificially 'dense' [26]. These work together to provide an actual imaging solution.

2.3.1) Off-Axis Illumination

In normal imaging we use three beams to create the interference that we require for imaging as can be seen in figure 2.6.

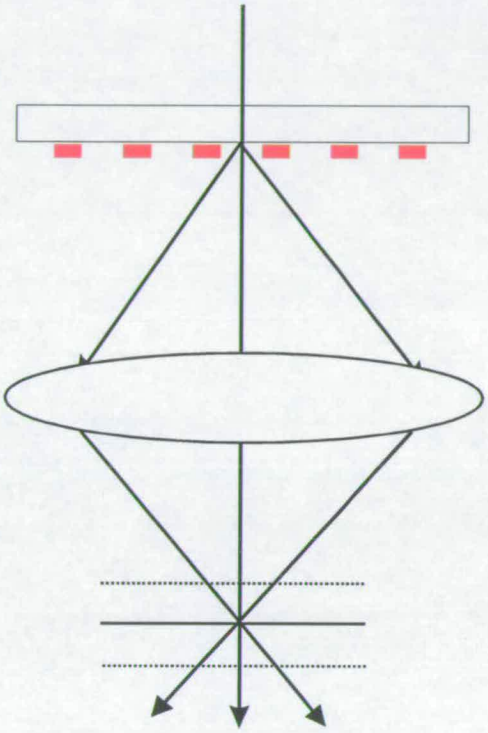

Figure 2.6. On axis imaging.

However as we wish to print smaller and smaller features the +1 and -1 order scattered light will not be gathered by the projection lens as can be seen on the left of figure 2.7. If we use non-zero angle incident light onto the mask (reticle) we can design this such that the 0 and +1 order diffracted rays can be gathered by the lens and imaging take place. This was the basic principle proposed for off-axis illumination [25].

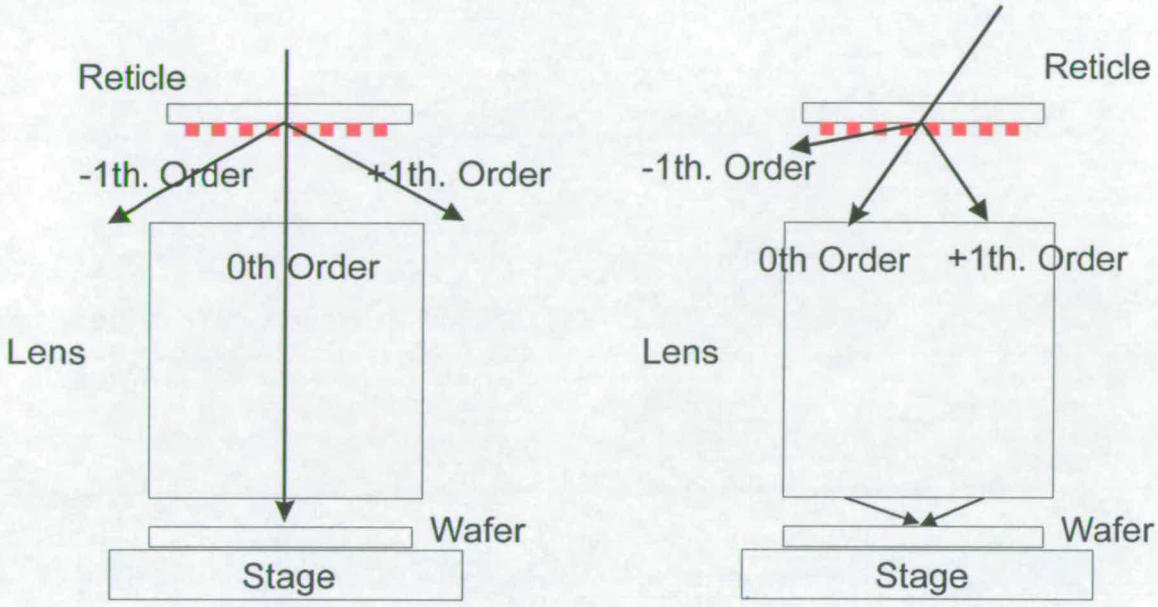

Figure 2.7. On-axis illumination (left) with $\pm 1^{st}$ order light not being gathered and off-axis illumination (right) showing 0 and +1 order light being gathered.

Off-axis illumination was quickly adopted by the exposure tool manufacturers and implemented into their production systems [28, 29, 30, 31]. Initially only simple annulus and quadropole illuminators as provided by tool suppliers were used, however their limitations were soon discovered and many IC manufacturers designed customised illumination schemes to suit their own IC patterns such as in [32, 33]. When designing these illumination schemes it is best to think of the entrance plane of the system as a frequency plane since we are dealing with a single wavelength. The frequencies can be considered analogous to the patterning features where dense features have a high frequency and isolated features a low frequency. As can be seen in figure 2.8 the dense features are at the edge of the frequency plane and have relatively low intensity while isolated features are very intense and in the centre of the plane. In this way by knowing where the diffraction orders of the pattern of interest fall, we can select these by having openings allowing this light through and prevent any interference from other frequencies where higher (or lower) intensity light my not allow interference to occur or may swamp the frequencies of interest.

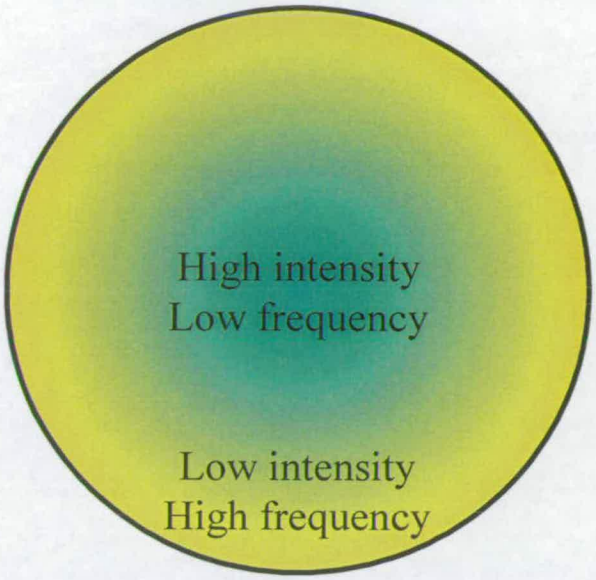

Figure 2.8. Frequency plane for a diffraction limited single wavelength imaging system.

2.3.2) Phase-Shifting Masks

The basic concept behind phase-shifting masks was first suggested by Levenson et al in 1982 [34]. With conventional binary (chrome on quartz) mask the light transmitted through the mask will produce a wavefront at the wafer that, as the imaging system approaches its limit, does not return to zero as can be seen in figure 2.9. If the intensity of the aerial image is considered, which is the square of the amplitude of the wavefront, it can be seen that some light appears in the area where a dark area should be. In the case of an alternating aperture phase-shifting mask (altPSM) however the direction of the wavefront through the shifted space is in the opposite sense to that of the unshifted space and has an area where the amplitude of the wavefront is zero as can be seen in figure 2.10. The aerial image of this then has an area of zero intensity. To produce a symmetrical aerial image it is important that the depth of the trench (d) in the shifted space is half an optical wavelength, this is obtained from:

$$d = \lambda/2(n - 1)$$

where λ is the illumination wavelength and n the refractive index of the glass material.

It is important to consider the slope of the aerial images produced from the binary and altPSM masks. The photoresist will sample the aerial image at a certain threshold, the steeper the slope of the aerial image the higher the contrast of the image that is being replicated and so the more

certainty there will be of an accurate dimension being obtained. The edges of process window are generally defined by the points where the contrast of the image is sufficiently poor that the resist can no longer accurately replicate the aerial image, this is generally in the defocus condition. By creating the dark area and providing steeper sloped aerial image, the process window can be extended with altPSM masks, in many cases creating a manufacturable process, as much more defocus can be tolerated. However, the depth of the shifted space must be tightly controlled otherwise the propagated wavefront from the shifted space will not be one hundred and eighty degrees out of phase and so the slope of the aerial image will be compromised.

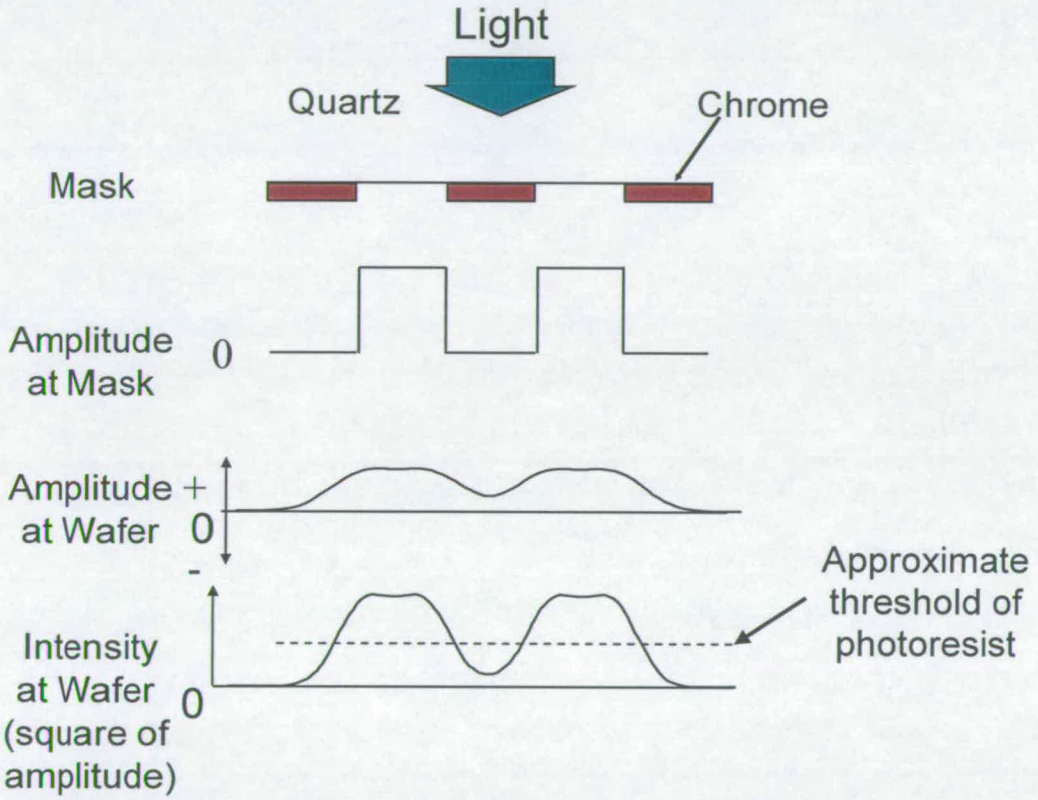

Figure 2.9. Wavefront propagation through an imaging system using a binary mask.

2.4) Conclusions

The development of photolithographic exposure tools for manufacturing of IC patterns has been highly successful over the past almost fifty years. During this time the features being printed have decreased in size from around 200μm, about four hundred times larger than the wavelength

of light being used to image them, to today's technology where features of around 50nm are being imaged using 193nm light. In this time there have been many advances in the exposure tools being used, where technology has advanced from simple contact printing to extremely complicated reduction systems where immersion is used to create systems with NA's larger than 1.0. It is important to bear in mind that the primary reason for the move to reduction systems was to help overcome the problems inherent in making high quality defect free masks. The fact that the reduction ratio also allowed more accurate feature replication, through minimising the effect of dimension errors on mask, should also not be taken lightly.

Today's technology has reached the level where, despite the reduction ratio's used, mask errors are being replicated and even magnified on mask. [35, 36]. When this is combined with new requirements for characterisation of the topography of a mask, the critical nature of mask as part of the imaging system can be understood. It is this requirement that has driven the research that is presented in this thesis.

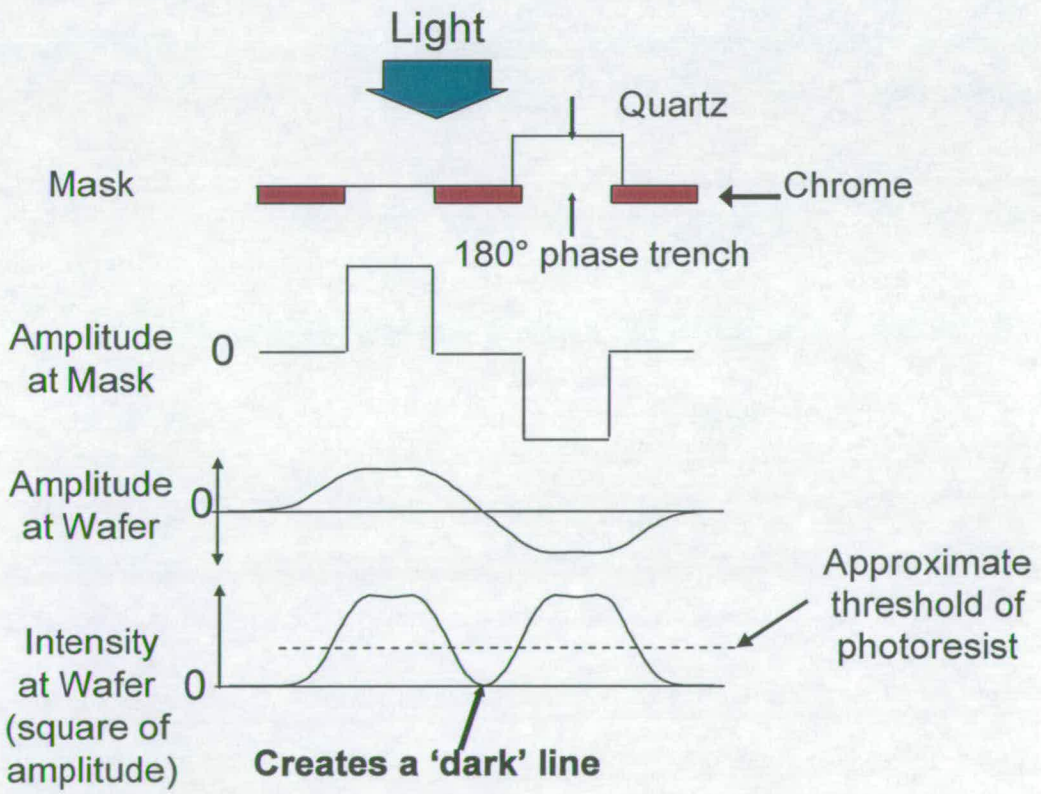

Figure 2.10. Wavefront propagation through an imaging system using an altPSM mask.

References

[1] M. Born, E. Wolf, "Principles of Optics", sixth edition, Cambridge University Press, (1980), pp. 401

[2] M. Colburn, S. Johnson, M. Stewart, S. Damle, T. Bailey, B.J. Choi, M. Wedlake, T. Michaelson, S.V. Sreenivasan, J. Ekerdt, C.G. Willson, "Step and Flash Imprint Lithography: A New Approach to High-Resolution Patterning", SPIE Vol. 3676, (1999), pp. 379-389

[3] J.B. Pendry, Physics Review Letters 86, 3966 (2000)

[4] D.O.S. Melville, R.J. Blaikie, "Super resolution imaging through a planar silver layer", Optics Express Vol. 13, No. 6, (2005) pp. 2127-2134

[5] A. Offner, "New concepts in projection mask aligners", Optical Engineering Vol. 14(2), (1975), pp. 130-132

[6] J.G. Maltabes, S.J. Holmes, J.R. Morrow, R.L. Barr, M.C. Hakey, G. Reynolds, W.R. Brunsvold, C.G. Willson, N.J. Clecak, S.A. MacDonald, H. Ito, "1X deep-UV lithography with chemical amplification for 1-micron DRAM production", SPIE Vol. 1262, (1990), pp. 2-7

[7] F. Klosterman, "A step-and-repeat camera system for photomasks", Philips Technical Review, Vol. 30, No. 3, (1969), pp.57-69

[8] Japanese patents JP19900151589 19900612, JP19900325272 19901129

[9] A. Bouwer, G. Bouwhuis, H. van Heek, S. Wittekoek, "The silicon repeater", Philips Technical Review, Vol. 37, No. 11/12, (1977), pp. 330-333

[10] M. Lacombat, A. Gerard, G. Dubroeucq, M. Chartier, "Photorepetition et projection directe", Rev. Tech. Thompson-CSF, Vol. 9, No. 2, (1977)

[11] J. Wilcyncski, "Optical step-and-repeat optical camera with dark field automatic alignment", Journal Vacuum Science Technology, Vol. 16, (1979), pp. 698-704

[12] J. Roussel, "Step-and-repeat wafer imaging", Solid State Technology, (1978), pp. 67-71

[13] Excimer Lasers, 2nd edition, Topics in Applied Physics, Vol. 30, ed. C.K. Rhodes, Springer Verlag, (1984)

[14] R.W. McCleary, P.J. Tompkins, M.D. Dunn, K.F. Walsh, J.F. Conway, R.P. Mueller, "Performance of a KrF excimer laser stepper", SPIE Vol. 922, (1988), pp. 396-399

[15] C.G. Willson, H. Ito, J.M. Frechet, F. Houlihan, "Chemical Amplification in the Design of Polymers for Resist Applications," International Union of Pure and Applied Chemistry, 28, 448 (1982).

[16] H. Ito, C.G. Willson, J.M. Frechet, M.J. Farrall, E. Eichler, "Synthesis of Poly(p-hydroxy-a-methylstyrene)," Polym.Prep., 25(1), (1984), pp. 158-159

[17] K. Suzuki, S. Wakamoto, K. Nishi, "KrF step and scan exposure system using higher NA projection lens", SPIE Vol. 2726, (1996), pp. 767-773

[18] M. can den Brink, H. Jaspar, S. Slonaker, P. Wijnhoven, F. Klaasen, "Step-and-scan and step-and-repeat, a technology comparison", SPIE Vol. 2726, (1996), pp. 734-753

[19] H. Sewell, "Advancing optical lithography using catadioptric projection optics and step and scan", SPIE Vol. 2726, (1996), pp. 707-720

[20] R. Sandstrom, "Argon fluoride excimer laser source for sub 0.25μm optical lithography", SPIE Vol. 1463, (1991), pp. 610-616

[21] N. Irie, M. Hamatani, M. Nei, "Progressive ArF exposure tool for 65nm node lithography", SPIE Vol. 5754, (2005) pp. 725-733

[22] R. Rubingh, M. Moers, M. Suddendorf, P. Vanoppen, A. Kisteman, M. Thier, V. Blahnik, E. Piper, "Lithographic performance of a dual stage 0.93NA ArF step and scan system", SPIE Vol. 5754, (2005), pp. 681-692

[23] M. Okumura, J. Ishikawa, M. Hamatani, M. Nei, "Mass production level ArF immersion exposure tool", SPIE Vol. 6154, (2006)

[24] H. Jasper, T. Modderman, M. van de Kerkhof, C. Wagner, J. Mulkens, W. de Boeij, E. van Setten, B. Kneer, "Immersion lithography with an ultra highNA inline catadioptric lens and a high transmission flexible polarization illumination system", SPIE Vol. 6154, (2006)

[25] Y. Nissan-Cohen, P. Frank, E.W. Balch, B. Thompson, K. Polasko, D.M. Brown, "Variable proximity corrections for submicron optical lithographic masks", 1987 Symposium on VLSI Technology, (1987).

[26] US Patent No. 5,242,770, (1992).

[27] D.L. Fehrs, H.B. Lovering, R.T. Scruton, "Illuminator modification of an optical aligner", KTI Microelectronics Seminar, (1989), pp. 217-230

[28] K. Kamon, T. Miyamoto, M. Yasuhito, H. Nagata, M. Tanaka, K. Horie, "Photolithography system using annular illumination", Japanese Journal of Applied Physics, Vol. 30, No. 11B, (1991), pp. 3021-3029

[29] N. Shiraishi, S. Hirukawa, V. Takeuchi, N. Magome, "New imaging techniques for 64M-DRAM", SPIE Vol. 1674, (1992), pp.741-752

[30] W. N. Partlo, P.J. Thompkins, P. G. Dewa, P.F. Michaloski, "Depth of focus and resolution enhancement for i-line and deep-UV lithography using annular illumination", SPIE Vol. 1927, (1993), pp. 137-157

[31] K. Tounai, H. Tanabe, H. Nozue, K. Kasama, "Resolution improvement with annular illumination", SPIE Vol. 1674, (1992), pp. 753-764

[32] S.Y. Chou, J.C. Lou, F.J. Liang, T.S. Gau, R.G. Liu, C.K. Chen, C.M Lai, "Customized illumination aperture filter design for through-pitch focus latitude enhancement of deep submicron contact hole printing", SPIE JM3 01(03), (2002), pp. 296-306

[33] F. Weisbuch, S. Warrick, W. Conley, J. Depre, "Assessment of 5-pole illumination for 65nm-node contact holes", SPIE Vol. 5754, (2005), pp. 1405-1416

[34] M.D. Levenson, N.S. Visanathan, R.A. Simpson, "Improving resolution in photolithography with a phase-shifting mask", IEEE Transactions on Electron Devices, Vol ED-29, No. 12, pp.1828-1836, 1982.

[35] W. Maurer, D. Samuels, "Masks for 0.25-micron lithography", Photomask and X-Ray Mask Technology, SPIE Vol. 2254 (1994), pp. 26-35.

[36] W.Maurer, "Mask specifications for 193 nm lithography", 16th Annual BACUS Symposium on Photomask Technology and Management, SPIE Vol. 2884 (1996), pp. 562-571.

Chapter 3
Determining Mask Effects in Low k_1 Lithography

3.1) Introduction

In order to work in the region where the k_1 of the Rayleigh criteria is below 0.5 a number of advanced imaging techniques must be used, the most significant and widely used of these being phase-shift masks (PSM). Initial work with alternating aperture phase-shift masks (altPSM) revealed many unexpected results that could not be fully explained through existing understanding of lithography. Further investigation revealed that the mask may no longer be treated as a planar two dimensional surface and it is necessary to model the topography with a more rigorous approach involving the solution of Maxwell's equations at the mask, in order to explain the observed effects.

3.2) Mask Topography

Classically alternating aperture phase-shift masks have been considered to be fairly discreet structures with perpendicular sidewalls and right-angled corners. However, as is known from the production of IC's, drawings do not often resemble reality; this also is the case with masks. To try and provide models that would give a good representation of actual masks, an alternating aperture phase-shift mask built by a commercial mask supplier for a 248nm 4x reduction scanner was examined. The mask was built using the 0°/180° phase differential technique with the trench for the 180° achieved in an Reactive Ion Etch (RIE) system. The mask then received a wet etch to reduce the effects of scattering from corners previously reported by a number of researchers [1, 2]. In order to examine the mask structure in a non-destructive manner that would still allow its use for lithography after investigation atomic force microscopy (AFM) was used. There are a number of commercial tools available to do this; in this case the tool used was a Veeco with a 0.18μm 'boot' tip [3]. This 'boot' tip on the Veeco tool has a flared end, allowing information to

be gathered on the profile of the mask to build an accurate picture of the wall angles and any undercuts. However it is not possible to measure any undercut between chrome and quartz but accurate measurement of the actual depth of each trench in the patterned area is achieved. This information is important as it is normal to assess the achieved phase through measurement of a metrology structure on the mask. This structure is limited to a minimum dimension of 2μm on mask which only represents structure of 0.5μm on wafer compared to the 0.1μm features of interest (given a 4x magnification system.) It is known from wafer processing that the difference in topography from 2μm features to 0.4μm features can be great, so it becomes important to be able to look at the individual features in order to establish the depth and profiles achieved in each.

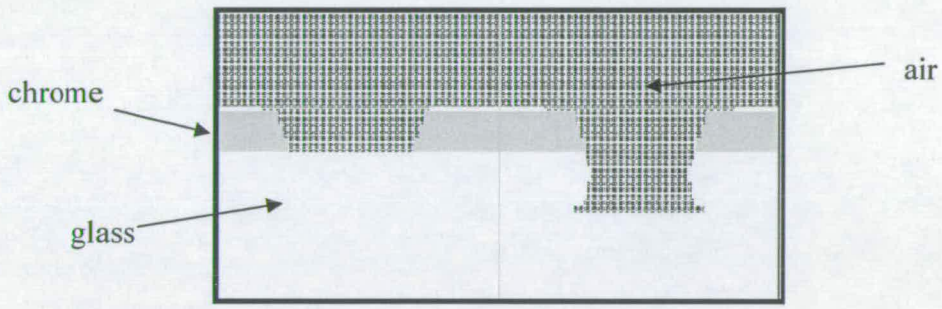

Figure 3.1. Pixelated representation of altPSM mask for EMF simulation

To build model masks a series of measurements from scan plots of the mask were taken. This data was then used to build masks that could then be fed into a 2D electro-magnetic field simulator. These model masks were built to reflect not only the depths obtained from the AFM plots but also the wall angles observed. The mask simulation files were built in a number of very small 'slices' which were then layered one on top of the other to construct a representation of the mask. This gave a pixelated staircase edge to the features, rather than the smooth rounded edge present on the actual mask. Each slice has a defined thickness and refractive index (real and imaginary parts.) The steps that represented a sloping wall were considerably greater than the increment size for each step in the simulation. An example of a mask is shown in figure 3.1. where the white area at the bottom represents the quartz, the grey area the chrome and the black cross area the vacuum. Once the masks had been built they were input to a commercially available, two-dimensional electro-magnetic

field simulator, ProMAX/2D, developed and sold by FINLE Technologies. This software uses a Finite Difference Time Domain (FDTD) technique solve Maxwell's equations for each pixel of the mask, this then produces a 'greyscale' output where the intensity and phase are calculated and data taken for a position in the near field just below the mask. This result was then taken and used in a commercially available lithography simulator, PROLITH/3D. The resultant aerial image was calculated. This was then further extended and the post-develop photoresist image calculated through simulation.

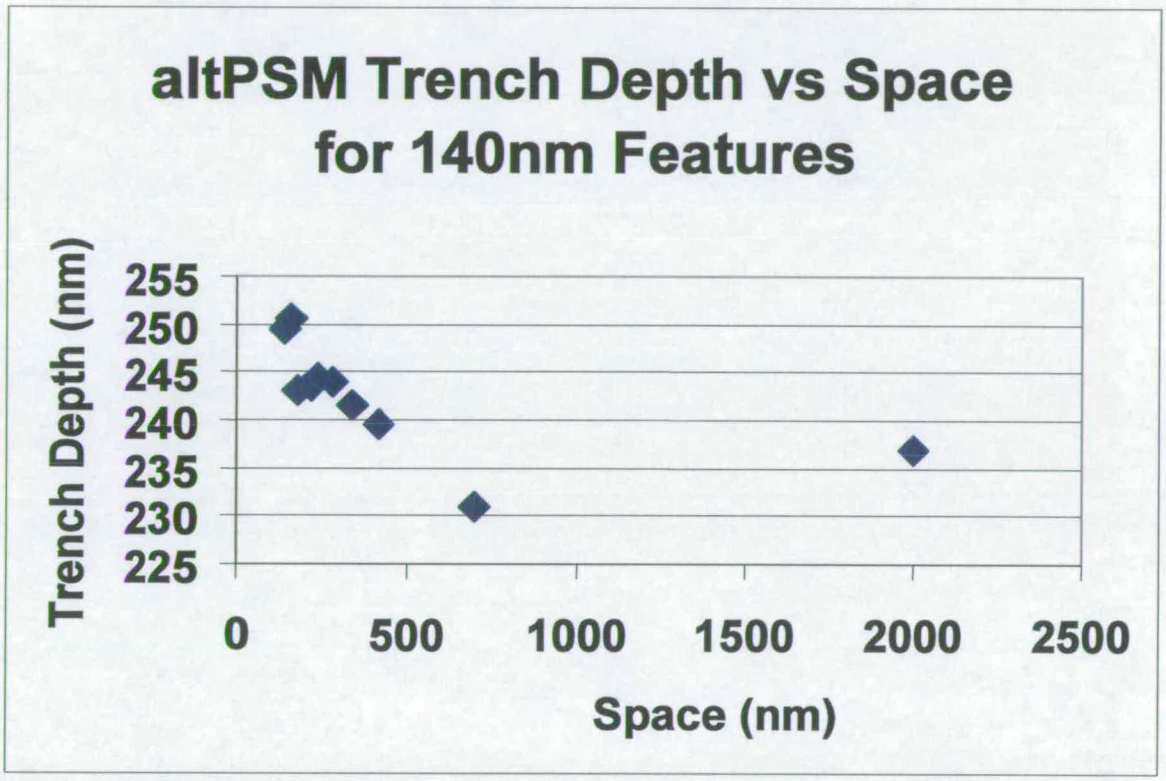

Figure 3.2. Phase trench depth vs space for 140nm nominal features.

3.3) Mask Data

The mask studied had various different structures on it, but this study concentrates on a matrix of structures based upon a nominal 1X dimension of 140nm. For this linewidth a number of different pitches were studied from 280nm out to 2140nm. A 400nm pitch where the line/space ratio was changed was also examined to represent more advanced technology. The data for the

nominal 140nm features is graphed and shown in figure 3.2. This data does not show a clear relationship between the measured trench depth and the space between the 140nm features. However, if we look at figure 3.3 this shows the same data with the most isolated pitch (2140nm, a 1:10 duty cycle) removed. A clear trend can be seen where the smaller spaces between the 140nm features have a deeper phase trench. A trend similar to this was previously observed by other researchers where it was explained by inverse reactive ion etch lag [4]. In this case the trend seems to have a fairly good linear fit. Further study of the mask at a 400nm pitch with varying line/space ratios showed no clear relationship between the space adjacent to the line and the trench depth. However the data from the 140nm features and the scatter evident here indicates that more investigation is required.

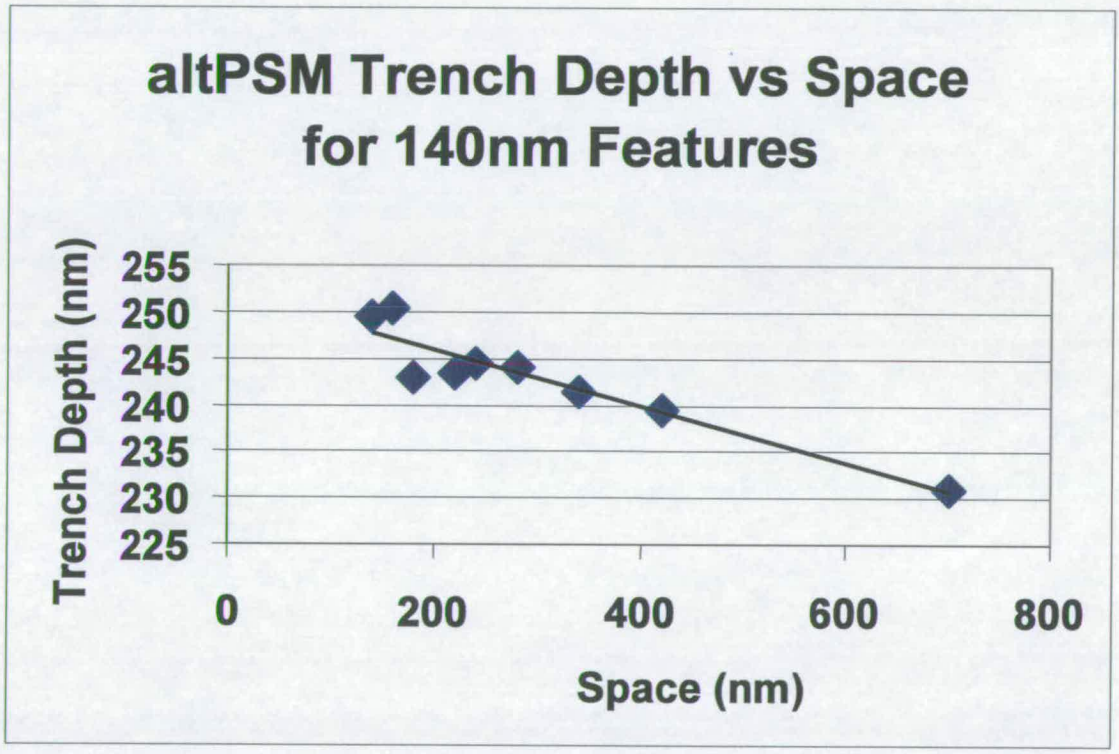

Figure 3.3. Phase trench depth vs space for 140nm nominal features for the densest duty cycles.

3.3.1) Mask Simulation

Each of the structures from the 140nm nominal features had a soft mask file built to represent the measured depths and profiles. These were then simulated with ProMAX/2D and the resultant

greyscale masks calculated. Masks were also built with the same achieved trench depth but with perpendicular chrome and quartz sidewalls as opposed to the rounded sidewalls on the real mask, to aid in de-coupling the effect of the rounding from the isotropic etch. For the purposes of this study only the E-polarised waves were considered with an incident angle of 0°. Preliminary work has also shown that the H-polarised waves have a much lesser effect upon the resultant aerial image; if a full rigorous solution is to be pursued, however, these assumptions could not be made.

The greyscale masks from the mask simulation were taken and fed into PROLITH/3D to calculate aerial images for pre-defined stepper conditions of 0.6NA lens, and 0.30σ. These calculated aerial images were then used to calculate the effective phase error against the 180° target [5]. The phase errors for the actual masks and those with perpendicular sidewalls are shown in figure 3.4. As can be seen it is not clear whether the wet etch has any effect upon the magnitude of the phase error, but for the densest pitches on this mask the errors are considerably lower than those on the equivalent model mask.

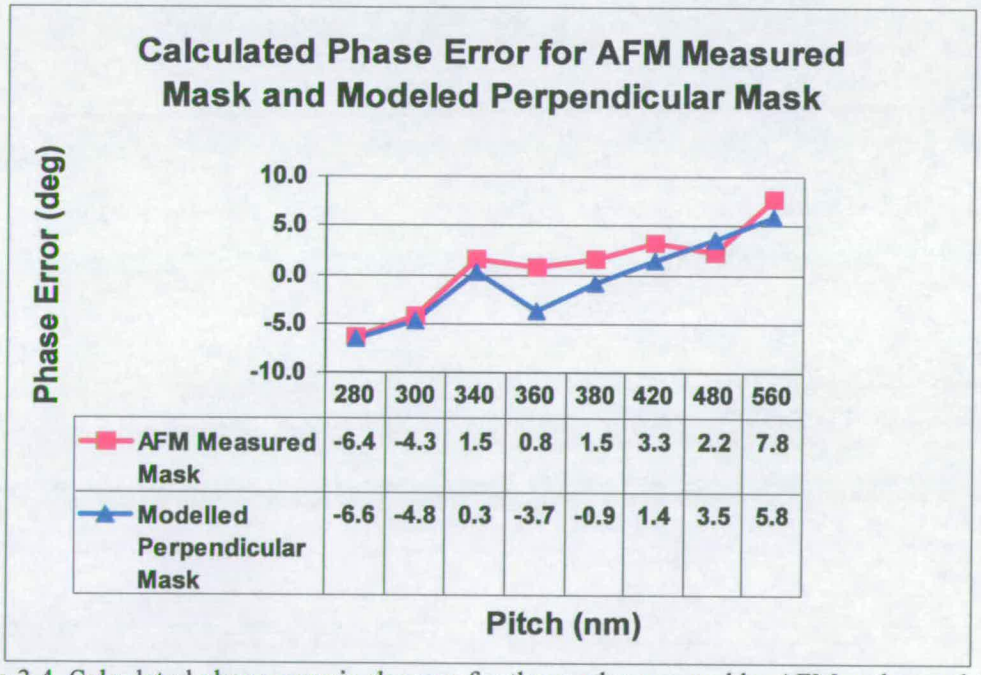

	280	300	340	360	380	420	480	560
AFM Measured Mask	-6.4	-4.3	1.5	0.8	1.5	3.3	2.2	7.8
Modelled Perpendicular Mask	-6.6	-4.8	0.3	-3.7	-0.9	1.4	3.5	5.8

Figure 3.4. Calculated phase error in degrees for the mask measured by AFM and a model mask with the same trench depth but perpendicular sidewalls.

The imbalance in intensity between the shifted and unshifted areas, expressed as a percentage of the peak intensity, was also calculated for both the mask measured by AFM and the modeled mask with perpendicular sidewalls, giving the results shown in figure 3.5. The data shows that the intensity differential follows a linear relationship against pitch for both masks. However, the intensity imbalance is considerably higher for the rounded mask that has received the isotropic wet etch.

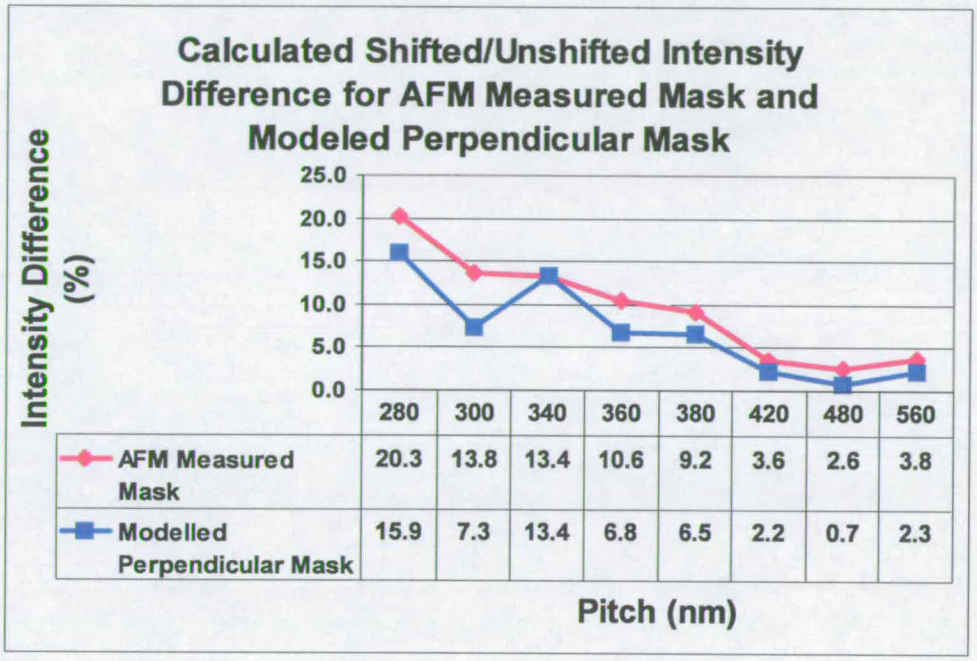

	280	300	340	360	380	420	480	560
AFM Measured Mask	20.3	13.8	13.4	10.6	9.2	3.6	2.6	3.8
Modelled Perpendicular Mask	15.9	7.3	13.4	6.8	6.5	2.2	0.7	2.3

Figure 3.5. Calculated intensity imbalance expressed as a percentage of peak intensity for the mask measured by AFM and a model mask with the same trench depth but perpendicular sidewalls.

3.4) Lithography Simulation

The photoresist image formation was also simulated from the greyscale masks and aerial image calculations previously mentioned. The process used was: 62nm of anti-reflective coating (ARC) and 400nm of DUV resist. The ARC and resist models were developed at International SEMATECH from chemical and lithographic analysis of existing processes and the methodology used to produce these models has been published previously [6]. Each mask was simulated and the process window analysed in terms of depth of focus (DOF) allowing a ±10% CD variation.

DOF is one of the most important parameters considered by the lithographer. Optical lithography systems do not have at all times perfectly flat exposure planes at the optimum focus, as such some tolerance to these defocus errors must be available. The best estimation of this comes from the DOF criterial developed by Lord Rayleigh of:

$$DOF = k_2 \frac{\lambda}{NA^2}$$

where k_2 is a process related coefficient, λ the illumination wavelength and NA the numerical aperture of the system. A summary of the results is given in table 3.1.

AFM Measured Mask

Pitch (nm)	280	300	340	360	380	420
Phase Error (deg)	0.74	-2.31	-2.33	6.10	-2.21	5.56
Intensity Imbalance (%)	30.58	31.49	25.81	24.79	17.51	14.05
DOF (μm)	1.20	1.30	1.35	1.15	1.20	1.25

Modelled Perpendicular Mask

Pitch (nm)	280	300	340	360	380	420
Phase Error (deg)	-6.61	-4.79	1.28	-3.70	-0.93	1.36
Intensity Imbalance (%)	15.90	7.26	20.13	6.81	6.49	2.21
DOF (μm)	0.80	0.95	1.25	1.25	1.60	1.65

Table 3.1. Summary of phase error, intensity imbalance and DOF for the measured and modeled masks

As can be seen from the table, the DOF is predominantly driven by the phase error, this is strongly shown in the case of the densest pitches for the measured mask where, despite an image intensity imbalance considerably stronger than the modeled mask, the DOF is larger.

The image placement was also studied at nominal best focus to study the effect of the aerial image intensity imbalance; results from this are shown in table 3.2. This data indicates that the image placement is primarily driven by the intensity imbalance.

AFM Measured Mask

Pitch (nm)	280	300	340	360	380	420
Intensity Imbalance (%)	30.58	31.49	25.81	24.79	17.51	14.05
Image Placement Error (nm)	31	31	26	25	18	14

Modeled Perpendicular Mask

Pitch (nm)	280	300	340	360	380	420
Intensity Imbalance (%)	15.90	7.26	20.13	6.81	6.49	2.21
Image Placement Error (nm)	16	7	20	7	6	2

Table 3.2. Summary of image placement error and intensity imbalance for the measured and modeled masks

3.5) Conclusions

AFM was used to extract information on the actual topography, depth and profile, observed on an alternating aperture phase-shift mask. The depth of the phase trench seemed to be related to the space adjacent to the feature being studied, an effect explained by RIE lag. This relationship between mask space and trench depth warrants more in depth investigation. EMF and conventional lithography simulation were used to calculate the effects of this mask topography upon the phase and intensity of the resultant aerial images. For the mask studied there was little effect upon the magnitude of the phase error from the rounding of the mask by the isotropic etch whilst the same technique appears to worsen intensity imbalance. When simulation of photoresist images is made the depth of focus was primarily driven by the phase error not intensity imbalance whilst the image placement error is governed by image intensity imbalance between shifted and unshifted areas. The data obtained here showing the effects of mask pattern (line/space size) upon phase trench depth indicates that the method of fabricating the mask, especially the types of etch used, requires to be quantified in order to determine if the observed difference in trench depth can be eliminated through process enhancements. If this effect cannot

be eliminated it may result in the present subtractive method of manufacturing alternating phase-shift masks becoming to complex and expensive for use in manufacturing.

References

[1] R.L. Kostelak, C. Pierrat, J.G. Garofalo, and S. Vaidya, "Exposure Characteristics of Alternate Aperture Phase-Shifting Masks Fabricated Using a Subtractive Process", J. Vac. Sci. Technol. B, Vol. 10(6), (1992), pp/3055-3061

[2] R.A. Ferguson, A.K. Wong, T.A. Brunner, L.W. Liebmann, "Pattern-Dependant Correction of Mask Topography Efects for Alternating Phase-Shifting Masks", SPIE Vol. 2440, (1995), pp. 349-360

[3] Y. Martin, H.K. Wickramasinghe, "Method for Imaging Sidewalls by Atomic Force Microscopy", Appl Physics Letters, 64 (19), (1994), pp.2498-2500

[4] P. Schiavone, F.P. Lalanne, A. Prola, "Clear Field PSM for 193nm Lithography", SPIE Vol. 3679, (1999), pp.582-589

[5] R.L. Gordon, C.A. Mack, J.S. Petersen, "Design and Analysis of Manufacturable Alternating Phase-Shifting Masks" SPIE Vol. 3546, (1998), pp.606-616

[6] J.S. Petersen, J.D. Byers, R.A. Carpio, "The Formation of Acid Diffusion Wells in Acid Catalysed Photoresists", Micro and Nano-Engineering 96, (1996), pp.169-174

Chapter 4
Wavelength Dependant Mask Defect Inspection and Printing.

4.1) Introduction

To successfully inspect a mask there are two major factors to consider: what types and dimensions of defects are critical and is the inspection tool capable of detection. Establishing the size of defect to be detected is very difficult, as these defects are at or around the limits of mask lithography and processing, making controlled production for testing very difficult. To overcome this it is possible to use simulation to predict the effects upon the desired image of the defects under study. The majority of lithography simulators use approximations to produce an aerial image from an altPSM [1]. These approximations do not take into account the losses that occur from scatter in the mask, and therefore produce aerial images with equal intensity between the shifted and unshifted spaces. To produce a more accurate simulation, which takes into account losses in the mask substrate, we must accurately establish the amplitude and phase of the light from both of these regions. To do this it is possible to utilise electro-magnetic field simulation (EMF) to establish a more accurate picture of the light that has propagated through the mask. Fortunately much work has been completed in this field and today a number of simulators have been developed that can be used to calculate this [2,3]. In this chapter one such simulator, TEMPEST, has been used to complete these calculations. However, judging whether the tool is capable remains very much an empirical process. It will be shown in this chapter that it is possible to simulate 1x inspection systems, both actinic and non-actinic, and the type of aerial image a transmission inspection on these tools may produce. For the purpose of this study only idealized square defects in the shifted space were studied, other defect cases, such as different shapes or breaks in chrome features, may give differing results.

4.2) Mask defect printing simulation

The EMF simulations used in this chapter were calculated using the TEMPEST simulator originally developed at UC Berkeley [2]. The input files for this, as well as the aerial images

from the propagated waves, were produced using the Interplay and Aerial products from Panoramic Technologies. The dimensions were obtained using some in-house programs written in MATLAB.

Firstly it is important to establish the defect free process window, so then the effect of the defect under study may be confirmed. The defect free aerial images produced were analysed and the threshold giving the desired feature dimension obtained. Once the aerial images in the defect cases were calculated, this threshold was used to give the dimension for each case.

To represent the 130nm technology node a mask with a 90nm line and 170nm space was simulated, (in all cases in this chapter the dimensions quoted are the 1x, i.e. on wafer dimensions, the only exception being the defect dimensions, which are on mask dimensions.) For this node the case chosen was a 248nm 4x exposure tool with a NA of 0.75 and partial coherence (σ) of 0.3. For the 100nm node a mask with a 70nm line and 130nm space was used, imaged in a 193nm 4x scanner with a NA of 0.78 and partial coherence of 0.3. These exposure tools are examples of the types used at these nodes. Simulations using this 193nm tool were also run using a 70nm line with 350nm space, and 50nm line with 350nm space. The defects studied were idealised square defects placed in the shifted space. For the 90nm line/170nm space and 70nm line/130nm space cases the defect was placed either in the centre or edge of the shifted space. For the 70nm line/350nm space and 50nm line/350nm space the defect size was fixed and its position within the shifted space varied.

4.2.1) Defect size

Figure 4.1 shows the defect free process window for the 130nm case to be 0.3μm and 0.25μm for the 100nm case (in the figure only one side of focus is shown). The critical dimension (CD) of the 130nm node and 100nm node with defect cases is shown in figure 4.2. For each node the CD has been calculated at best focus and at the defocus value at the edge of the defect free process window. It is interesting to note that the actual printing of the defect does not set the process window, it is the disturbance of the aerial image and the change in CD (a CD tolerance of ±10% has been allowed,) that defines the critical defect size. In the 130nm node case centre defects are tolerable up to 140nm. For edge defects it was greater than this; in both cases the defects are more critical at best focus than at defocus. At the 100nm node the centre defects of 100nm and greater result in more than 10% CD variation as do edge defects of 150nm or greater.

Again best focus is more sensitive than defocus. For both node cases, the defocused aerial image is more tolerant of the defects, this is likely due to the fact that in these features the CD is smaller when defocused, so when the aerial image is broadened by the defect it has more margin until it exceeds' the maximum allowable CD.

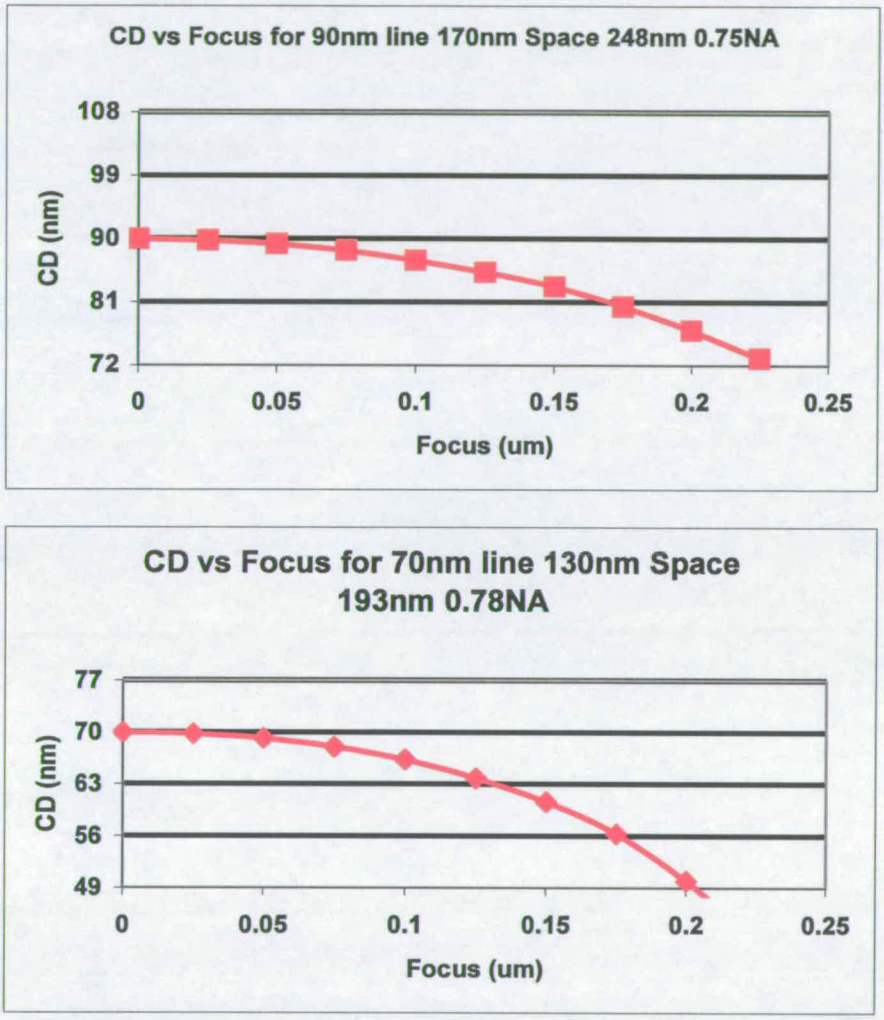

Figure 4.1. CD vs. defocus for the 130nm node case (top) and 100nm node case (bottom). Both are for the defect free cases.

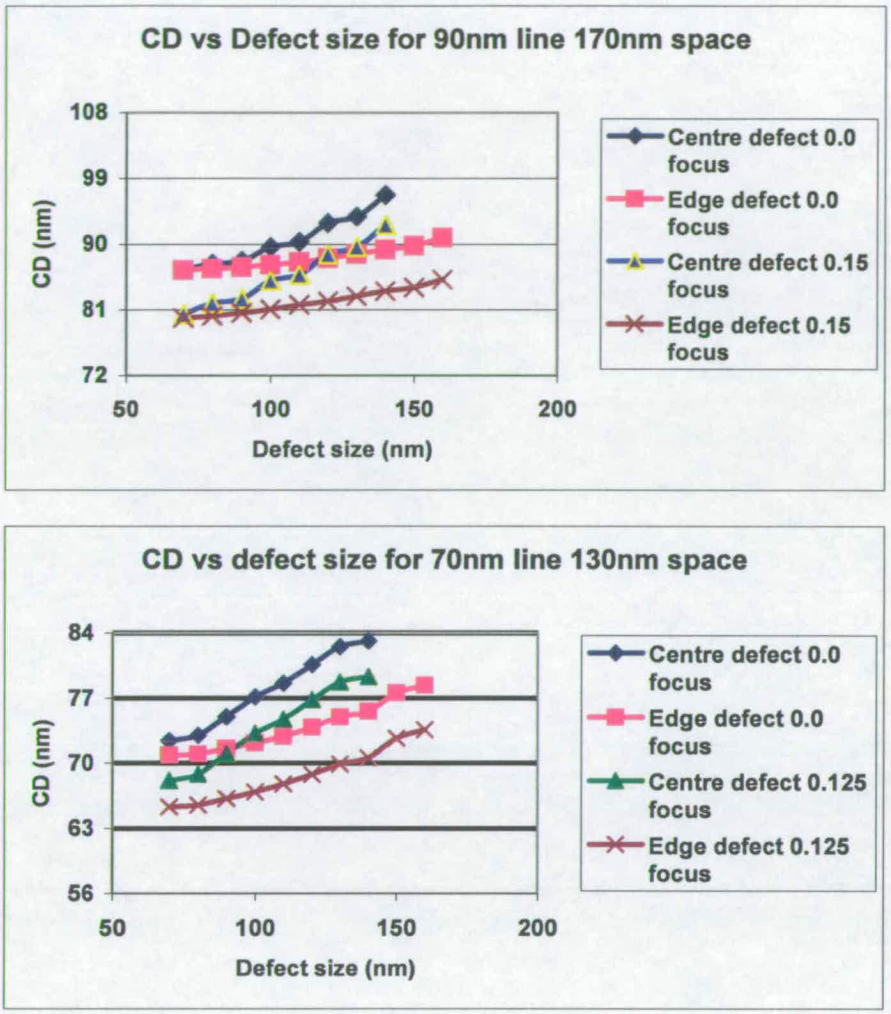

Figure 4.2. CD vs defect size for the 130nm node case (top) and 100nm node case (bottom). Defects in the centre and at the edge of the shifted space are shown at best focus and at defocus values equating to the edge of the defect free process window.

4.2.2) Defect position

To study the effect of the defect position a number of simulations were run where the defect dimension was held constant but its position within the shifted space varied. This work was completed for one of the semi-dense cases already used and more isolated cases. Three features were used: 70nm line with 130nm space (the defect being 130nm), 70nm line with a 350nm space (the defect being 130nm,) and 50nm line with a 350nm space (the defect being 100nm.)

For all, the imaging system was the 4x 193nm scanner, 0.78NA and 0.3σ. Figure 4.3 shows the CD vs position of the defect edge from the edge of the shifted space. The semi-dense cases studied earlier showed that a defect in the centre of the shifted space had much more effect than one at the edge. The top plot in figure 4.3 shows that the effect of the defect in the semi-dense case (70nm line/130nm space) is again much greater in the centre, but the maximum effect is when the defect is mid-way between the edge and centre. In the 70nm line/350nm space, the defect has the largest effect upon the feature dimension when it is ~35nm from the edge of the chrome feature as can be seen in the middle plot of figure 4.3. By the time the defect is ~105nm away in the best focus case the CD variation is less than 10%. For the defocus case the defect must be more than 175nm away before the CD variation is below 10%. When the linewidth is reduced to 50nm the 100nm defect causes the largest CD variation when ~70nm from the edge, this can be seen in the right plot in figure 3. At best focus this defect must be more than 140nm from the edge for a variation below 10%, however when defocused this increases to greater than 175nm.

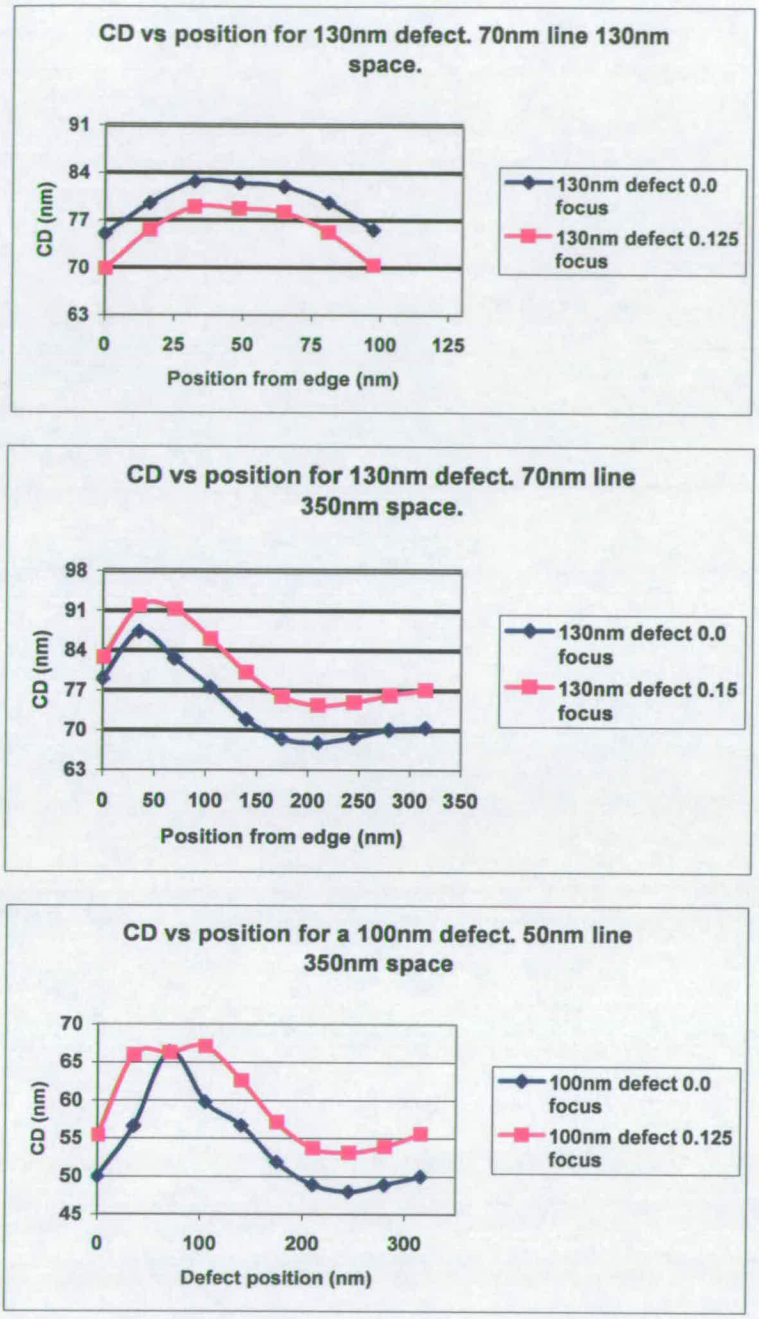

Figure 4.3. CD vs position from edge of the shifted space for a 130nm defect with 70nm line/130nm space (top), 130nm defect with 70nm line/350nm space (centre) and a 100nm defect with a 50nm line/350nm space (bottom). The imaging tool simulated was 4x 193nm, 0.78NA, 0.3σ.

Examination of the CD variation versus defocus for the defect free isolated structure situations, with these linewidths, is shown in figure 4.4. These plots indicate that as the defocus increases so does the CD, this is the opposite of the previously studies cases shown in figure 4.1. In the case of more isolated features such as this, the defects actually have more effect upon the CD as they broaden further an already widening aerial image.

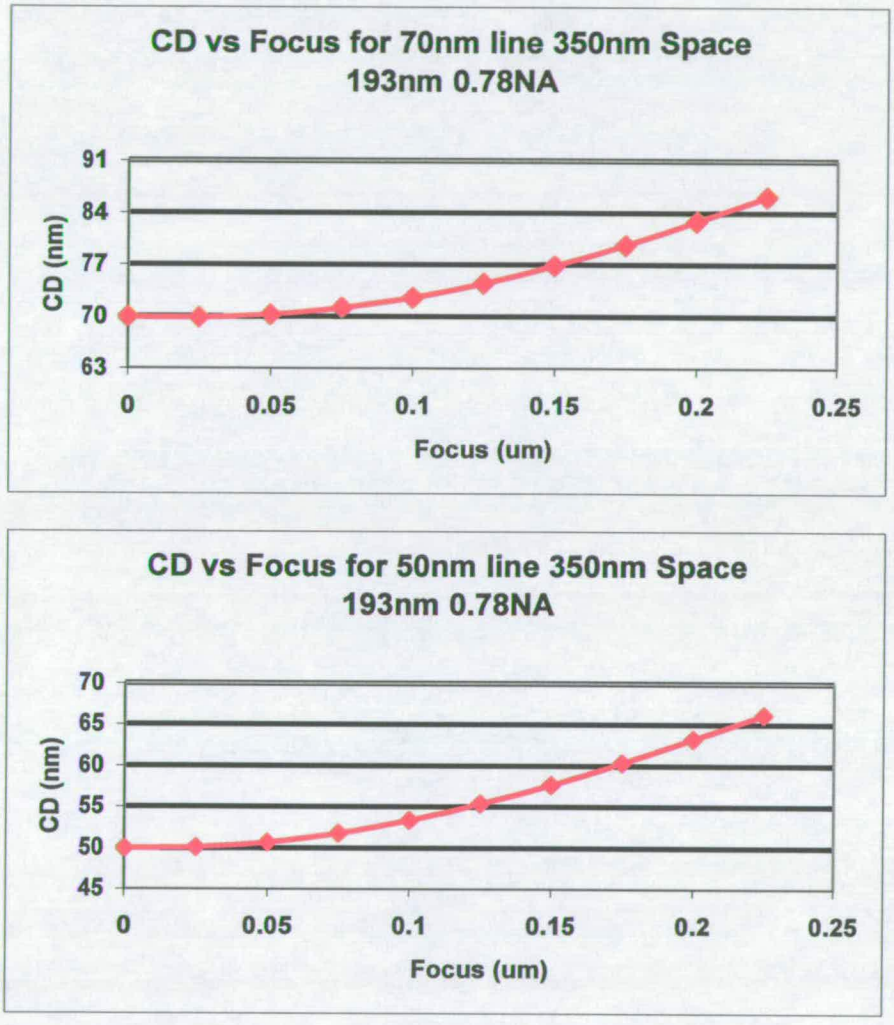

Figure 4.4. CD vs. defocus for the 70nm line/350nm space case (top) and 50nm line/350nm space case (bottom) imaged with 4x 193nm, 0.78NA, 0.3σ. Both are for the defect free cases.

4.3) Defect inspection

4.3.1) Defect inspection methodology

Many of the mask inspection systems used today are optically very different from the exposure tools the masks are used in. While they may use transmission, as is used for exposure, they may also add to this a reflected inspection. Another major difference is they tend to be 1x imaging tools, whereas the exposure tools are in the main 4x reduction systems. Simulation of a 1x imaging system compared to a 4x system is complicated by the many more diffraction orders gathered in the 1x system. To compensate for this it is no longer possible to simply take zero angle incident waves but non-perpendicular incident waves must be included [4]. The relative source positions of these should be calculated to take into consideration not only the wavelength being used but also the lens NA and the domain being studied.

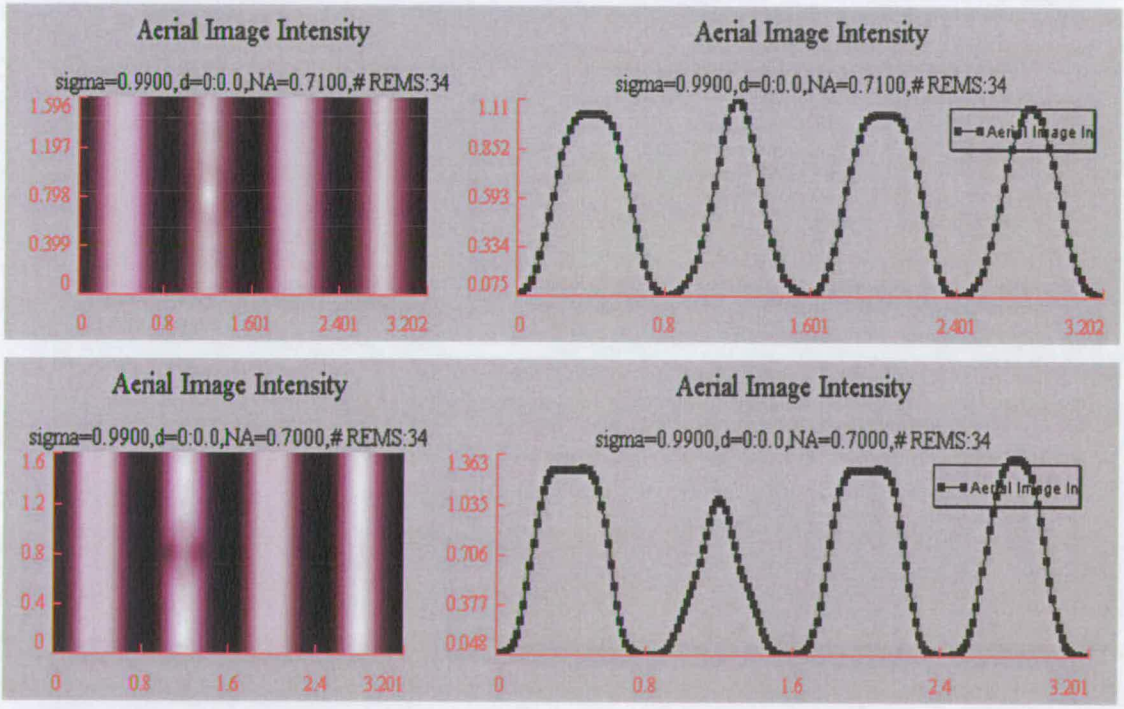

Figure 4.5. Aerial image from 1x imaging systems with 0.7NA for a 257nm source (top) and 193nm source (bottom) on a mask with 70nm line/130nm space and a 100nm defect in the middle of the shifted space

.

4.3.2) Results of size, position and wavelength dependence

Actual inspections of photomasks is further complicated by the use of non-actinic wavelengths. Some of the latest tools use solid-state sources emitting at 257nm [5]. Considering a transmissive imaging system, the aerial image produced by this has been calculated. assuming an NA of 0.7, partial coherence of 0.99 and the relevant incident orders of light (from the planes of incidence being restricted by periodicity). The aerial images for a 257nm system and 193nm illuminated system, for the 70nm line/130nm space, with 100nm centre defect are shown in figure 4.5. The figure shows a view of the aerial image intensity to the left and a cross section through the defect on the right. As can be seen the aerial image is not greatly disturbed by the defect in the 257nm system (top) but is much more greatly disturbed in the 193nm illuminated system.

Simulations were also made for the 70nmline/130nm space case with a 150nm defect at the edge of the shifted space. The optical systems were assumed to be the same and the aerial images are shown in figure 4.6. For the 257nm system the edge defect causes a much greater disturbance in the aerial image than for the centre defect, though again the 193nm illuminated system is more greatly effected.

To further explore the capability of the transmissive inspection systems simulations were run for both illumination wavelengths using higher NA lens settings. Figure 4.7 shows the aerial images for 70nm line/130nm space with 100nm centre defect for tools with 257nm source (top) and 193nm source (bottom). The left-hand plot shows a NA of 0.8 and the right hand a NA of 0.9 in each wavelength. It can be seen for the 257nm tool that increasing the NA to 0.9 does make the aerial image at the defect more prominent, however when compared to the 193nm source the difference is still significantly less.

One possible way to enhance the capability of the 257nm illuminated inspection system is to modify its imaging conditions. Figure 4.8 shows a 257nm 0.7NA inspection of the 70nm line/130nm space pattern with a 100nm defect in the centre of the shifted space. The left plot shows the effect of varying focus for a coherence of 0.99σ. The right variation of coherence for a focus of 0.0μm. It can be seen that changing focus to a setting of +0.4μm increases the differential in the aerial image intensity for the position with defect, as does decreasing

coherence to 0.3σ. The change in coherence seems to be the stronger of these two factors. A combination of these is shown in figure 4.9 where focus is varied for a coherence of 0.3σ. Once again a defocus of +0.4μm gives the largest differential in aerial image intensity.

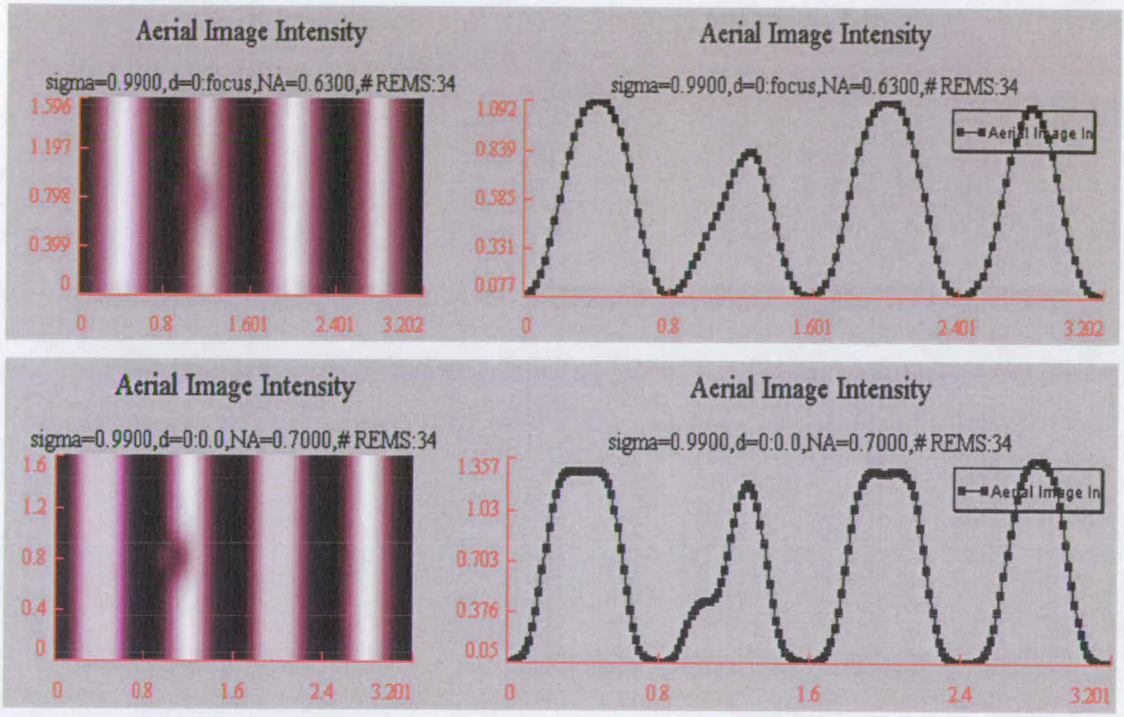

Figure 4.6. Aerial image from 1x imaging systems with 0.7NA for a 257nm source (top) and 193nm source (bottom) on a mask with 70nm line/130nm space and a 150nm defect at the edge of the shifted space.

4.4) Conclusions

The dimensions of the defects calculated in this work can be compared to the ITRS roadmap, a summary of which is shown in table 4.1. The roadmap calls for a defect limit of 100nm at the 130nm technology node, the work here indicated that defects up to 140nm were tolerable for the case studied here. At the 100nm technology node the ITRS value is 80nm, this compares to 100nm derived here. It should be noted that the cases studied here in no way cover all of the potentials for these nodes so it is possible that more sensitive cases exist. The aerial image has

not been coupled into the resist in these studies, this may also heighten the effects. Simulation studies show that smaller defects at the centre of a shifted space rather than at the edge result in the limits of CD tolerance being reached. In semi-dense patterns the defects have greater effect at best focus than at the edge of the focus window, whereas in more isolated cases the defects have greater effect at defocus. The most sensitive position for a defect is not at the edge or centre of the shifted space but rather at a position between these two.

The 1x inspection simulations indicate that actinic inspection is significantly more sensitive than non-actinic inspection. This is especially evident in the case of defects in the centre of the shifted space where the difference in aerial image intensity between with defect and defect free positions is difficult to detect. For defects at the edge of a shifted space the non-actinic inspection appears to be more likely to detect these features than for a centre defect. The sensitivity of non-actinic inspection can be improved by increasing the NA of the inspection system, changing the coherence and using defocus.

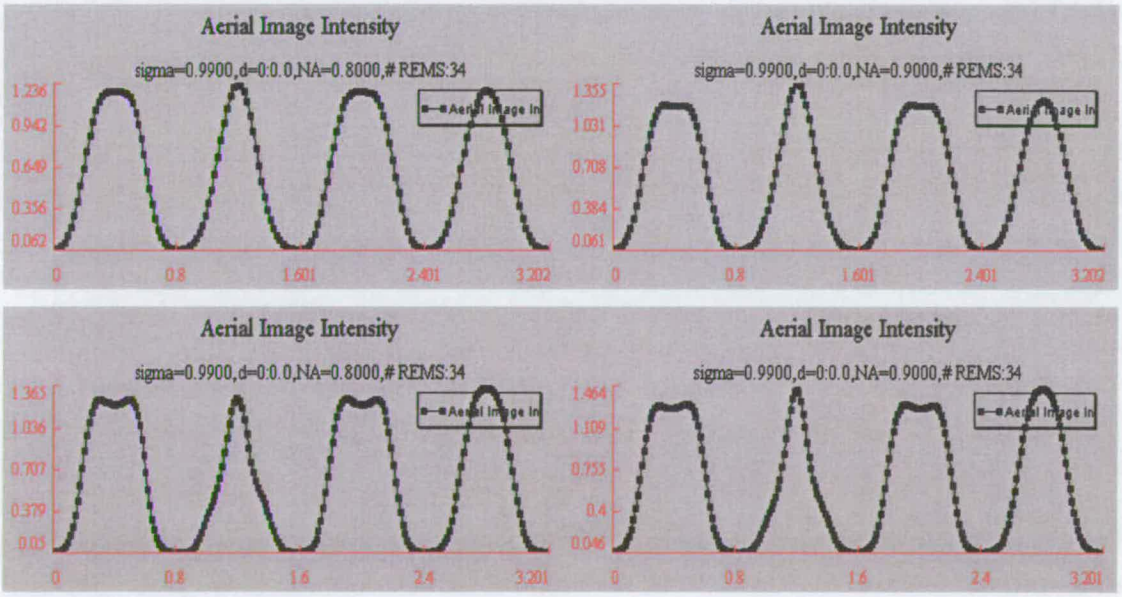

Figure 4.7. Aerial image from 1x imaging systems with a 257nm source (top) and 193nm source (bottom) on a mask with 70nm line/130nm space and a 150nm defect at the edge of the shifted space. For each wavelength the left-hand plot shows a NA of 0.8 and the right hand a NA of 0.9.

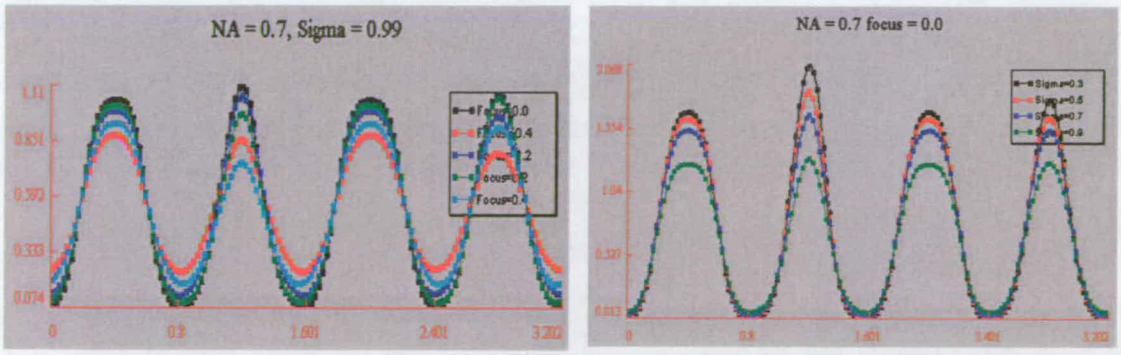

Figure 4.8. Aerial image from 1x imaging systems with a 257nm source on a mask with 70nm line/130nm space and a 100nm defect in the centre of the shifted space. The left plot shows focus varied for a 0.99σ coherence, the right coherence varied for a focus of 0.0μm.

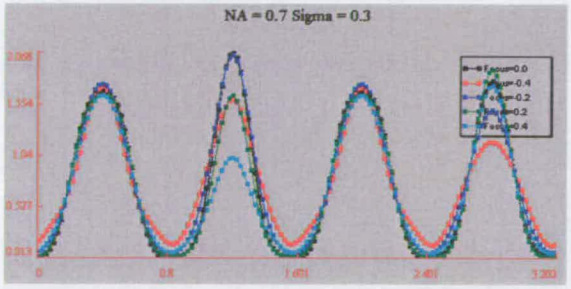

Figure 4.9. Aerial image from 1x imaging systems with a 257nm source on a mask with 70nm line/130nm space and a 100nm defect in the centre of the shifted space. The plot shows focus varied for a 0.3σ coherence.

Year	*2001*	*2002*	*2003*	*2004*	*2007*	*2010*	*2013*
TECHNOLOGY NODE	*130nm*			*90nm*	*65nm*	*45nm*	*33nm*
Mask minimum image size	*360*	*320*	*280*	*240*	*180*	*128*	*92*
Defect size	*104*	*92*	*80*	*72*	*52*	*36*	*26*

Table 4.1. Summary of allowable mask defect size from the ITRS roadmap, 2000 update.

References

1. M.D. Levenson, N.S. Visanathan, R.A. Simpson, "Improving resolution in photolithography with a phase-shifting mask", IEEE Transactions on Electron Devices, Vol ED-29, No. 12, pp.1828-1836, 1982.
2. A. Wong, "Rigorous three-dimensional time-domain finite-difference electromagnetic simulation", Ph.D. dissertation, University of California at Berkeley, 1994.
3. C.K. Kalus, S. List, A. Erdmann, R.L. Gordon, M. McCallum, A. Semmler, "Benchmarking of available rigorous electromagnetic field (EMF) simulators for phase-shift masks applications", Microelectronic Engineering, pp.79-86, 2001.
4. T.V. Pistor, A.R. Neureuther, R.J. Socha, "Modeling oblique incidence effects in photomasks", SPIE 4000, pp.228-237, 2000.
5. D. Alles, P. Ter Beek, S.T. Juang, J.N. Wiley, K. Hsai, "Mask inspection system using DUV wavelength and new alogorithm platform for advanced mask inspection for 0.13-um technology node", SPIE 4066, pp.462-471, 2000.

Chapter 5
Electrical Characterisation of Binary and Alternating Aperture Phase-Shifting Masks

5.1) Introduction

Advanced masks are routinely being used today to produce very small features that drive our requirements for ever faster and lower power chips. These masks obviously also require very small features to be clearly patterned and are consequently difficult and expensive to manufacture. Hence, an accurate and robust capability to test and characterise the mask making process is very important. However, as device manufacturers know, small dimensions are not easy to accurately measure using conventional optical measurement tools. As a result tools such as SEMs are employed to achieve the resolution and accuracy required. These tools are prohibitively expensive and also come with technical problems. One of the major issues with mask metrology is the industry wishes to measure conductive features (chrome) on an insulating base (glass). This situation is bearable on silicon where the substrate is semi-conductive but exceedingly difficult to deal with on photomasks. This chapter examines the issues involved in the use of relatively low cost Electrical Critical Dimension (ECD) measurement of mask features. This technique has the twin advantages that it requires relatively low cost equipment and actually requires a patterned conductor on an insulator. Further, it will look at the application of electrical measurement into alignment measurement. To date mask makers have only had to roughly centre the circuit pattern on the glass as it was a single writing layer. Phase-shifting masks generally require a second layer to be written aligned to the first, normally at tolerances under 100nm. In this work a new test structure has been developed to measure the alignment between the chrome blocking features and the phase shifting regions etched into the quartz substrate (for the phase shift etch the chrome acts as a self-aligned mask for the open glass areas, hence the term chrome blocker). Results are presented, obtained from state-of-the-art masks fabricated in a commercial mask shop, which demonstrate the capability effectiveness of the test structure when used in a progressional offset array.

5.2) Electrical linewidth dimension test structures

To electrically test dimensions a crossbridge linewidth structure [1] on a 4× mask was chosen for use on a Nikon step and scan DUV system. The crossbridge structure consists of two different sections. The first is a Greek cross [2] which is a type of van der Pauw, sheet resistance (R_S) measurement structure [3,4]. The second part is a bridge structure which is used, in conjunction with the value of sheet resistance obtained from the Greek cross, to extract the electrical linewidth [5].

Cross-bridge test structures, which have been used to investigate metal damascene interconnect processes [6], were used as the basis for the on mask patterns. These could be used directly for the binary patterns but some adaptation was required for the altPSM patterns. In the "dense" test structures the electrically measured line is surrounded by floating lines and phase shifting regions and is illustrated in Figure 5.1 [7].

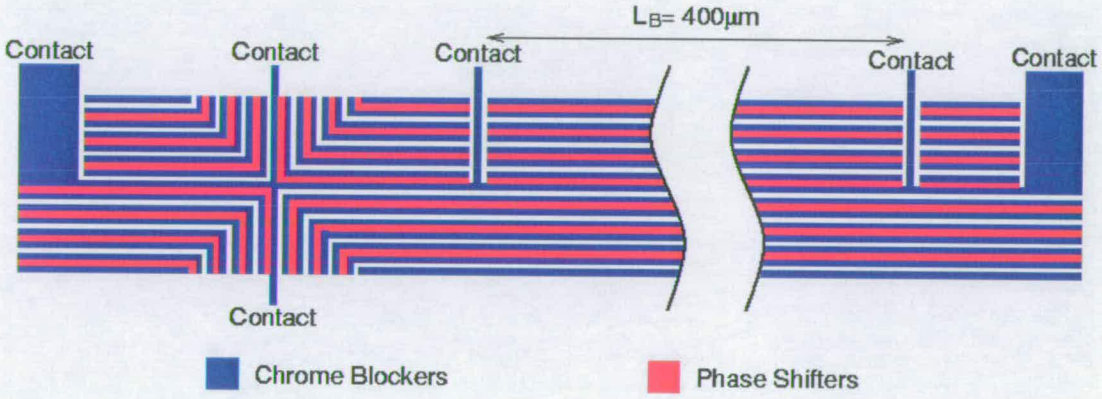

Fig. 5.1. Section of PSM test structure layout. The black areas are the chrome features while the shaded areas are regions of 180° phase shift. This is a structure with a linewidth of 15µm and a line to space ratio of 1:1.

5.3) Application of test structures to a mask

The test structure layout contains test structures with on mask linewidths of 0.4, 0.5, 0.6, 0.7, 0.8, 0.9, 1.0, 1.1, 1.2 and 1.5µm. Bridge structures with line to space ratios of 1:1, 1:1.5, 1:2, 1:3, 1:5 and 1:10 were designed for each of the feature sizes. There are two sets of dense structures with different arrangements of the dummy lines around the Greek cross. In the first set the floating lines follow the shape of the cross, and these will be referred to as "L-Type" structures.

In the second set the unmeasured lines run up to the vertical contact arms of the cross and stop short as they do in the bridge section of the structure. This set will be referred to as "I-Type" test structures. Both of these types are shown in figure 5.2.

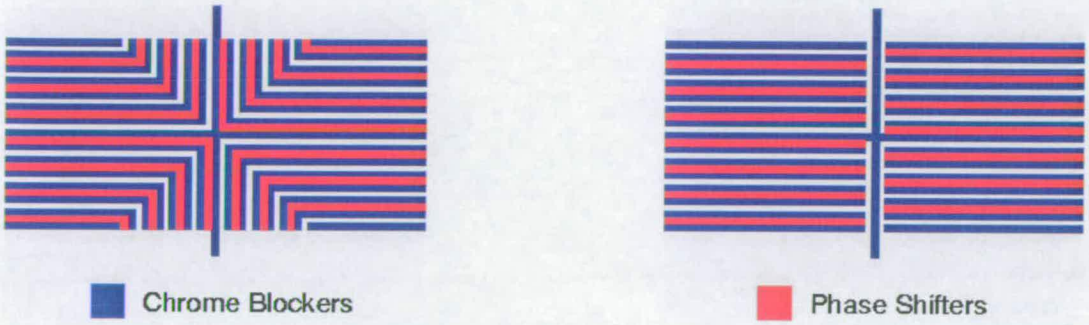

Fig. 5.2. Layout of the L-type (left) and I-type (right) Greek cross structures.

The module layout was a 14 x 10 array of test structures with probe pads which could be probed using a standard 2 x n probe card. This included two isolated linewidth structures for each feature size. Two modules were produced: one with pads sized for on-mask probing and one where the probe pads are scaled so that when the structures are printed using a 4x exposure tool the pads will be the same size as those designed for on-mask measurement. The layout with the large pads was repeated three times on the mask, once with the phase shifting elements removed to give binary structures. The version with the small pads for on-mask testing was repeated twenty four times, in three blocks of eight, where one set contains binary structures. A picture of the mask can be seen in figure 5.3 along with a close-up of the layout for on-mask probing.

The chrome layer on the mask was written on a variable shaped e-beam tool [8]. The phase-shifting layer on a laser based optical tool. Phase etch was performed using an ICP etch tool. The phase-shifting layer was designed with an overlap of 200nm over the chrome features.

The SEM used to measure the mask was a modified Hitachi S-7080. The wafers were measured on a Hitachi S-8840 SEM. Electrical measurements from both automated and manual probe stations were measured using an HP-4145B, HP 4062B and Solatron microvoltmeter.

The wafer exposures were performed using a Nikon S-204B step and scan tool with an NA of 0.68 and partial coherence of 0.4. The wafers were coated in 400nnm of Shipley UV210 resist and developed in 0.26N developer on a DNS 200B track interfaced to the exposure tool.

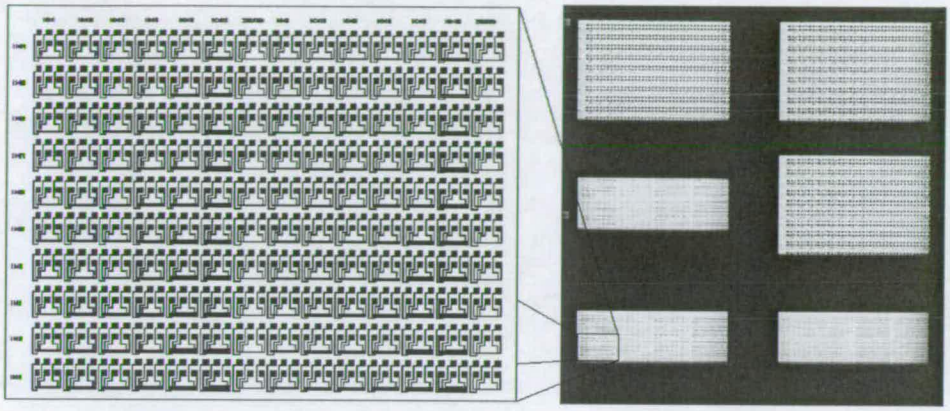

Fig. 5.3. Photograph of the actual phase shifting mask with a close up view of the layout of one of the sets of on-mask test structures.

5.4) Linewidth measurements

5.4.1) Electrical linewidth measurements

The Anti-Reflective (AR) coating of chromium oxide on the mask presented a challenge when electrically probing the devices [9]. Initial attempts to use a standard 2 × 4 probe card designed to probe aluminium pads were unable to make reliable electrical contact because the AR coating was too hard for the probe tips to penetrate. However, it was found that steerable probes on a manual probe station were able to pierce the AR coating and contact the underlying chromium. It should be noted that considerable force was required to make contact but no scratching of the pads was observed. Sheet resistance measurements were made on the Greek cross section of one of the isolated binary 1.5μm structures. The measurements were very noisy partly because the potentials were being measured using Source Monitor Units (SMUs) which did not have a high enough resolution for low voltages. The repeatability was significantly improved by using higher currents as can be seen in Fig. 5.4.

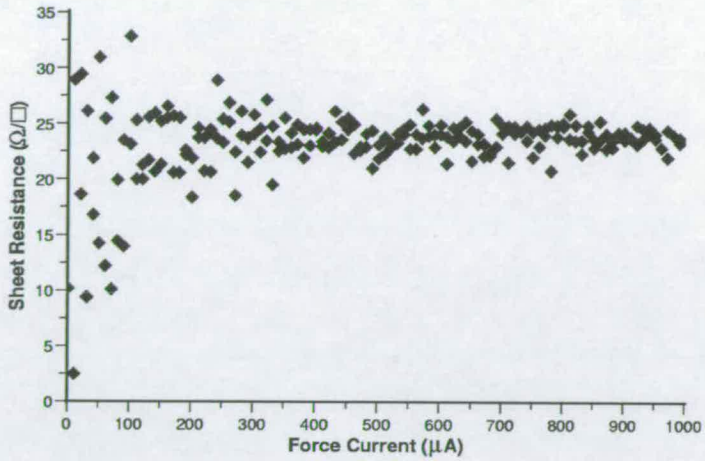

Fig. 5.4. Results of Kelvin measurements made on a chrome Greek cross structure as the force current was swept from 1μA to 1mA.

One interesting result was that although the repeatability at low currents was quite poor, a large number of measurements at a set force current typically resulted in almost the same mean value. Sets of 200 measurements were made over a short space of time at five force currents ranging from 10μA to 1mA. The mean values and standard deviations of sheet resistance calculated for each current setting are plotted in figure 5.5.

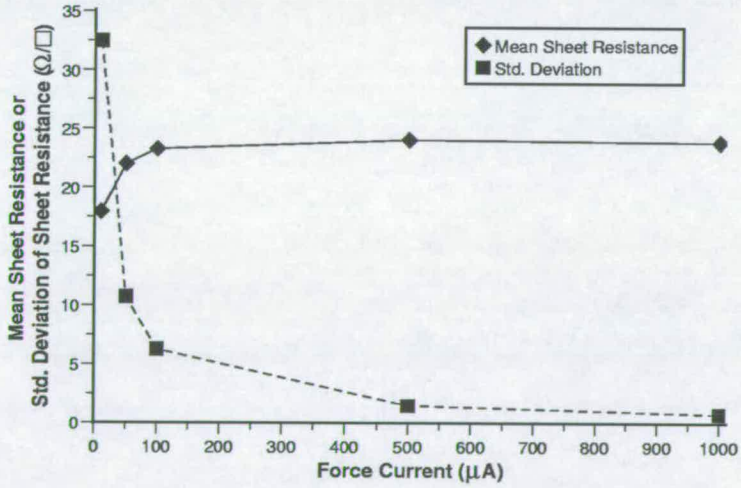

Fig. 5.5. Mean and standard deviation of sheet resistance versus force current for a chrome Greek cross structure.

The results indicate that although the repeatability of the measurement improves with higher force currents these high currents do not appear to lead to joule heating and a change in resistance. As the repeatability of the measurement is almost the same at 500μA and 1mA it was decided that the lower current should be used in any further measurements as a precaution against damaging the structure under test. The measured sheet resistance of 24.13Ω/□ is similar to a reported value of 19.4Ω/□ for chrome without an AR coating [9].

The chromium oxide AR coating was then removed by a very short etch in an aqueous solution of ceric ammonium nitrate and acetic acid. This meant that a test system using a probe card and semi-automatic probe station could then be used. This system used a voltmeter with a higher resolution which provided more repeatable and precise measurements.

Next, one complete set of structures (see figure 5.3) from the binary section and one from the phase shifted region were measured using the higher resolution system and the semi-automatic probe station. The sheet resistance results obtained from the dense I and L-type test structures have been averaged together for each feature size and are presented in figure 5.6.

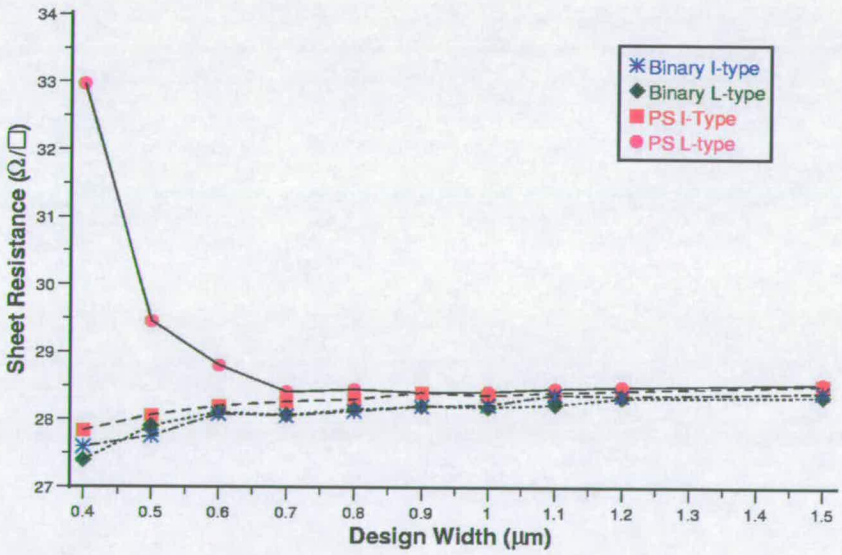

Fig. 5.6. Mean values of R_S against feature size for dense chrome Greek cross structures.

Ideally sheet resistance (R_s) should be insensitive to feature size and the variation for structures with a nominal width of more than 0.7μm is small. For example, the difference between the mean sheet resistance extracted from the phase shifted I-type structures with a cross arm width of 0.7μm and those that are 1.5μm wide is ~0.25Ω/□ which is less than 1%. The narrower structures show much more variation with size, in particular the sheet resistances extracted from the phase shifted L-type structures show a sharp increase as dimensions reduce. At present the reason for this is not clear but it is only in the L-type structures that the phase shifting elements surround the centre of the Greek cross as can be seen in figure 5.1. The fabrication of the phase shifters may be affecting the geometry of the cross leading to problems with the measurements. Figure 5.7 shows the average asymmetry factor F_A plotted against feature size. F_A is a figure representing the difference between measurements made on a cross structure at different orientations and is used to calculate a correction factor which is applied to the calculated sheet resistance to correct for asymmetry [10].

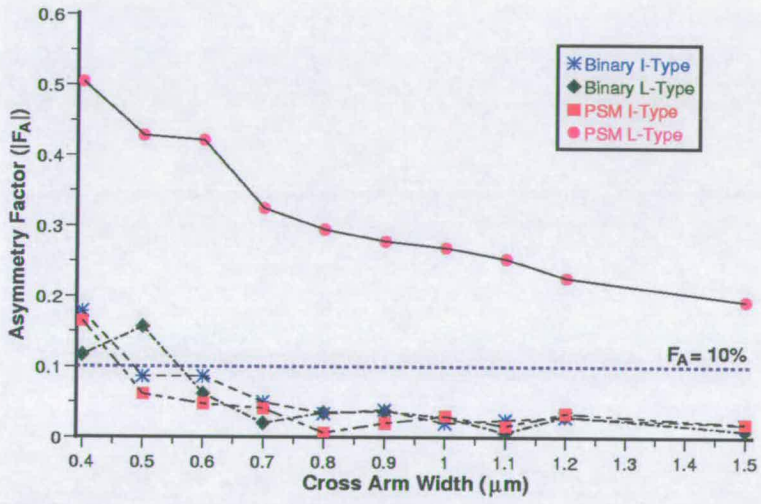

Fig. 5.7. Average Greek cross asymmetry factor $|F_A|$ versus feature size for chrome structures.

Provided that F_A <0.1% the correction factor approaches unity and does not need to be used. Figure 5.7 shows that F_A is negligible for binary and I-type phase shifted cross structures with cross arms wider than 0.7μm. Even the narrowest of these structures only requires correction of about 0.3% to the value of R_S. The results from the L-Type phase shifted structures confirm that these structures are not symmetrical and that correction factors should be applied. The sheet

resistance results for these structures that are plotted in figure 5.8 have been corrected according to the method described in reference [11] and this has been effective for the structures wider than 0.7μm. However, asymmetry correction cannot account for the high values of sheet resistance encountered in the narrower crosses. The effect of the phase shifting elements on these structures may have led to current crowding and joule heating in the narrow tracks during measurement. Alternatively these structures may no longer have the correct geometry to be considered as van der Pauw structures and in this case the results should be disregarded.

In addition to the extraction of mean sheet resistance for all the structures with the same nominal feature size, as shown in figure 5.6, it is possible to investigate the variability of the measurements across the a of different dimensions by taking the standard deviation. The results of these calculations are presented in figure 5.8.

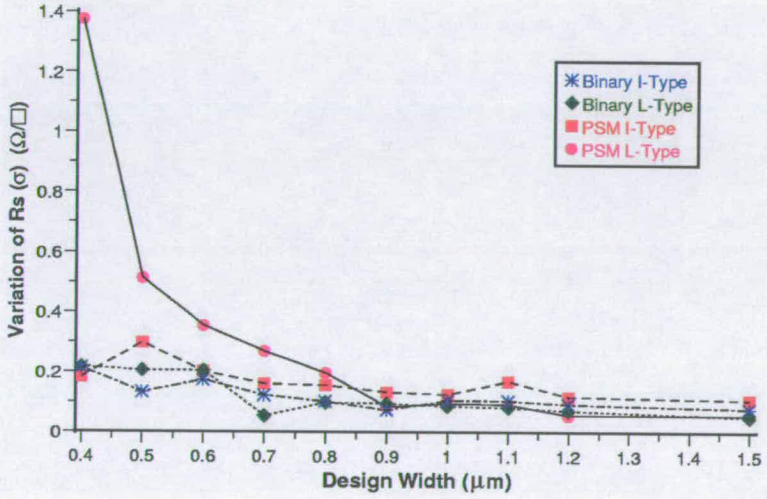

Fig. 5.8. Standard deviation of Rs against feature size for dense chrome Greek cross structures.

It would be expected that the variation of the sheet resistance between different structures of the same size would reduce as the cross arm width is increased. Reference [12] shows that larger Greek cross structures are less sensitive to short range non-uniformity in the resistivity of the conducting film being measured. Large structures effectively extract the average sheet resistance for the material.

Initial measurements of the resistance of a nominal 1.5μm wide track were performed using the manual probing system before the chromium oxide was removed and the results are presented in table 5.1.

Force Direction	Mean Resistance (Ω)	σ_R (Ω)
Forward	6730.22	2.4537
Reverse	6729.34	2.2709
Average	6729.78	-

Table 5.1. Results of Kelvin measurements made on a bridge linewidth structure with a force current of 500μA.

The standard deviations observed when making the bridge measurements are proportionally much smaller (~0.035%) than for the Rs measurements where σ was almost 20% in some cases. This is probably because the voltages being measured are much higher for the bridge structures than for the crosses. The electrical linewidth W_L is calculated by taking the average bridge resistance R_B from table 5.1 and using it in:

$$W_L = \frac{R_s L_B}{R_B}$$

where L_B is the length of the bridge section and R_S is the average sheet resistance. The result of this calculation is that W_L = 1.434μm and the nominal value of linewidth was 1.5μm so the electrical width is about 4.4% less than this. If the individual values of R_S from each orientation are used to calculate linewidth figures using the average bridge resistance it can be seen that the measurements which showed the best repeatability provide values of ECD closest to the nominal linewidth. The linewidth results and the standard deviations of the sheet resistances can be seen in table 5.2.

There are two main sources for variability in ECD measurements, firstly the measurement of the resistance of the bridge itself and secondly the value of sheet resistance used in the linewidth

calculation. The first can be minimised through the choice of measurement current and, as is clear from the results in table 5.1, makes up a very small proportion of the measured resistance. The sheet resistance variability is more of a problem. It was shown previously that the value of R_S extracted from the cross structures was a function of the feature size and it was also found that the repeatability of the measurements improved as the nominal cross arm width was increased. For this reason it was decided that the average of the sheet resistances extracted from the 1.5μm structures should be used in the calculation of ECD. These values are 28.5Ω/□ for the phase shifted structures and 28.4Ω/□ for the binary structures.

Orientation	Mean R_S (Ω/□)	σR_S (Ω/□)	W_L(μm)
+0°	24.0328	4.886	1.428
-0°	24.3091	0.462	1.445
+90°	23.7083	4.809	1.409
-90°	24.4804	0.489	1.455

Table 5.2. Sheet resistance, standard deviation of R_S and linewidths for each Greek cross measurement orientation.

5.4.2) Electron microscope linewidth measurements

To assess the capability of the electrical measurements against a more standard methodology, the mask was measured on a CD SEM using their modified threshold method [13]. It was noticed during this measurement that care must be taken to ensure that structures being measured, especially during repeated measurement, do not build up a charge. With an isolated feature on an insulator such as this charge up is rapid and undoubtedly influences accuracy. The altPSM mask showed considerably more charging than the binary mask, probably due to the exposed chrome where the CrO_2 ARC was removed by the phase well etch.

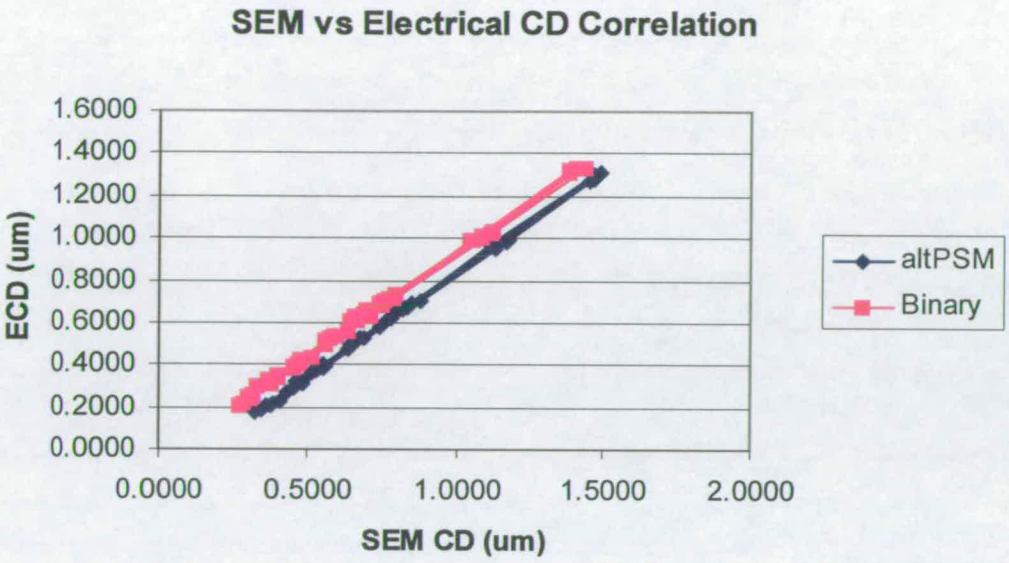

Fig. 5.9. Comparison of SEM CD (left) and ECD (right) for the binary and altPSM patterns.

The correlation of electrical to SEM measured linewidths is show in figure 5.9. The correlation for both binary and altPSM features can be seen to be very good. Analysis of this correlation gave an R^2 fit of 0.999 for both binary and altPSM, the covariance of these were 0.112 and 0.118 respectively, indicating that the spread of the fit was small.

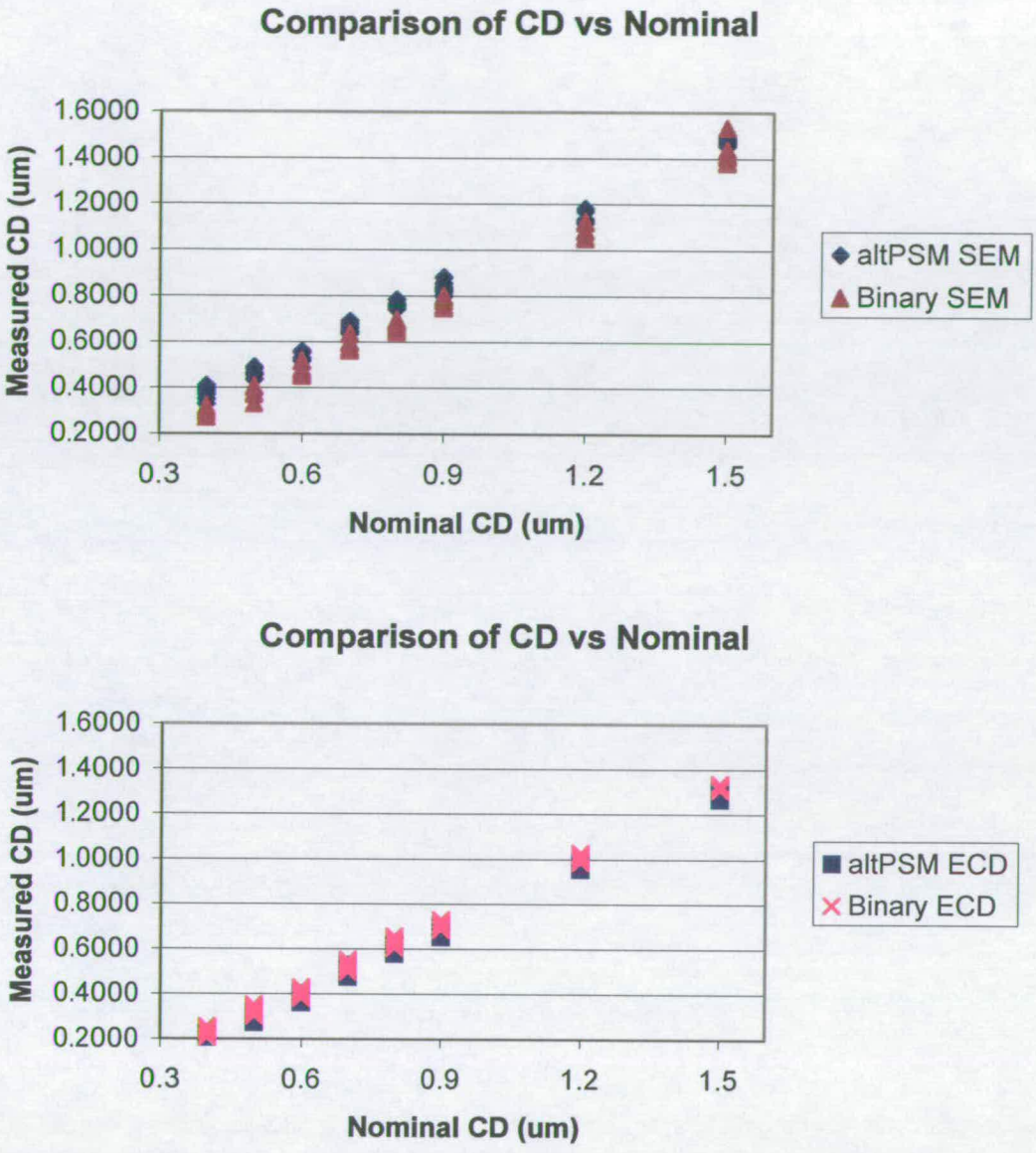

Fig. 5.10. Comparison of SEM CD (top) and ECD (bottom) to drawn linewidth for the binary and altPSM mask patterns.

It can be seen from figure 5.9 that there is an offset between the electrical and SEM measured CDs. In this case the offset for the binary patterns was 63nm whereas for the altPSM it was 165nm, a difference of 82nm. The reason for this difference is not clear as the chrome layer for both binary and altPSM were written on the same tool at the same time. One possibility is that

this could be related to SEM metrology [13], another possibility is that the wall angles of the etch chrome (binary mask) vs the etched chrome plus etched quartz (altPSM on one side of feature) may differ giving a disparity in results on the SEM. If we examine the actual CDs we can see an average difference between binary and altPSM patterns of 16nm in ECD and 66nm in SEM measurements. For binary structures the average CD from the SEM is considerably smaller than for altPSM suggesting the source to be SEM metrology of altPSM structures. The results for SEM and ECD measurements are shown in figure 5.10.

Analysis of the data by nominal dimension is shown in figure 5.11 for both binary and altPSM patterns. Good linearity can be seen for all mask dimensions from 1.5μm to 0.4μm. A very good result for linearity through all duty cycles was also achieved as can be seen in figure 5.12.

Some initial wafer exposures were made and dimensions measured on a CD SEM compared to the mask SEM and ECD measurements for the altPSM patterns. Figure 5.13 shows the relationship. Analysis of this data gives a correlation of 0.995 for both wafer to mask SEM and for wafer to mask ECD.

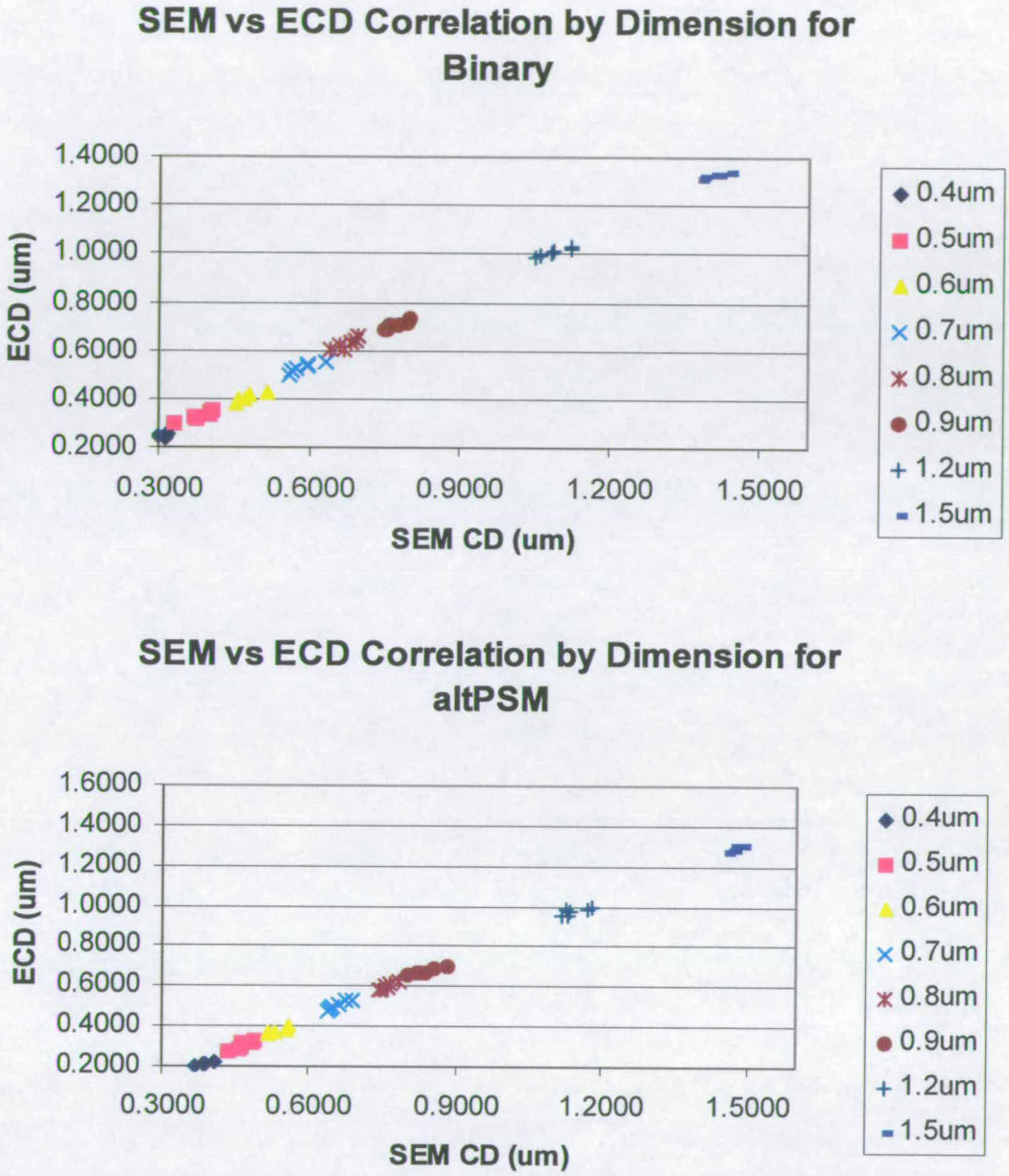

Fig. 5.11. Comparison of SEM and ECD, grouped by nominal dimension, for the binary (top) and altPSM (bottom) patterns.

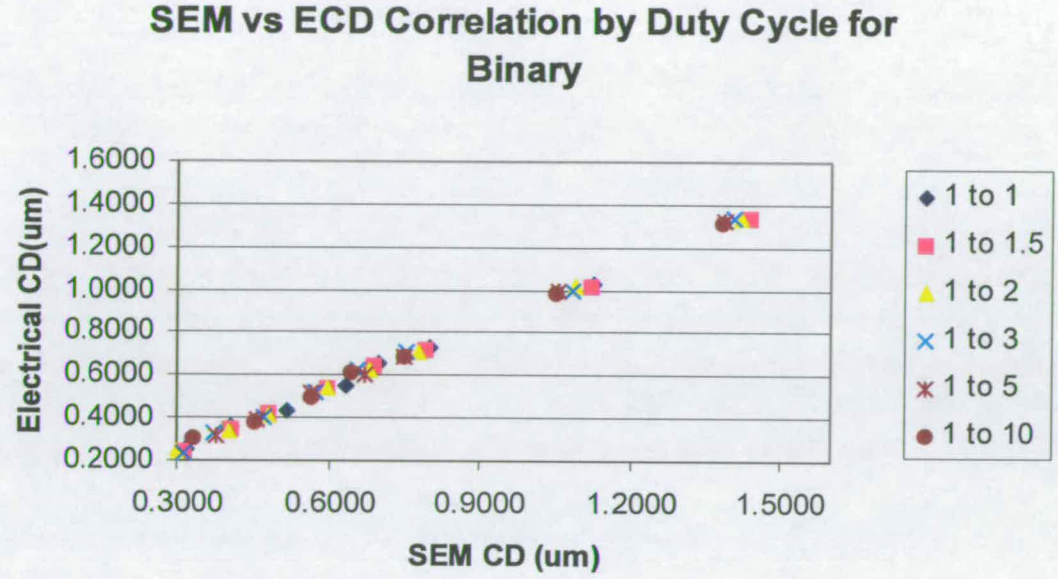

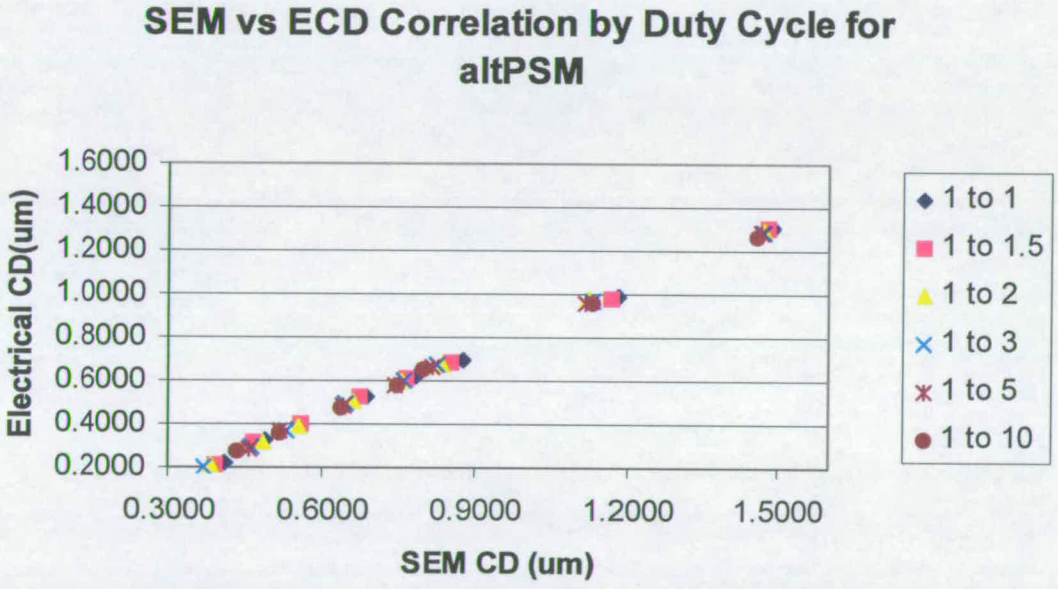

Fig. 5.12. Comparison of SEM and ECD, grouped by duty cycle, for the binary (top) and altPSM (bottom) patterns.

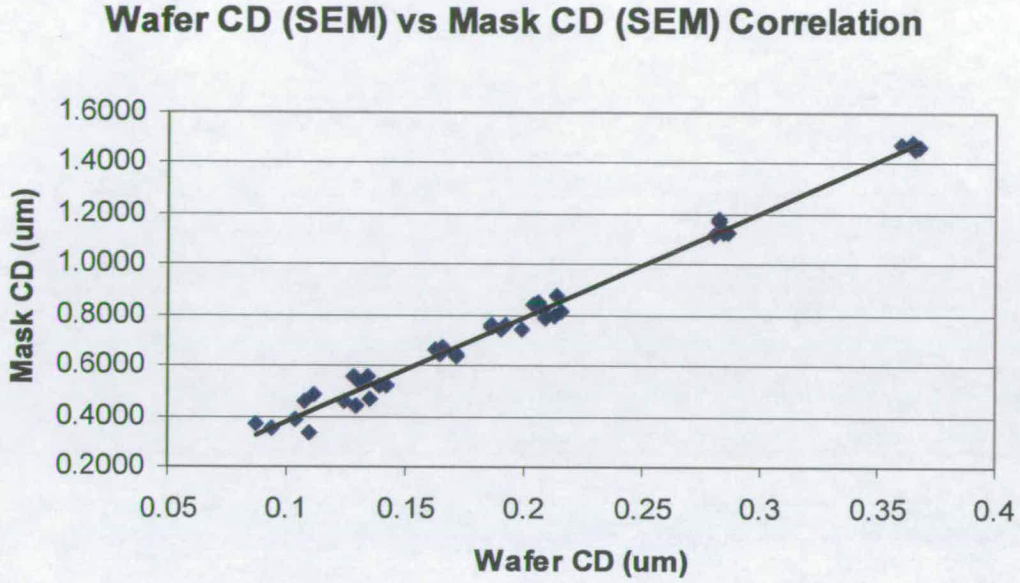

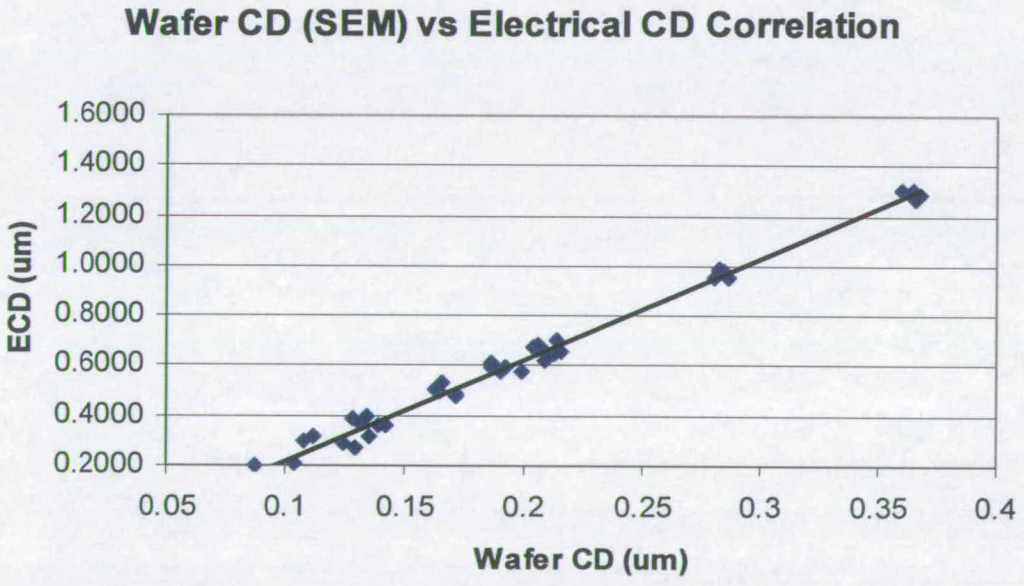

Fig. 5.13. Wafer CD SEM measurement vs Mask SEM measurement (top) and mask ECD measurement (bottom) for the altPSM patterns.

5.4.3) Mask design for practical automated probing

The work so far has shown that that the chrome oxynitride that provides the top surface of the absorber is non-conductive. A solution to overcome this was developed. This involved making openings in the resist over the probe pads in the second masking layer. This layer is used to define the areas where quartz is to be etched creating phase-shifted zones. The etch used to remove the quartz is also suitable to remove the oxy-nitride layer on the chrome and so it is a simple matter to add openings to this second layer over the probe pads, the chrome itself providing an etch stop. The layout for this is shown in figure 5.14.

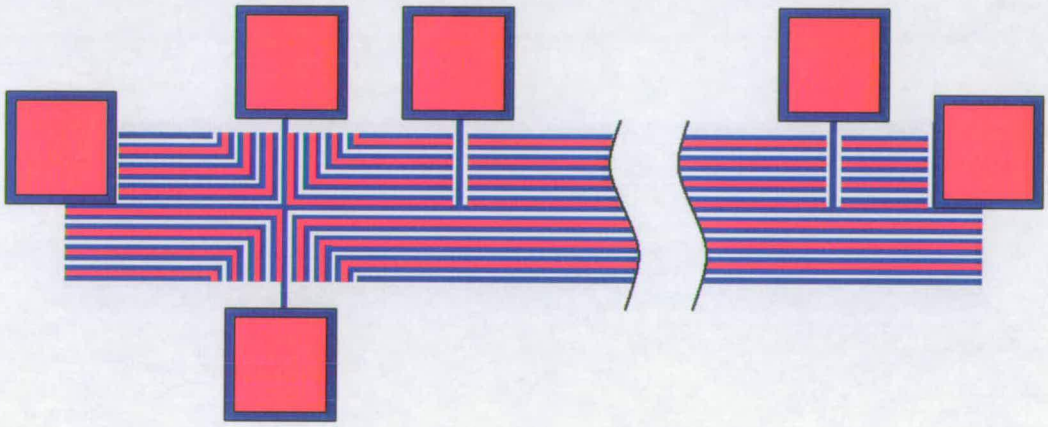

Figure 5.14. Layout of the cross-bridge structure with second layer cut outs shown on the probe pad areas.

The sheet resistance was measured on each of the relevant dimensions and used to calculate the electrical CD at that dimension. The correlation against the design CD was very good with an offset of 110nm and a fit of 1.01. This is shown in figure 5.15.

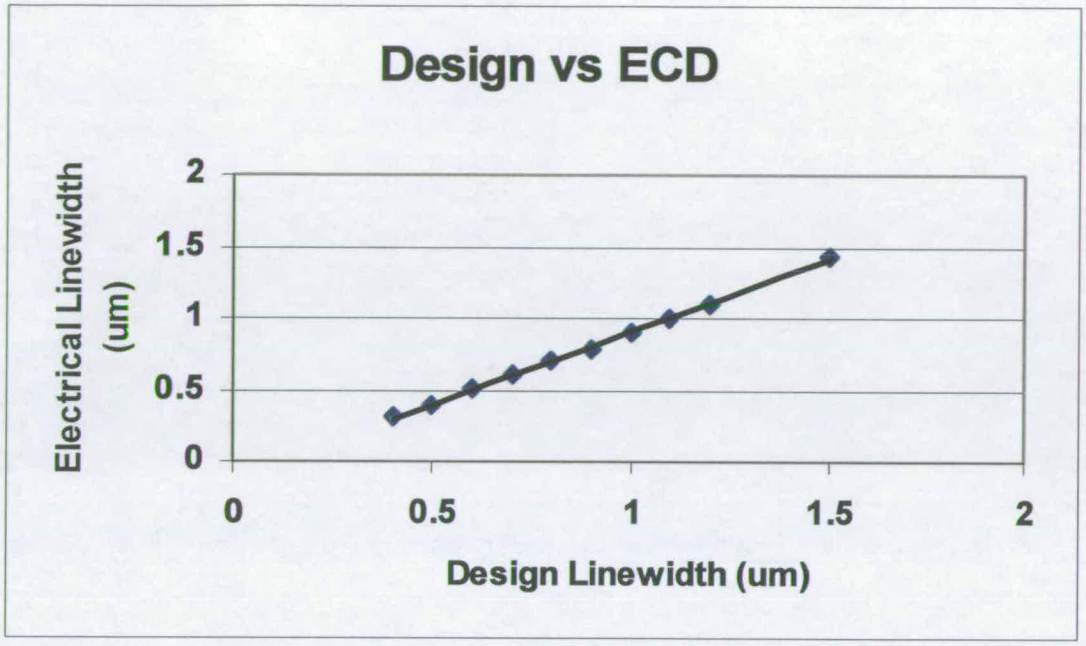

Figure 5.15. Correlation of ECD to designed CD.

Previously we saw an excellent correlation between mask CD SEM measurements and mask ECD measurements of 0.999. On this occasion an AFM was used to establish the fit of physically measured vs ECD data. Once again a very good result was achieved with a correlation of 0.95 as can be seen in figure 5.16.

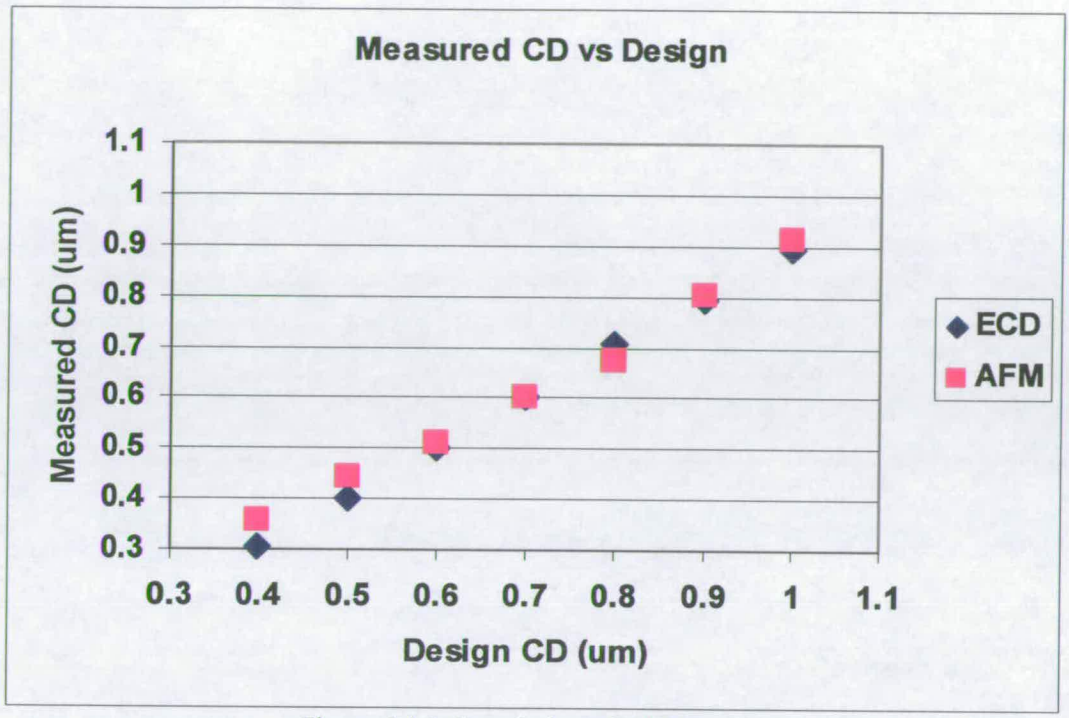

Figure 5.16. Correlation of AFM and ECD.

In this case the data could be easily gathered using an automated 6x2 probe card, a much more manufacturable tool than the manual steerable probes used for the first mask. This technique offers a way that the electrical measurements could be integrated into a manufacturing environment rather than the lab.

5.5) Alignment Test Structure

As has been described above, the phase shifting elements are fabricated by etching into the quartz (synthetic fused silica) substrate. The etch depth required depends on the wavelength of the light intended to be used with the mask, λ, and the refractive index of the substrate material. The etch depth required to give 180° phase shift is calculated using:

$$d = \lambda/2(n - 1) \qquad (1)$$

If the mask is intended for use with 248nm deep ultra-violet (DUV) illumination and quartz n =1.51 then the phase shifter depth should be 243nm. The removal of this material will change the effective capacitance between two chrome lines on the mask. This effect can be used in a test structure to allow the measurement of the overlay between the chrome layouts and the phase shifters. Simulations of simple capacitive structures have been performed using the two dimensional interconnect analysis software Raphael [14]. The simulated structure consists of two or more electrode elements on a quartz substrate with a gap between which represents the phase shifter. The actual test structure on the mask will be an inter-digitated capacitor with hundreds of electrode fingers so the simulation should accurately model the lateral capacitance between two elements. Errors in this value will be introduced by fringe effects if there are too few electrodes and this is indicated by the results in table 5.3.

Number of electrodes	Capacitance between adjacent electrodes
2	2.894412×10^{-17} Fμm^{-1}
3	2.166128×10^{-17} Fμm^{-1}
4	2.129511×10^{-17} Fμm^{-1}

Table 5.3. Results of simulations of capacitive structures with different numbers of electrodes.

It was decided that the simulated structure with 4 metal electrodes should be used as this should give an accurate estimation of the capacitance without the use of a complex simulation. Unlike the normal alternating aperture structures on the mask, these capacitive test structures will have phase shifting elements between each pair of fingers. In addition there will be no overlap between the metal features and the phase shifters when they are correctly aligned. This means that any misalignment will cause a reduction in the amount of quartz being etched between the electrodes. The simulation areas for three different alignments are illustrated in figure 5.17.

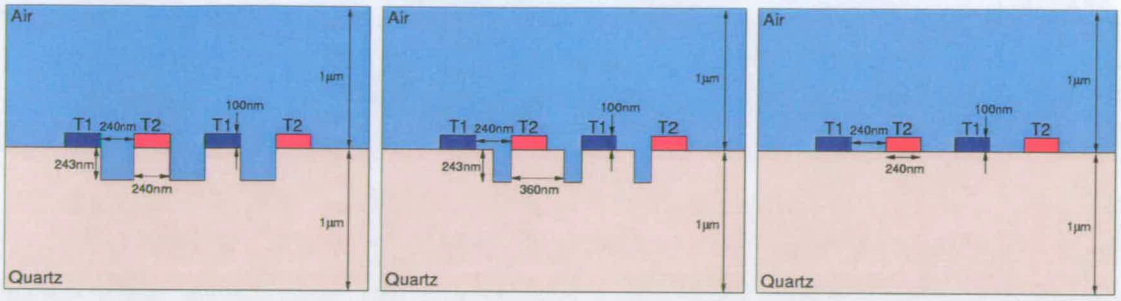

Fig. 5.17. Different possible alignment scenarios: left – zero offset, centre – 120nm offset, right – 240nm offset.

The four metal electrodes in the simulated structure are connected either to 1V (T1) or ground (T2), and so there are effectively three lateral capacitances. The offset was varied from -240nm to +240nm and the capacitance between T1 and T2 was extracted. The results of the simulations are presented in figure 5.18.

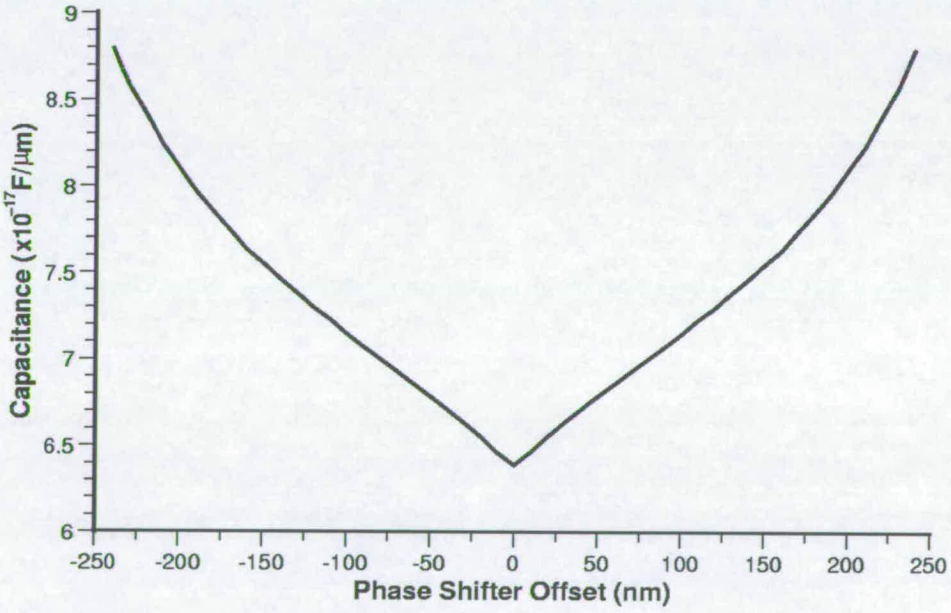

Fig. 5.18. Simulated capacitance plotted against phase shifter alignment.

The simulation results suggested that a progressional off-set technique (POT) [15], [16] could be used to extract the degree of alignment error between the chrome and the phase shifter elements. The test mask fabricated included a number of POT arrays consisting of nine capacitor structures with built in overlay errors ranging from -400nm to +400nm. The test structures have the same designed feature sizes as the simulations and contain a total of 2000 capacitor elements, each being 1000μm long. The simulation data can be used to estimate the actual capacitance of the test structures, assuming there is no misalignment and this is shown in figure 5.19.

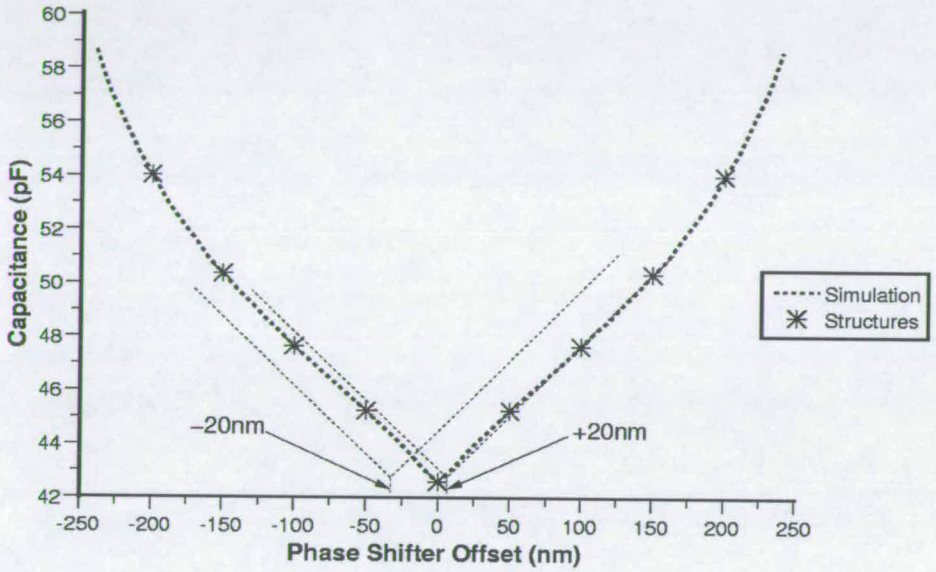

Fig. 5.19. Estimated capacitance of alignment test structures derived from simulation data in figure 5.18.

If there is an actual offset between the chrome features and the phase shifting elements then the results will be shifted away from zero and it should be possible to extract the value of the overlay error.

5.5.1) Equipment Used

The chrome layer on the mask was written on a Gaussian e-beam tool (Mebes 5500) [17] and the phase-shifting layer on a laser based optical tool. Phase etch was performed using an ICP dry etch tool. The phase-shifting layer was designed with an overlap of 200nm over the chrome features. Electrical measurements from both automated and manual probe stations were

measured using an HP-4145B, HP 4062B and Solatron microvoltmeter for CD measurements and an HP-4280 for capacitance measurements.

5.5.2) Overlay measurement

The mask produced was exposed with an offset in the X direction to help verify the suitability of the technique. Each of the progressional offset arrays was measured and the resultant capacitance plotted against designed offset. From this the actual overlay could be extracted as shown in figure 5.20.

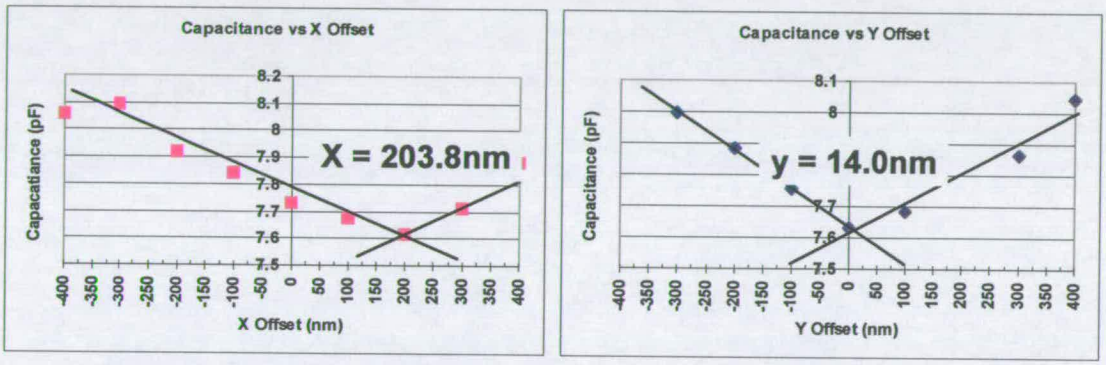

Figure 5.20. Capacitance vs offset and extracted overlay for the progressional offset arrays.

As can be seen the designed off set of 200nm in X could be very well resolved by this technique. The offset in Y of 14nm is well within the manufacturing tolerances of the write tool used for the patterning.

5.6) Conclusions

The initial measurements indicate that it is possible to probe test structures on chrome masks with anti-reflective coatings. However, it was suspected that probe related problems make the measurements less repeatable than when probing directly onto chrome pads where the AR coating has been removed. The building of the second test mask where the quartz etch was used to remove the chromium dioxide anti-reflective coating, showed this to be the case.

Measurements made on Greek cross structures show that the variability of the extracted sheet resistance is reduced by increasing the size of the cross. It is clear that the etching of the phase shifting elements has a strong effect on the geometry of the L-type cross structures and this leads

to large errors in the very narrow crosses which cannot be removed through the use of the correction factor F_A. Future on-mask test structure layouts should use large Greek crosses, or possibly box crosses, for R_S extraction rather than following the minimum feature size of the bridge section. In addition these should be isolated structures as there is no need to use phase shifting elements (which can affect the geometry of the cross) as relatively large features are being printed.

An excellent correlation was made between mask CD SEM measurements and mask ECD measurements for both binary and altPSM patterns. Differences have been demonstrated between CD-SEM and electrical measurements. As expected there is a systematic offset between the ECD and SEM results obtained from the binary structures. What was unexpected was that the phase shifted lines, which appeared to be electrically narrower than the binary structures, were measured on the CD-SEM system as being significantly wider. As both patterns were written on the same tool at the same time and the flourine based etch used to create the phase well does not significantly etch chrome, it is thought that this offset probably originated in the mask CD SEM measurement. In SEM linewidth measurement the threshold selected to define the edge of the feature has a systematic effect on the extracted width. It is likely that the presence of the phase well affects the SEM image so that the tracks appear significantly wider than expected. Charging of the mask in the SEM chamber also affects the measurement of linewidth leading to poor contrast and long testing times.

Overlay measurement tools are typically less expensive than CD measurement tools, however they often suffer from inaccuracies in measurement due to gravity causing a sag in the plate as it is only held at the edge during measurement. Very often it is also impossible to establish what the overlay on the mask was after processing; because these structures use features that are created during the mask processing, they in effect create an artefact that allows the mask to be reviewed and interrogated afterwards. This work has established a method to overcome these limitations through use of a progressional offset capacitive array. The accuracy of these structures appears to be high, however further calibration with production type overlay tools remains to be done.

References

[1] M.G. Buehler, S.D. Grant, and W.R. Thurber, "Bridge and van der Pauw Sheet Resistors For Characterizing the Line Width of Conducting Layers," J. Electrochemical Soc - Solid State Technology, vol. 125, no. 4, pp. 650-654, April 1978.

[2] J.M. David and M.G. Buehler, "A Numerical Analysis of Various Cross Sheet Resistor Test Structures," Solid-State Electronics, vol. 20, pp. 539-543, 1977.

[3] L.J. van der Pauw, "A Method of Measuring Specific Resistivity and Hall Effects of Discs with Arbitrary Shape," Phillips Research Rep., vol. 13, pp. 1-9., Jan 1958.

[4] L.J. van der Pauw, "A Method of Measuring the Resistivity and Hall Coefficient on Lamellae of Arbitrary Shape," Philips Technical Review, vol. 59, no. 8, pp. 220-224, 1958.

[5] "Standard Test Method for Determining the Average Electrical Width of a Straight Thin-Film Metal Line [Metric]," Tech. Rep. F1216M-96, American Society for Testing and Materials, 1996.

[6] C.M. Peyne, A. O'Hara, J.T.M. Stevenson, J.P. Elliott, A.J. Walton, and M. Fallon, "Test Structures for Characterising a Damascene Interconnect Process," in Proceedings of IEEE International Conference on Microelectronic Test Structures, Monterey, CA, USA, March 1997, pp. 151-155.

[7] M. McCallum, S. Smith, A.J. Walton, J.T.M. Stevenson, "Electrical CD characterisation of binary and alternating phase shift masks", Proceedings of IEEE International Conference on Microelectronic Test Structures, Cork, April 2002, pp 7-12.

[8] W.V. Colbran, "Hitachi e-beam lithography tools for advanced applications", SPIE Vol. 1496 (1991), pp. 90-96

[9] M.W. Cresswell, Private communication.

[10] M.W. Cresswell, M. Gaitan, R.A. Allen, and L.W. Linholm, "A Modified Sliding Wire Potentiometer Test Structure for Mapping Nanometer-Level Distances," in Proceedings of IEEE International Conference on Microelectronic Test Structures, Kyoto, Japan, March 1991, pp. 129-134.

[11] M.G. Buehler and W.R. Thurber, "An Experimental Study of Various Cross Sheet Resistor Test Structures," J. Electrochemical Soc - Solid State Technology, vol. 125, no. 4, pp. 645-650, April 1978.

[12] M.I. Newsam, A.J. Walton, and M. Fallon, "Numerical Analysis of the Effect of Geometry on the Performance of the Greek Cross Structure," Proceedings of IEEE International Conference on Microelectronic Test Structures, Trento, Italy, March 1996, pp. 247-252.

[13] E.E. Chain, E.P. Baaklini, "Automated CD measurements with the Hitachi S-6280", SPIE Vol. 2439 (1995), pp. 319-324

[14] Avant!, Raphael Reference Manual, Release 2000.2, 2000.

[15] J.A. Serack, A.J. Walton, and J.M. Robertson, "A Novel Device Structure for Studying Gate and Channel Edge Effects of IGFETs," in Proceedings of IEEE International Conference on Microelectronic Test Structures, Long Beach, USA, pp. 67-72, Feb 1998.

[16] A.J Chester, A.J. Walton, and P. Tuohy, "An Experimental Investigation of EEPROM Reliability Issues Using the Progessional Offset Technique," in Proceedings of IEEE International Conference on Microelectronic Test Structures, San Diego, USA, pp. 218-222, March 1994.

[17] J.M. Chabala, F.E. Abboud, C.A. Sauer, S. Weaver, M. Lu, H.T. Pearce-Percy, U. Hofmann, M. Vernon, D. Ton, D.M. Cole, R.J. Naber, "Extension of graybeam writing for the 130-nm technology node", SPIE Vol. 3873 (1999), pp. 36-48

Chapter 6
Final Conclusions and Future Work

6.1) Introduction

This thesis has reported significant work in the area of understanding and characterising masks for photolithography. The significance of the three dimensional structure of masks has been reported, together with the effects that mask errors have upon the printed image. Defects, especially those on phase-shfting masks, have been shown to be critical to the printed image, as well as being relatively difficult to detect. Suggestions have been made for how the industry can best develop inspections systems that will identify these defects. Finally the increasingly important area of mask feature dimension measurement has been investigated, a new novel electrical CD measurement technique being developed that provides not only more accurate measurements, but also cheaper tools than standard CD-SEM's for on mask metrology. This technique has also been further developed to provide the potential for overlay measurement on altPSM masks. A more detailed discussion of the above summary follows.

6.2) Determining Mask Effects

The three dimensional nature of a photomask was studied in this chapter. AFM was used to establish the depths of quartz that had been removed from the mask to produce the shifted space that produces the one hundred and eighty degree shifted light wave. A special 'boot' tip was used on the AFM to gather information on the side walls of these quartz trenches where an isotropic etch had rounded the corners of the trench and created a slight undercut under the chrome feature. It was found that there seemed to be systematic relationship between the width of the trench and the depth obtained where narrower trenches had significantly deeper trenches. It is thought that this is due to an effect known as inverse RIE lag.

Once the topographic information had been gathered a pixelised representation of the mask was built and a Maxwell solver used to calculate the amplitude and phase of the waves just below the

mask. This showed that the effect of this difference in depth is to ensure that waves that propagate through the shifted space will not have the desired one hundred and eighty degree phase shift. Another effect that must be noted is that there is considerable light scatter within the mask, especially from the corners of the shifted space. This scatter means that less light propagates through the mask at the shifted space and so the intensity of light between shifted and unshifted spaces differs creating an imbalance.

Further simulation was then used to identify the effect of these two phenomena. Aerial images were calculated and two major process metrics, those of depth of focus (DOF) and Image Placement Error (IPE) were calculated. It was found that the DOF was predominantly driven by the phase error, especially for the densest pitches. This effect will have a very major effect upon the process margin of the IC pattern being produced and may render it unmanufacturable. Very large intensity imbalances were calculated leading to IPE's of over 20% of the feature printed, it is likely that this would strongly affect the performance of the IC being produced.

6.3) Mask defect printing and inspection

It is vitally important to ensure that no defects are present on a mask as these will be reproduced on all ICs printed and is likely to lead to loss of performance or even failure of these circuits. With standard binary masks the inspection was straightforward as it was simply a matter of dealing with light (transmissive) and dark (chrome) areas where only the amplitude of the light was important. However with altPSM the defect may not be a simple 'dark' area in the amplitude of the wave, it may be a phase error so inspection tools must take both amplitude and phase of the propagated light into account.

This thesis has reported the use of EMF simulation to calculate the amplitude and phase of propagated waves through masks with modelled defects. This data was then taken and aerial images calculated for 4x lithographic printing systems. These defect sizes and positions were changed in order to calculate the threshold at which they would cause the process to fail and it was found that the limit was not, as was previously thought, when the defects began to be reproduced on the wafer, but rather they cause a disturbance in the aerial image and the dimension of the desired feature would exceed desired tolerances. It was found that the most sensitive position for a defect to occur was not at the centre or edge of a shifted space, but rather

at the mid-point between these two positions. It should be noted that these findings may differ for different types of defects such as irregular shaped defects and those adjacent or in chrome features.

Whilst printing of these masks is on 4x reductions systems, their defect inspection is on 1x systems. This work comparing these two imaging systems led to the observation that, whilst for the 4x reduction systems we need only consider on-axis incident plane waves, the diffraction orders from off-axis points not being gathered by the lens, this is not true for 1x imaging. This work developed a technique to consider all relevant incident waves and calculate the aerial image as seen by the inspection tool. However inspections are further complicated by the use in industry of non-actinic light sources, where identification of an exact one hundred and eighty degree phase shift is not possible. The work here has shown that non-actinic systems are considerably worse than actinic systems at detecting defects. Further that their performance could be improved by changing the defocus and coherence of their imaging, the coherence being the stronger of these two effects.

6.4) Electrical characterisation of masks

Mask metrology has had the serious challenge of having to measure smaller and smaller dimensions on mask. While wafer metrology has overcome this by using Scanning Electron Microscopy (SEM) this technique has some limitations on mask, primarily due to the fact that a mask consists of a conductive metal (chrome) on top of an insulating substrate (quartz.) Some success, e.g. [1], has been achieved in industry mainly due to the chrome having an anti-reflective insulating layer of chromium dioxide on the top. However in altPSM manufacturing this layer is generally removed by the second etch that removes the quartz and creates the phase-shifting space. The resulting bare metal very quickly charges up when scanned by an electron beam and so measurement becomes difficult. SEM metrology tools are also an order of magnitude more expensive than the optical tools that have sustained the industry to date. When this is combined with the fact that only around five percent of masks are at geometries that require this technique, the return on investment is such that very few mask manufacturers can afford to purchase them. An alternative that overcomes both the repeatability problems associated with the charging and is economically viable is therefore very attractive. Electrical CD measurement, which is the subject of this thesis, fits well into both of these requirements.

The structures used in this work were based upon cross-bridge structures. These structures have a Greek cross to establish the sheet resistance of the metal and long bridge structures to obtain the CD. Structures were designed for both binary and altPSM patterns. It was found that if the chrome dioxide anti-reflective coating was left on, only probing using a strongly forced needle could penetrate this layer and obtain a reasonable electrical contact. A novel solution to this was found and a second mask was designed where the phase-shift quartz etch was allowed to also etch the ARC over the probe pads. This allowed good electrical contact to be made and an automated probe station to be used. It also had the advantage of no additional process steps during the manufacture of the mask.

Measurement of the masks found that for the majority of dimensions measured the sheet resistance were independent of the feature size which allowed the same sheet resistance to be used for all features. Electrical measurements of the bridge structures also showed very good repeatability with a standard deviation of ~0.035%. When the ECD calculations are made and compared to SEM CD measurements a correlation of 0.999 for both binary and altPSM features resulted. A systematic offset was obtained between the two measurement types. Wafers were also printed with the features and a wafer CD-SEM used to measure the on wafer CD's. This data showed a correlation of 0.995 against the mask ECD's, a very good result.

The success of on mask ECD led to exploration of other potential electrical measurement structures for masks. Capacitive structures were designed using a progressional offset technique where multiple structures were measured to establish the overlay between the first chrome patterning layer of the mask and the second quartz phase-shifting etch. This work accurately measured a pre-defined offset between the two layers to well within the overlay capability of the write tool used.

6.5) Future Work

A number of suggestions for further work in the area of advanced mask characterisation have arisen from the work presented in this thesis. Chapter 3 showed that a good method needs to be devised to establish the exact trench depth of a shifted space. This is required to ensure that the maximum benefit in process window gain is obtained through the desired one hundred and

eighty degree phase shift of the light propagated through the shifted space and also that no placement error occurs as a result of aerial image intensity imbalance. The AFM data used in this thesis, whilst very accurate, is time consuming to obtain. The data gathered showed a very strong inverse RIE lag, something that must be overcome in order to prevent phase errors and image intensity imbalance. It was found that these in turn caused depth of focus and image placement problems.

In chapter 4 the problem of establishing what kind of mask defects must be identified was addressed and it was shown that conventional non-actinic inspection systems are limited in their ability to find these defects. Work remains to be done to further refine the inspection system imaging parameters to provide a better inspection. As was shown actinic inspection is always better. However, finding a source capable of providing a steady and sufficiently powerful 193nm light for today's technology is likely to be beyond the scope of any project work and involve a great deal of industrial investment.

The electrical mask CD measurements described in chapter 5 were very accurate and quick to obtain. Some further work remains to develop a method where they could easily be applied to binary masks without the need for a second etch to removed the ARC on top of the chrome. Work is also required on inspecting the masks for defects both before and after probing to ensure that no critical defects are generated during this process. It is also possible to take this technique forward to characterise other on mask features, where it may be possible to measure other imaging effects such as corner rounding or serif addition. This would allow this technique to become part of optical proximity correction (OPC) feature characterisation. The work on alignment test structures shows the potential of capacitive measurements for characterising masks. It may be possible to take these forward for further alignment or topography characterisation, most especially with altPSM masks, where the area with the shifted space will have a different capacitance to an unshifted space due to the removal of the quartz substrate.

6.6) Final Conclusions

The work presented in this thesis has shown that understanding the exact structures on advanced masks is essential to ensure that the resulting pattern can be predicted. The work shows that not only must the width of a feature be understood but also the overall topography of it and its

surroundings. The present standard metrology structures used by the industry are relatively large and not a good representation of actual circuit features, this is something that must be addressed by the industry. Application of existing AFM technology has been applied to show how this topography data can be gathered and advanced simulation techniques established to show their effect on imaging. Novel simulation techniques have further been developed to establish what the limitations are for defects to be present on altPSM masks and a new methodology developed to show how mask inspection systems image these defects. Further work has shown how these inspection systems could be improved to provide better inspections.

There also exist limitations, both technical and financial, to the application of CD-SEM metrology to masks. This work introduces a much lower cost alternative that overcomes the charging problem inherent with altPSM masks and offers other electrical based metrology related to alignment that may be applied to masks. It is suggested that this would be a strong candidate for adoption by the mask industry as an alternative to SEM or optical CD measurement.

This thesis has analysed and characterised advanced masks for microlithography, providing a greater insight into the critical nature of having accurate data on the physical features on the mask. The results of this study provide the foundation to develop the appropriate metrology for future mask technologies.

References

[1] P. Nesladek, A. Wiswesser, B. Sass, J. Richter, "Metrology limits of mask process development", SPIE Vol. 6283, (2006)

Appendix A
Published Papers

The following are papers written by the author associated with this thesis which have been presented at an international conference or have been published in a peer reviewed journal.

M. McCallum, R. Gordon, "Determining mask effects in low k1 lithography", Microelectronic Enginering (1999), *A2 – A5*

M. McCallum, R. Gordon, "Mask topography effects in low k1 lithography", SPIE Vol. 4000, (2000), *A6 - A11*

M. McCallum, P. Gabella, G. Shelden, K. Kjoller, K. Miller, "Alternating PSM Mask Performance – A Study of Multiple Fabrication Technique Results", SPIE Vol. 4346, (2001), *A12 – A17*

M. McCallum, "Wavelength dependant mask defect inspection and printing", SPIE Vol. 4562, (2001), *A18 – A24*

S. Smith, M. McCallum, A.J. Walton and J.T.M. Stevenson; "Electrical CD Characterisation of Binary and Alternating Aperture Phase Shifting Masks", International Conference on Microelectronic Test Structures, April 8-11 2002, *A25 – A30*

M. McCallum, S. Smith, A. Lissimore, A.J. Walton, J.T.M. Stevenson, "Electrical Dimension Characterisation of Binary and Alternating Aperture Phase-Shifting Masks", SPIE Vol. 4889, (2002), *A31 - A39*

S. Smith, M. McCallum, A.J. Walton, J.T.M. Stevenson, P.D. Harris, A.W.S. Ross, A.C. Hourd, L. Jiang, "Test Structures for CD and Overlay Metrology on Alternating Aperture Phase-Shifting Masks", International Conference on Microelectronic Test Structures, April 8-11 2004. *A40 – A45*

Determining Mask Effects in Low K1 Lithography.

Martin McCallum* and Ron Gordon#

International SEMATECH, 2706 Montopolis Drive, Austin, TX 78741, USA
* Assignee from Motorola, Colvilles Road, East Kilbride G75 0TG, Scotland
# Assignees from Motorola APRDL, Ed Bluestein Blvd, Austin, TX 78741, USA

With optical lithography driving device-manufacturing capability to subwavelength dimensions, new effects that were once safely ignored are playing a crucial role in determining process quality. One such critical effect results from the consideration of mask topography. The use of advanced photomasks is far from straightforward, especially when confronted with a low k1 process. In this challenging regime, any image model must take into account the effects of the mask topography on the wavefront: any scattering of the light can cause a resultant loss in the already low process tolerance we have. This paper will discuss results we have achieved with the use of atomic force microscopy to characterise the topography of an alternating aperture phase-shift mask. Electro-magnetic field simulation combined with conventional lithography simulation will be used to estimate the effects in the resultant aerial and photoresist images. We will discuss some observed effects upon process depth of focus and image placement from the phase and image intensities resulting from the physical topography of the mask pattern.

1) Introduction

As optical lithography drives IC manufacture to smaller dimensions in order to satisfy economic and technological requirements, we are pushing the fundamental limits of physics. The classical Rayleigh criterion relates resolution to the wavelength and numerical aperture incorporates a variable coefficient, the so called k1 factor, has historically been significantly above 0.5, a region where even completely coherent sources could produce the desired image. However, we are now beginning to work in the region below 0.5, and we are discovering that phenomena we could previously neglect are significant. We must utilise a number of techniques to help us work in the region where k1 is between 0.5 and 0.25 the most significant and widely used of these being phase-shift masks (PSM). Initial work with alternating aperture phase-shift masks (altPSM) revealed many unexpected results that we could not fully explain through our understanding of lithography. Further investigation revealed that if we no longer treat the mask as a planar two dimensional surface, but model the topography with a more rigorous approach involving the solution of Maxwell's equations at the mask, we could explain the observed effects.

2) Mask Topography

Classically we have considered alternating aperture phase-shift masks to be fairly discreet structures with perpendicular sidewalls and right-angled corners. However, as we know from the production of IC's, our drawings do not often resemble reality; this also is the case with masks. To try and provide models that would give a good representation of actual masks, we examined an alternating aperture phase-shift mask built for a 248nm 4X scanner. The mask was built using the 0°/180° phase differential technique with the trench for the 180° achieved in an RIE system. The mask then received a wet etch to reduce the effects of scattering from corners previously reported by a number of researchers [1, 2]. In order to examine the mask structure in a non-destructive manner that would still allow us to use it for lithography after investigation we chose to use atomic force microscopy (AFM). There are a number of commercial tools available to do this; our preferred choice being a Veeco with a 0.18μm 'boot' tip [3]. This 'boot' tip on the Veeco tool has a flared end, allowing us to interrogate

the profile of the reticle to build an accurate picture of the wall angles and any undercuts. Unfortunately any undercut between chrome and quartz cannot be accurately measured with this technique. This also allows for accurate measurement of the actual depth of each trench achieved in the patterned area. This information is important as we normally assess the achieved phase through measurement of a metrology structure on the mask. However, this structure is limited to a minimum dimension of 2μm on mask which only represents structure of 0.5μm on wafer compared to the 0.1μm features in which we are interested (if a 4X magnification system is assumed.) As we know from wafer processing, the difference in topography from 2μm features to 0.4μm features can be great, so it becomes important to be able to look at the individual features in order to establish the depth and profiles achieved in each.

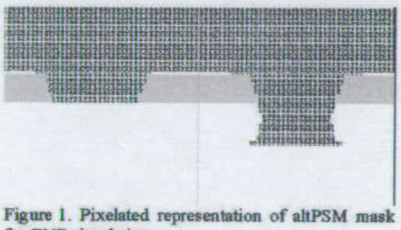

Figure 1. Pixelated representation of altPSM mask for EMF simulation

To build the modeled masks we took a series of measurements from scan plots of the reticle. The data was then used to build masks that we could then feed into a 2D electro-magnetic field simulator. These masks were built to reflect not only the depths that we obtained from the AFM plots but also the wall angles and undercuts observed. The mask simulation files were built in a number of very small 'slices' which were then layered one on top of the other to construct a representation of the mask. This gave a pixelated staircase edge to the features, rather than the smooth rounded edge observed on the actual reticle. Each slice has a defined thickness and refractive index (real and imaginary parts.) The steps that represented a sloping wall were considerably greater than the increment size for each step in the simulation. An example of a mask is shown in figure 1.

Once the masks had been built they were input to a commercially available, two-dimensional electro-magnetic field simulator, ProMAX/2D, developed and sold by FINLE Technologies. This software was used to produce a 'greyscale' output where the intensity and phase are calculated for each pixel studied. This was then be taken and used in a commercially available lithography simulator, PROLITH/3D. The resultant aerial image was calculated. This was then further extended and the post develop photoresist image calculated through simulation.

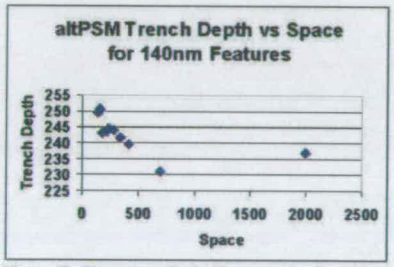

Figure 2. Phase trench depth vs space for 140nm nominal features.

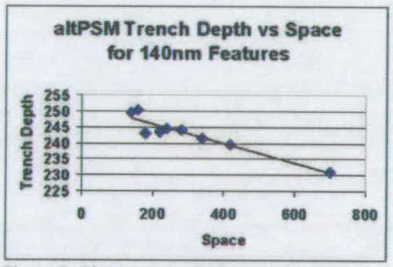

Figure 3. Phase trench depth vs space for 140nm nominal features for the densest duty cycles.

3) Mask Data

The mask studied had various different structures on it, but for this study we chose to use a matrix of structures based upon a nominal 1X dimension of 140nm. For this linewidth a number of different pitches were studied from 280nm out to 2140nm. We also studied a 400nm pitch where the line/space

ratio was changed. The data for the nominal 140nm features is graphed and shown in figure 2. This data does not show a clear relationship between the measured trench depth and the space between the 140nm features. However, if we look at figure 3 this shows the same data with the most isolated pitch (2140nm, a 1:10 duty cycle) removed. A clear trend can be seen where the smaller spaces between the 140nm features have a deeper phase trench. A trend similar to this was previously observed by other researchers where it was explained by inverse reactive ion etch lag [4]. In this case the trend seems to have a fairly good linear fit. Further study of the mask at a 400nm pitch with varying line/space ratios showed no clear relationship between the space adjacent to the line and the trench depth. However the data from the 140nm features and the scatter evident here indicates that more investigation is required.

4) Mask Simulation

Each of the structures from the 140nm nominal features had a soft mask file built to represent the measured depths and profiles. These were then simulated with ProMAX/2D and the resultant greyscale masks calculated. Masks were also built with the same achieved trench depth but with perpendicular chrome and quartz sidewalls as opposed to the rounded sidewalls on the real reticle, to aid in de-coupling the effect of the rounding from the isotropic etch.. For the purposes of this study only the E-polarised waves were considered with an incident angle of 0°. Preliminary work has also shown that the H-polarised waves have a much lesser effect upon the resultant aerial image; if a full rigorous solution is to be pursued, however, these assumptions should not be made.

The greyscale masks from the mask simulation were taken and fed into PROLITH/3D to calculate aerial images for pre-defined stepper conditions of 0.6NA lens, and 0.30σ. These calculated aerial images were then used to calculate the effective phase error against the 180° target [5]. The phase errors for the actual masks and those with perpendicular sidewalls are shown in figure 4. As can be seen it is not clear whether the wet etch has any effect upon the magnitude of the phase error, but for the densest pitches on this mask the errors are considerably lower than those on the equivalent model mask.

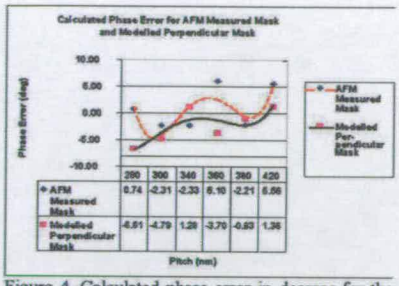

Figure 4. Calculated phase error in degrees for the mask measured by AFM and a model mask with the same trench depth but perpendicular sidewalls.

The imbalance in intensity between the shifted and unshifted areas was also calculated for both the mask measured by AFM and the modeled mask with perpendicular sidewalls, giving the results shown in figure 5. The data shows that the intensity differential follows a linear relationship against pitch for both masks. However, the intensity imbalance is considerably higher for the rounded mask that has received the isotropic etch.

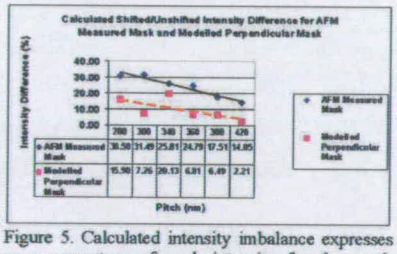

Figure 5. Calculated intensity imbalance expresses as a percentage of peak intensity for the mask measured by AFM and a model mask with the same trench depth but perpendicular sidewalls.

5) Lithography Simulation

The photoresist image formation was also simulated from the greyscale masks and aerial image calculations previously mentioned. For the purposes of this study the process used was: 62nm of anti-reflective coating (ARC) and 400nm of DUV resist. The ARC and resist models were developed at International SEMATECH from chemical and

lithographic analysis of existing processes and the methodology used to produce these models has been published previously [6]. Each mask was simulated and the process window analysed in terms of depth of focus (DOF) allowing a ±10% CD variation. A summary of the results is given in table 1.

AFM Measured Mask

Pitch (nm)	280	300	340	360	380	420
Phase Error (Deg)	0.74	-2.31	-2.33	6.10	-2.21	0.95
Intensity Imbalance (%)	30.58	31.49	25.81	24.79	17.51	14.05
DOF (um)	1.20	1.30	1.30	1.10	1.20	1.25

Modeled Perpendicular Mask

Pitch (nm)	280	300	340	360	380	420
Phase Error (Deg)	-6.81	-4.79	1.38	-3.79	-2.92	1.76
Intensity Imbalance (%)	16.90	7.26	20.13	6.81	6.49	2.21
DOF (um)	0.80	0.90	1.20	1.35	1.60	1.65

Table 1. Summary of phase error, intensity imbalance and DOF for the measured and modeled masks

As can be seen from the table, the DOF is predominantly driven by the phase error, this is strongly shown in the case of the densest pitches for the measured mask where, despite an image intensity imbalance considerably stronger than the modeled mask, the DOF is larger.
The image placement was also studied at nominal best focus to study the effect of the aerial image intensity imbalance; results from this are shown in table 2. This data indicates that the image placement is primarily driven by the intensity imbalance.

AFM Measured Mask

Pitch (nm)	280	300	340	360	380	420
Intensity Imbalance (%)	30.58	31.49	25.81	24.79	17.51	14.05
Image Placement Error (nm)	31	31	25	25	18	14

Modeled Perpendicular Mask

Pitch (nm)	280	300	340	360	380	420
Intensity Imbalance (%)	16.90	7.26	20.13	6.81	6.49	2.21
Image Placement Error (nm)	15	7	20	7	6	2

Table 2. Summary of image placement error and intensity imbalance for the measured and modeled masks

6) Conclusion

AFM was used to extract information on the actual topography, depth and profile, observed on an alternating aperture phase-shift mask. The depth of the phase trench seemed to be related to the space adjacent to the feature being studied, an effect explained by RIE lag. The relationship between mask space and trench depth warrants more in depth investigation. EMF and conventional lithography simulation were used to calculate the effects of this mask topography upon the phase and intensity of the resultant aerial images. For the mask studied there seems to be little effect upon the magnitude of the phase error from the rounding of the mask by the isotropic etch whilst the same technique appears to worsen intensity imbalance. When simulation of photoresist images is studied the depth of focus seems to be primarily driven by the phase error not intensity imbalance whilst the image placement error is governed by image intensity imbalance between shifted and unshifted areas.

7) Further Work

The data obtained here on the effects of mask pattern (line/space size) upon phase trench depth requires much deeper analysis and fuller data collection. The method of fabricating the reticle, especially the types of etch used, require investigation to determine if the observed difference in trench depth can be eliminated through process enhancements. If this effect cannot be eliminated it may result in the present subtractive method of manufacturing alternating phase-shift masks becoming to complex and expensive for use in manufacturing.

References

[1] Exposure Characteristics of Alternate Aperture Phase-Shifting Masks Fabricated Using a Subtractive Process – R. Kostelak et al., J. Vac. Sci. Technol. B, Vol. 10(6) pp/3055-3061, (1992)
[2] Pattern-Dependant Correction of Mask Topography Efects for Alternating Phase-Shifting Masks – R.A. Ferguson, et al., SPIE 2440, pp. 349-360, (1995)
[3] Method for Imaging Sidewalls by Atomic Force Microscopy – Y. Martin et al, Appl Physics Letters, 64 (19), pp.2498-2500, (1994)
[4] Clear Field PSM for 193nm Lithography – P. Schiavone et al., SPIE 3679, pp.582-589, (1999)
[5] Design and Analysis of Manufacturable Alternating Phase-Shifting Masks – R.L. Gordon et al., SPIE 3546, pp.606-616, (1998)
[6] The Formation of Acid Diffusion Wells in Acid Catalysed Photoresists – J.S. Petersen et al., Micro and Nano-Engineering 96, pp.167-174, (1996)

Mask topography effects in low k1 lithography.

Martin McCallum* and Ron Gordon#

International SEMATECH, 2706 Montopolis Drive, Austin, TX 78741, USA
* Assignee from Motorola, Colvilles Road, East Kilbride G75 0TG, Scotland
# Assignees from Motorola APRDL, Ed Bluestein Blvd, Austin, TX 78741, USA

ABSTRACT

With optical lithography driving device-manufacturing capability to subwavelength dimensions, complicated phenomena that were once safely ignored are playing a crucial role in determining process quality. One such critical effect results from the consideration of mask topography. As low k1 processes are entering pilot production, we as an industry are finding that we can no longer simply treat the mask as a simple planar surface and therefore consideration of reticle topography is becoming as important as pre-CMP wafer topography once was. The use of advanced masks in a low-k1 process is far from straightforward however, because any image model describing these processes must now predict the effects of light scatter from the mask that lead to a loss in the already low process tolerance we have. In this paper we will discuss the extraction of mask topography information, using advanced atomic force microscopy (AFM), and the resultant structures simulated through the use of electro-magnetic field (EMF) simulation. We will also verify the accuracy of these simulations by examining the correlation between data gathered on an Aerial Image Measurement System (AIMS) and the simulations. We will further show how we have transferred these EMF simulated masks to a conventional lithography simulator to estimate the effects in the resultant photoresist image. This data will be compared to the actual performance of the masks when exposed using state-of-the-art processing.

Keywords: EMF simulation, AIMS, mask topography

1) INTRODUCTION

As optical lithography drives IC manufacture to smaller dimensions in order to satisfy economic and technological requirements, we are pushing the fundamental limits of physics. The classical Rayleigh criterion relates resolution to the wavelength and numerical aperture incorporates a variable coefficient, the so called k1 factor, has historically been significantly above 0.5, a region where even completely coherent sources could produce the desired image. However, we are now beginning to work in the region below 0.5, and we are discovering that phenomena we could previously neglect are significant. We must utilise a number of techniques to help us work in the region where k1 is between 0.5 and 0.25 the most significant and widely used of these being phase-shift masks (PSM). Initial work with alternating aperture phase-shift masks (altPSM) revealed many unexpected results that we could not fully explain through our understanding of lithography. Further investigation revealed that if we no longer treat the mask as a planar two dimensional surface, but model the topography with a more rigorous approach involving the solution of Maxwell's equations at the mask, we could explain the observed effects.

2) MASK TOPOGRAPHY

Classically we have considered alternating aperture phase-shift masks to be fairly discrete structures with perpendicular sidewalls and right-angled corners. However, as we know from the production of IC's, our drawings do not often resemble reality; this also is the case with masks. To try and provide models that would give a good representation of actual masks, we examined an alternating aperture phase-shift mask built for a 248nm 4X scanner. The mask was built using the 0°/180° phase differential technique with the trench for the 180° achieved in an RIE system. The mask then received a wet etch to reduce the effects of scattering from corners previously reported by a number of researchers [1, 2]. In order to examine the mask structures in a non-destructive manner that would still allow us to use it for lithography after investigation we chose to use atomic force microscopy (AFM). There are a number of commercial tools available to do

this; our preferred choice being a Veeco with a 0.18μm 'boot' tip [3]. This 'boot' tip on the Veeco tool has a flared end, allowing us to interrogate the profile of the reticle to build an accurate picture of the wall angles and any undercuts. Unfortunately any undercut between chrome and quartz cannot be accurately measured with this technique. This also allows for accurate measurement of the actual depth of each trench achieved in the patterned area. This information is important as we normally assess the achieved phase through measurement of a metrology structure on the mask. However, this structure is limited to a minimum dimension of 2μm on mask, which only represents structure of 0.5μm on wafer compared to the 0.1μm features in which we are interested (if a 4X-magnification system is assumed.) As we know from wafer processing, the difference in topography from 2μm features to 0.4μm features can be great, so it becomes important to be able to look at the individual features in order to establish the depth and profiles achieved in each.

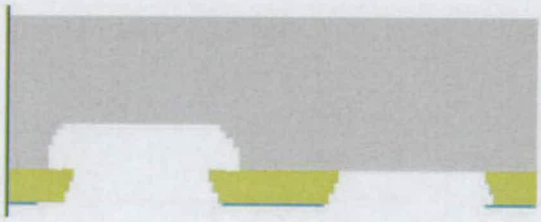

Figure 1. Pixelated representation of altPSM mask for EMF simulation

To build the modeled masks we took a series of measurements from scan plots of the reticle. The data was then used to build masks that we could then feed into a 2D electro-magnetic field simulator. These masks were built to reflect not only the depths that we obtained from the AFM plots but also the wall angles and undercuts observed. The mask simulation files were built in a number of very small 'slices' which were then layered one on top of the other to construct a representation of the mask. This gave a pixelated staircase edge to the features, rather than the smooth rounded edge observed on the actual reticle. Each slice has a defined thickness and refractive index (real and imaginary parts.) The steps that represented a sloping wall were considerably greater than the increment size for each step in the simulation. An example of a mask is shown in figure 1.

Once the masks had been built they were input to a commercially available, two-dimensional electro-magnetic field simulator, ProMAX/2D, developed and sold by FINLE Technologies. This software was used to produce a 'grayscale' output where the intensity and phase are calculated for each pixel studied. This was then be taken and used in a commercially available lithography simulator, PROLITH/3D. The resultant aerial image was calculated. This was then further extended and the post develop photoresist image calculated through simulation.

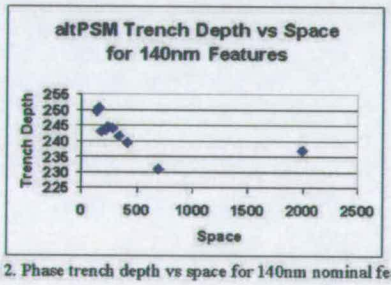

Figure 2. Phase trench depth vs space for 140nm nominal features.

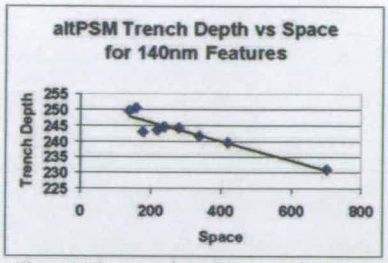

Figure 3. Phase trench depth vs space for 140nm nominal features for the densest duty cycles.

3) MASK DATA

The mask studied had various different structures on it, but for this study we chose to use a matrix of structures based upon a nominal 1X dimension of 140nm. For this linewidth a number of different pitches were studied from 280nm out to 2140nm. We also studied a 400nm pitch where the line/space ratio was changed. The data for the nominal 140nm features is graphed and shown in figure 2. This data does not show a clear relationship between the measured trench depth and the space between the 140nm features. However, if we look at figure 3 this shows the same data with the most isolated pitch (2140nm, a 1:10 duty cycle) removed. A clear trend can be seen where the smaller spaces between the 140nm features have a deeper phase trench. A trend similar to this was previously observed by other researchers where it was explained by inverse reactive ion etch lag [4]. In this case the trend seems to have a fairly good linear fit. Further study of the mask at a 400nm pitch with varying line/space ratios showed no clear relationship between the space adjacent to the line and the trench depth. However the data from the 140nm features and the scatter evident here indicates that more investigation is required.

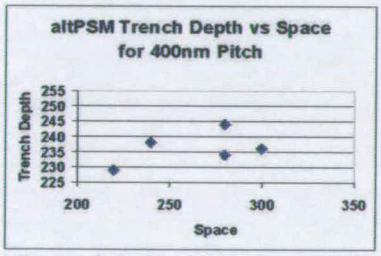

Figure 4. Phase trench depth vs space for 400nm pitch features.

4) MASK SIMULATION

Each of the structures from the 140nm nominal features had a mask file built to represent the measured depths and profiles. These were then simulated with ProMAX/2D and the resultant grayscale masks calculated. Masks were also built with the same achieved trench depth but with perpendicular chrome and quartz sidewalls as opposed to the rounded sidewalls on the real reticle, to aid in de-coupling the effect of the rounding from the isotropic etch. For the purposes of this study only the E-polarised waves were considered with an incident angle of 0°. Preliminary work has also shown that the H-polarised waves have

a much lesser effect upon the resultant aerial image; if a full rigorous solution is to be pursued, however, these assumptions should not be made.

The grayscale masks from the mask simulation were taken and fed into PROLITH/3D to calculate aerial images for pre-defined stepper conditions of 0.6NA lens, and 0.30σ. These calculated aerial images were then used to calculate the effective phase error against the 180° target [5]. The phase errors for the actual masks and those with perpendicular sidewalls are shown in figure 5. As can be seen the phase error shows a linear relationship versus pitch, this matches the relationship seen for the trench depth and pitch.

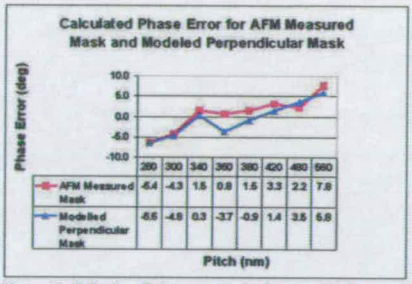

Figure 5. Calculated phase error in degrees for the mask measured by AFM and a model mask with the same trench depth but perpendicular sidewalls.

To aid in checking the accuracy of the simulation, an Aerial Image Measurement System (AIMS) a Zeiss MSM-100, was used to examine the mask. The data from the AIMS system was then analysed and a correction methodology [6] used to correct for known errors in the AIMS tool. The data in figure 6 shows an extremely good correlation between the simulation for the actual mask and the AIMS data.

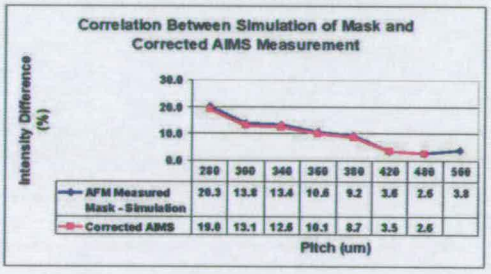

Figure 6. Correlation between EMF mask simulation and AIMS measurements that have been corrected.

The imbalance in intensity between the shifted and unshifted areas was also calculated for both the mask measured by AFM and the modeled mask with perpendicular sidewalls, giving the results shown in figure 7. The data shows that the intensity differential follows a linear relationship against pitch for both masks. However, the intensity imbalance is slightly higher for the rounded mask that has received the isotropic etch.

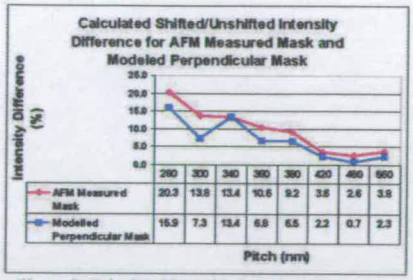

Figure 7. Calculated intensity imbalance expresses as a percentage of peak intensity for the mask measured by AFM and a model mask with the same trench depth but perpendicular sidewalls.

5) LITHOGRAPHY SIMULATION AND PRINTING

To compare the accuracy of the models derived we exposed wafers in the SEMATECH Advanced Tool Development Facility (ATDF). The wafers were exposed on an SVGL Micrascan III using 0.6NA and 0.3 partial coherence. The process used was 62nm of Brewer Science DUV30 BARC and 400nm of Shipley UV6 photoresist. The wafers were measured on a KLA-8100 CD SEM. The photoresist image formation was also simulated from the grayscale masks and aerial image calculations previously mentioned. The BARC and resist models were developed at International SEMATECH from chemical and lithographic analysis of the processes and the methodology used to produce these models has been published previously [7]. Each mask was simulated and the process window analysed in terms of depth of focus (DOF) allowing a ±10% CD variation. A summary of the results is given in table 1.

Pitch (nm)	280	300	340	360	380	420	480	560
Measured DOF (um)	1.2	1.6	1.0	1.0	0.8	0.8	0.8	0.8
Simulated DOF (um)	0.4	0.6	1.0	1.0	1.2	1.4	0.8	0.8

Table 1. Summary of measured DOF vs simulated for the process used

As can be seen from the table, the DOF for the more isolated pitches (340nm out) was fairly accurately simulated. However, for the dense features (280nm and 300nm) the simulated DOF was considerably less than for the actual printed images. The reason behind this unknown, though the use of a 'top down' SEM to measure the DOF may of artificially increased the DOF for the densest duty cycles due to lack of information on scummed resist and resist height loss.

6) CONCLUSION

AFM was used to extract information on the actual topography, depth and profile, observed on an alternating aperture phase-shift mask. The depth of the phase trench seems to be related to the space adjacent to the feature being studied, an effect explained by RIE lag. The relationship between mask space and trench depth warrants more in depth investigation. EMF and conventional lithography simulation were used to calculate the effects of this mask topography upon the phase and intensity of the resultant aerial images. For the mask studied there seems to be a linear relationship between the phase error and the pitch, this corresponds to the relationship observed between space and trench depth. The accuracy of the mask EMF simulation was checked against data gathered from an AIMS tool and an extremely good correlation

found, once the AIMS data had been corrected for known errors. The rounding of the mask by the isotropic etch appears to slightly worsen intensity imbalance. When simulation of photoresist images is studied the depth of focus seems to be primarily driven by the phase error not intensity imbalance, however a balance between these is required. A very good correlation was seen between the simulation results and printing results for depth of focus on semi-dense and isolated structures, this was not the case for dense (1:1 and 1:1.2) duty cycles.

7) FURTHER WORK

The data obtained here on the effects of mask pattern (line/space size) upon phase trench depth requires much deeper analysis and fuller data collection. The method of fabricating the reticle, especially the types of etch used, require investigation to determine if the observed difference in trench depth can be eliminated through process enhancements. If this effect cannot be eliminated it may result in the present subtractive method of manufacturing alternating phase-shift masks becoming to complex and expensive for use in manufacturing.

ACKNOWLEDGEMENTS

The authors would like to thank Alvena Williams and Tony Hare of International SEMATECH for AFM and AIMS measurement data. Thanks also to Mike Recek, Ted Doros and Dan Holladay of International SEMATECH ATDF engineering group for printed wafers and use of their reticle.

REFERENCES

[1] Exposure Characteristics of Alternate Aperture Phase-Shifting Masks Fabricated Using a Subtractive Process – R. Kostelak et al., J. Vac. Sci. Technol. B, Vol. 10(6) pp/3055-3061, (1992)
[2] Pattern-Dependant Correction of Mask Topography Efects for Alternating Phase-Shifting Masks – R.A. Ferguson, et al., SPIE 2440, pp. 349-360, (1995)
[3] Method for Imaging Sidewalls by Atomic Force Microscopy – Y. Martin et al, Appl Physics Letters, 64 (19), pp.2498-2500, (1994)
[4] Clear Field PSM for 193nm Lithography – P. Schiavone et al., SPIE 3679, pp.582-589, (1999)
[5] Design and Analysis of Manufacturable Alternating Phase-Shifting Masks – R.L. Gordon et al., SPIE 3546, pp.606-616, (1998)
[6] Deducing aerial image behavior from AIMS data – R. Gordon, et al., SPIE 4000, to be published, (2000)
[7] The Formation of Acid Diffusion Wells in Acid Catalysed Photoresists – J.S. Petersen et al., Micro and Nano-Engineering 96, pp.167-174, (1996)

Alternating PSM Mask Performance – A Study of Multiple Fabrication Technique Results

Martin McCallum*, Patricia Gabella#, Gil Shelden, Kevin Kjoller& and Kirk Miller&
International SEMATECH, 2706 Montopolis Drive, Austin, TX 78741, USA
* - Assignee from Motorola APRDL, Austin TX, current address Nikon Precision Europe GmbH, Nikon Court, Kirkton Campus, Livingston EH54 7DL, UK
# - Assignee from AMD, Austin TX
& - Veeco/Digital Instruments, Santa Barbra CA

Keywords: alternating PSM, mask topography, AFM

ABSTRACT

In this paper we will discuss the results obtained from five alternating aperture phase-shifting masks (altPSM), each with an identical layout but manufactured using a different technique. We will show the results obtained for mask CD performance measured on a SEM for a number of dimensions and duty cycles. We will show how the results obtained from conventional mask metrology compare with results from advanced analysis including mask topography information obtained using an automated atomic force microscope (AFM). Comparison will be made showing how the metrology structures on the mask compare to the actual structures in the patterning area. A comparison of the results achieved from each mask manufacturing technique will also be made.

1. INTRODUCTION

Today, after much debate and many papers on the subject, we are finally using alternating aperture phase-shifting masks (altPSM) in pilot production. The idea behind this technique and its results are well known [1,2], however its implementation has been a long and tortuous process. We have traditionally been faced with two major problems: layout and mask fabrication. Recently there have been many advances in TCAD; notable amongst them the introduction of the complementary or 'trim' approach using a combination of altPSM and binary masks to photocompose the desired pattern on the wafer [3]. This has overcome, at a price, the layout restrictions we previously had. However, we still do not have a definitive way to best manufacture the masks we desire to make. To try and understand this better International SEMATECH undertook to build masks with identical layouts, suitable for use in conventional altPSM approaches but also similar to those used with the 'trim' approach.

2. MASK DESCRIPTIONS

The five techniques chosen to build these masks varied primarily in the anisotropic etch that formed the 180° phase trench and any subsequent post etch that was used to reduce any effects from the well known intensity imbalance often observed [4]. The methods used were:

A) 90°/270° anisotropic etch with an reactive ion source (RIE)
B) 0°/180° anisotropic etch with an etch tool with an inductively coupled plasma (ICP) source
C) 0°/180° anisotropic etch with ICP tool and additional isotropic wet etch
D) Dual trench (220°/400°) anisotropic etch with RIE tool
E) 0°/180° anisotropic etch with an RIE tool

The mask dimensions varied between 1X dimensions of 80nm to 180nm with duty cycles of: 1:1, 1:1.5, 1:3, 1:5 and 1:10. Additionally trim modules were made with binary overlay for 1:3, 1:5 and 1:10 duty

cycles. Modules for mask metrology were also added. The layout for the whole mask is shown in figure 1. Three manufacturers were used to make the five masks.

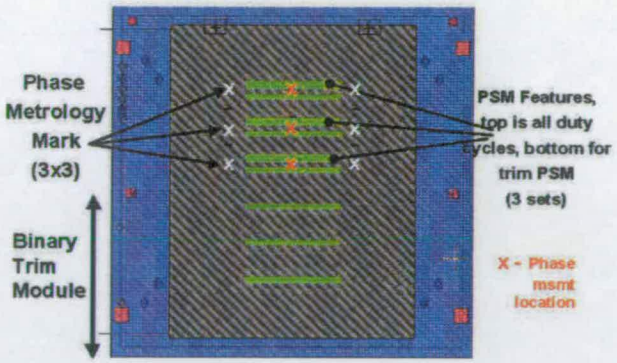

Figure 1. Mask layout showing the phase-shift and binary features as well as metrology structures.

Three manufacturers were used to manufacture the five masks.

3. MASK CD PERFORMANCE

Three of the masks were manufactured using shaped beam e-beam tools and two with a raster scan tool. Figure 2 shows there was no clear difference between any of these groups. Reticle A shows very good linearity down to 320nm on mask (80nm 1X). The other masks did not achieve linearity across all duty cycles but individual duty cycles were linear, although they may not of achieved their target CD's.

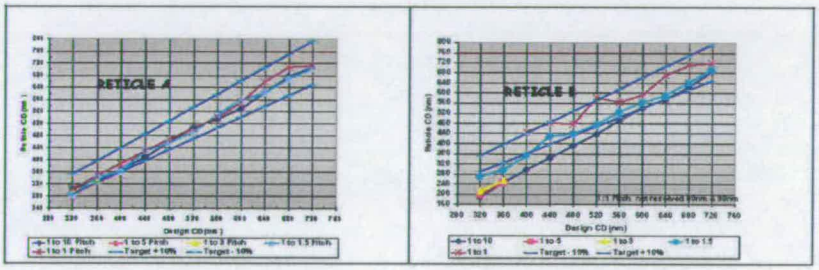

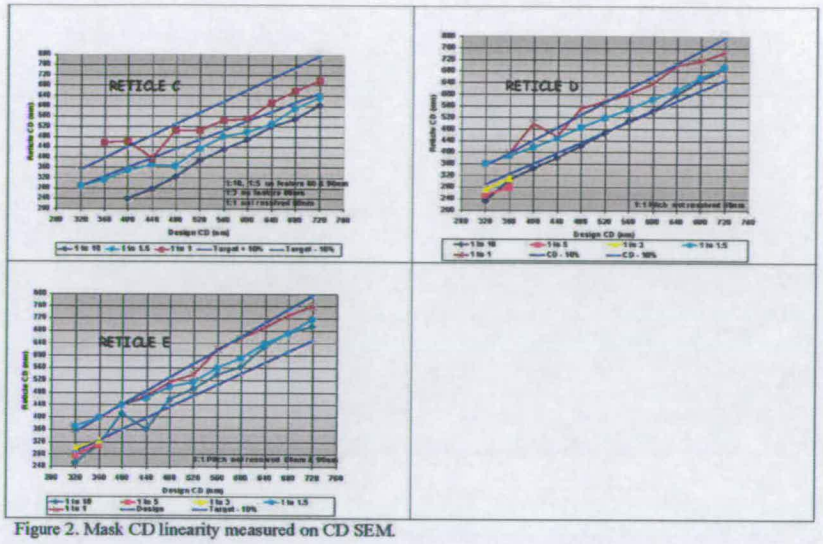

Figure 2. Mask CD linearity measured on CD SEM.

The image fidelity also varied widely between the five masks. If we examine figure 3 we can see that reticle A has much better defined chrome features than reticles B and D. The image quality does not seem to directly correlate with the type of write tool used, this would suggest the actual mask lithographic process is the critical factor. The phase shifted region, written in all cases by a laser write tool, has the worst image quality on mask A. Again this suggests the actual process used governs the image quality.

Figure 2 shows that not all duty cycles could achieve their target CD. The proximity effects at 80nm, 100nm and 130nm (1X) are shown in figure 4 for all reticles. It is clear to say that reticle A once again has the best performance, no other masks achieving performance within the CD specifications of ±10%.

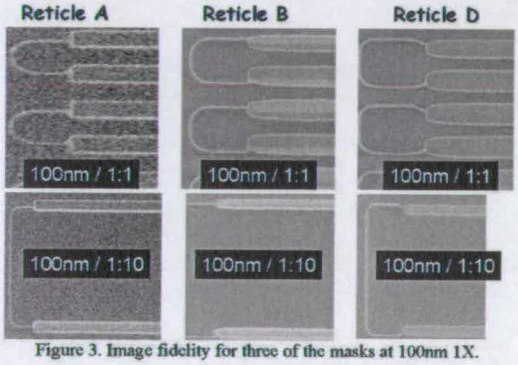

Figure 3. Image fidelity for three of the masks at 100nm 1X.

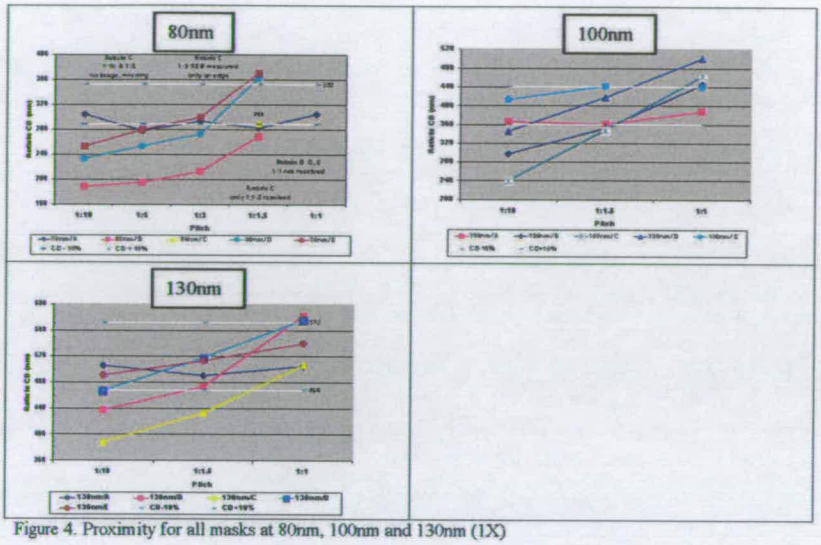

Figure 4. Proximity for all masks at 80nm, 100nm and 130nm (1X)

4. METROLOGY STRUCTURE DATA

The phase metrology structures on the mask were measured on a Lasertec 248nm tool on a 5μm grating. The depth of the phase trench was also measured on an automated Veeco Metrology Dimension 9000M-PM atomic force microscope (AFM). The depth measured was used to calculate the phase using material constants of n = 1.510288, k = 0. The depth taken was the difference between the 0° and 180° openings. This data is shown in table 1 where there is a very good correlation between the Lasertec direct phase measurement and the calculated phase.

	Ret A	Ret B	Ret C	Ret D	Ret E
Delta Phase Depth (nm)	254.7	241.9	245.4	247.7	248.4
Phase Calculated from Depth (deg)	188.6	181.8	179.2	183.5	184.0
Lasertec Phase (deg)	187.1	181.0	179.7	183.2	182.9
Delta Phase - Calculated to Lasertec	1.5	0.8	-0.5	0.3	1.1

Table 1. Calculated phase from phase depth and measured phase from Lasertec tool.

5. PATTERN STRUCTURE DATA

In figure 5, the etched trench depth in each mask is plotted as a function of the space width. A clear trend can be seen where the smaller spaces have a much deeper phase trench. It is important to note that this trend is true for all of the etch techniques used. This trend had previously been noted by other researchers [5] who used only an RIE etch, however this data indicates the etch tool used does not seem to be the primary source of the variation, this may be due more to pattern loading. Examining the graph we can see

that the depth is fairly constant for the larger openings. However when we reach about 400nm (1X) openings the trenches begin to deepen, the rate of depth change then increases when we reach about 150nm (1X). No good fit was found to this rate of depth change.

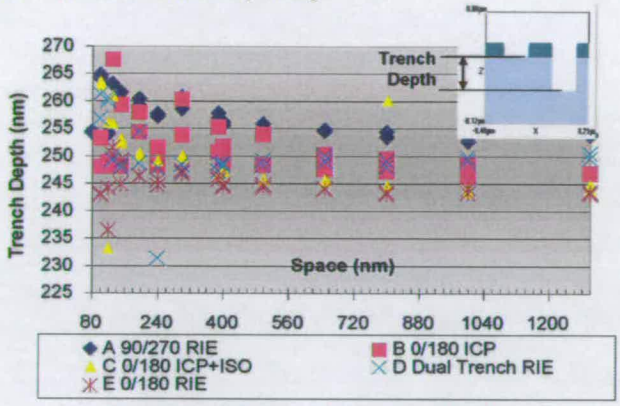

Figure 5. Trench depth vs. etched opening width (1X).

A very important piece of data obtained was the difference in depth seen between the different trench widths. Table 2 shows the depth range for each of the masks and also the calculated phase difference this corresponds to. A very large differences in phase can be seen, much beyond the phase control called for in the ITRS roadmap. Of concern is the difference between the very large features (>1200nm in figure 5) and the smallest. The large features correspond to the dimensions of the features used for mask metrology. These features, as can be seen in table 1, achieved close to the 180° target. However the difference in phase indicated in table 2 would suggest that for the smallest features the phase achieved is considerably off that desired. This phase error would strongly interact with any aberrations present in the lens.

Reticle	Depth Range (nm)	Phase (deg)	Etch
A	12	9.0	RIE 90/270
B	22	16.2	ICP 0/180
C	31	22.7	ICP + ISO 0/180
D	30	22.1	RIE 220/400
E	15	11.2	RIE 0/180

Table 2. Range of trench depths and corresponding calculated phase difference.

6. CONCLUSION

Masks have been built with the same layout but using five different manufacturing techniques. The image quality of the chrome layer varied but did not seem to correspond to the type of mask writer used, it would appear that the process used is the dominant factor. All masks could achieve their target phase in the metrology structures of 5µm, where a good correlation was found between direct phase measurement using a Lasertec tool and the phase calculated from depth measurements taken by AFM. The phase trench depth in the smallest spaces, corresponding to the most critical dimensions, was found to be greatly different to the depth in the metrology structure. The corresponding phase difference was found to be up to 22°. No clear relationship was found between the type of etch used and the phase trench depth change indicating that another factor, perhaps pattern loading, is the critical factor defining the trench depth change.

ACKNOWLEDGEMENTS

The authors would like to thank Mike Bishop of International SEMATECH, Luis Ortiz of KLA-Tencor, Faris Modawar, Matt Williams and Rene Owens for the Reticle Technology Centre for much of the mask metrology work.

REFERENCES

1. M.D. Levenson, N.S. Visanathan, R.A. Simpson, "Improving resolution in photolithography with a phase-shifting mask", IEEE Transactions on Electron Devices, Vol ED-29, No. 12, pp.1828-1836, 1982.
2. M.D. Levenson, D.S. Goodman, S. Lindsey, P.W. Payer, H.E. Santini, "The phase-shifting mask II: Imaging simulations and submicron resist exposures", IEEE Transactions on Electron Devices, Vol. ED-31, No. 6, pp.753-763, 1984.
3. M.E. Kling, N. Cave, B.J. Falch, C.C. Fu, K.G. Green, K.D. Lucas, B.J. Roman, A.J. Reich, J.L. Sturtevant, R. Tian, D.R. Russell, L. Karklin, Y.T. Wang, "Practising extension of 248 DUV optical lithography using trim-mask PSM", SPIE 3679, pp.10-17, 1999.
4. M. McCallum, R. Gordon, "Mask topography effects in low k1 lithography", SPIE 4000, pp.695-700, 2000.
5. P. Schiavone, F. Lalanne, A. Prola, "Clear Field PSM for 193nm Lithography", SPIE 3679, pp.582-589, 1999.

Wavelength Dependant Mask Defect Inspection and Printing.

Martin McCallum

Nikon Precision Europe GmbH, Nikon Court, Kirkton Campus, Livingston, UK

ABSTRACT

In this paper we use simulations to establish the size of quartz defects we need to detect in alternating aperture phase shifting masks (altPSM) when imaged in high NA 248nm and 193nm 4X exposure systems. Such as those that will be used at the 130nm and 100nm technology nodes. Data will be presented showing that smaller defects in the centre of the shifted space than at the edge of the space cause the allowable CD variation to be reached. It will be shown that the most sensitive position for a quartz defect in a shifted space is not at the edge or centre of the space, but rather at a point between these two. We will then use advanced simulation techniques, that take into account the extra non-planar incident waves we must consider in 1X imaging, to establish how these defects are 'seen' by 1X actinic and non-actinic mask inspection systems. The relatively large effect upon the transmitted aerial image of a defect in an actinic inspection, especially for defects in the centre of the shifted space, when compared to a non-actinic inspection will be shown.

Keywords: alternating PSM, actinic inspection, quartz defects, high NA

1) INTRODUCTION

In lithography today we are rapidly developing new exposure tool systems that are using lower and lower wavelengths of light to print the features that are required by today's advanced IC devices. However, this is not enough and we are utilising other techniques such as phase-shifting masks to help. In combination this leads to a great increase in the complexity of the masks and their inspection becomes very challenging. In particular the use of alternating aperture phase-shifting masks (altPSM), first proposed by Levinson and co-workers in 1982 [1], are just now being introduced into pilot manufacturing and so the need to complete a rigorous inspection of a production mask is only now facing us as a 'must do'.

To successfully inspect a mask we must consider two major factors: what types and dimensions of defects are critical and is the inspection tool we are using capable. Establishing the size of defect we have to detect is very difficult, as these defects are at or around the limits of mask lithography and processing, making controlled production for testing very difficult. To overcome this we can use simulation to predict the effects upon the desired image of the defects under study. The majority of lithography simulators use approximations to produce an aerial image from an altPSM. These approximations do not take into account the losses that occur from scatter in the mask, and therefor produce aerial images with equal intensity between the shifted and unshifted spaces. To produce a more accurate simulation, which takes into account losses in the mask substrate, we must accurately establish the amplitude and phase of the light from both of these regions. To do this we can utilise electro-magnetic field simulation (EMF) to establish a more accurate picture of the light that has propagated through the mask. Fortunately much work has been completed in this field and today a number of simulators have been developed that can be used to calculate this [2,3]. In this paper one such simulator, TEMPEST, has been used to complete these calculations. However, judging whether the tool is capable remains very much an empirical process. We will demonstrate in this paper some work simulating 1X inspection systems, both actinic and non-actinic, and the type of aerial image a transmission inspection on these tools may produce.

2) METHOD

The EMF simulations used in this paper were calculated using the TEMPEST simulator originally developed at UC Berkeley [2]. The input files for this, as well as the aerial images from the propagated waves, were produced using the Interplay and Aerial products from Panoramic Technologies. The dimensions were obtained using some in-house programs written in MATLAB.

Firstly it is important to establish the defect free process window, so we may then confirm the effect of the defect under study. The defect free aerial images produced were analysed and the threshold giving the desired feature dimension

obtained. Once the aerial images in the defect cases were calculated, this threshold was used to give the dimension for each case.

To represent the 130nm technology node a mask with a 90nm line and 170nm space was simulated, (in all cases in this paper the dimensions quoted are the 1X, i.e. on wafer dimensions, the only exception being the defect dimensions, which are on mask dimensions.) For this node we chose a 248nm 4X exposure tool with a NA of 0.75 and partial coherence (σ) of 0.3. For the 100nm node a mask with a 70nm line and 130nm space was used imaged in a 193nm 4X scanner with a NA of 0.78 and partial coherence of 0.3. These exposure tools are examples of the types expected to be used at these nodes. Simulations using this 193nm tool were also run using a 70nm line with 350nm space, and 50nm line with 350nm space. The defects studied were idealised square defects placed in the shifted space. For the 90nm line/170nm space and 70nm line/130nm space cases the defect was placed either in the centre or edge of the shifted space. For the 70nm line/350nm space and 50nm line/350nm space the defect size was fixed and its position within the shifted space varied.

3) DEFECT PRINTABILITY RESULTS

3.1) Defect size

Figure 1 shows the defect free process window for the 130nm case to be 0.3µm and 0.25µm for the 100nm case (in the figure only one side of focus is shown). The critical dimension (CD) of the 130nm node and 100nm node with defect cases is shown in figure 2. For each node the CD has been calculated at best focus and at the defocus value at the edge of the defect free process window. It is interesting to note that the actual printing of the defect does not set the process window, it is the disturbance of the aerial image and the change in CD (a CD tolerance of ±10% has been allowed,) that defines the critical defect size. In the 130nm node case centre defects are tolerable up to 140nm. For edge defects it was greater than this; in both cases the defects are more critical at best focus than at defocus. At the 100nm node the centre defects of 100nm and greater result in more than 10% CD variation as do edge defects of 150nm or greater. Again best focus is more sensitive than defocus. For both node cases, the defocused aerial image is more tolerant of the defects, this is likely due to the fact that in these features the CD is smaller when defocused, so when the aerial image is broadened by the defect it has more margin until it exceeds' the maximum allowable CD.

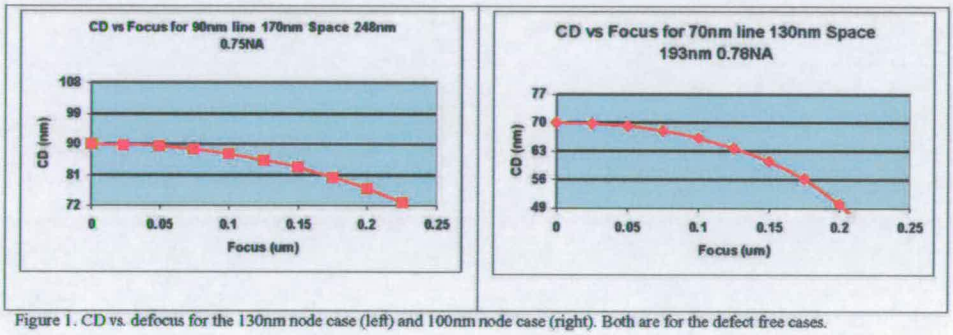

Figure 1. CD vs. defocus for the 130nm node case (left) and 100nm node case (right). Both are for the defect free cases.

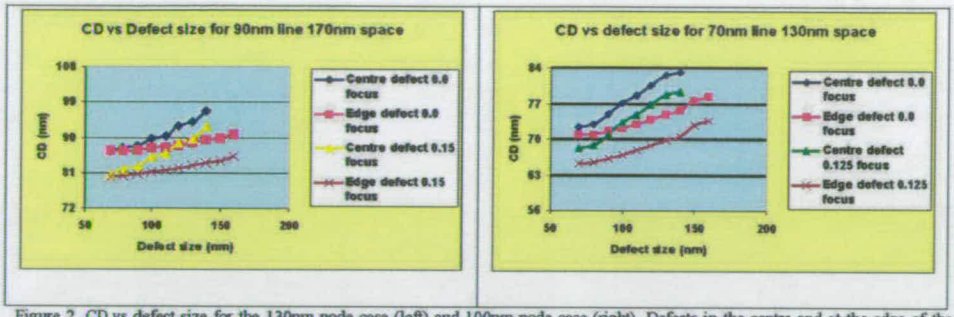

Figure 2. CD vs defect size for the 130nm node case (left) and 100nm node case (right). Defects in the centre and at the edge of the shifted space are shown at best focus and at defocus values equating to the edge of the defect free process window.

3.2) Defect position

To study the effect of the defect position a number of simulations were run where the defect dimension was held constant but its position within the shifted space varied. This work was completed for one of the semi-dense cases already used and more isolated cases. Three features were used: 70nm line with 130nm space (the defect being 130nm), 70nm line with a 350nm space (the defect being 130nm,) and 50nm line with a 350nm space (the defect being 100nm.) For all, the imaging system was the 4X 193nm scanner, 0.78NA and 0.3σ. Figure 3 shows the CD vs position of the defect edge from the edge of the shifted space. The semi-dense cases studied earlier showed that a defect in the centre of the shifted space had much more effect than one at the edge. The left plot in figure 3 shows that the effect of the defect in the semi-dense case (70nm line/130nm space) is again much greater in the centre, but the maximum effect is when the defect is mid-way between the edge and centre. In the 70nm line/350nm space, the defect has the largest effect upon the feature dimension when it is ~35nm from the edge of the chrome feature as can be seen in the middle plot of figure 3. By the time the defect is ~105nm away in the best focus case the CD variation is less than 10%. For the defocus case the defect must be more than 175nm away before the CD variation is below 10%. When the linewidth is reduced to 50nm the 100nm defect causes the largest CD variation when ~70nm from the edge, this can be seen in the right plot in figure 3. At best focus this defect must be more than 140nm from the edge for a variation below 10%, however when defocused this increases to greater than 175nm.

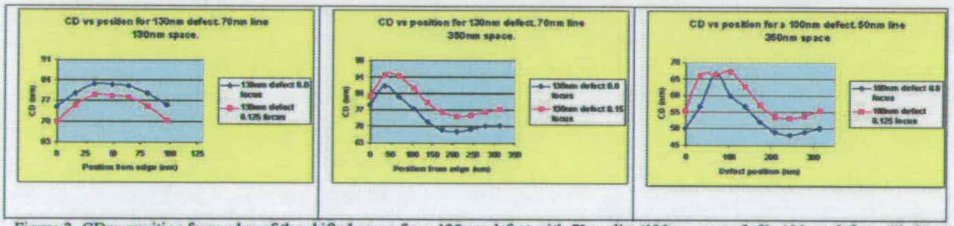

Figure 3. CD vs position from edge of the shifted space for a 130nm defect with 70nm line/130nm space (left), 130nm defect with 70nm line/350nm space (centre) and a 100nm defect with a 50nm line/350nm space (right). The imaging tool simulated was 4X 193nm, 0.78NA, 0.3σ.

Examination of the CD variation versus defocus for the defect free isolated structure situations, with these linewidths, is shown in figure 4. These plots indicate that as the defocus increases so does the CD, this is the opposite of the previously studies cases shown in figure 1. In the case of more isolated features such as this, the defects actually have more effect upon the CD as they broaden further an already widening aerial image.

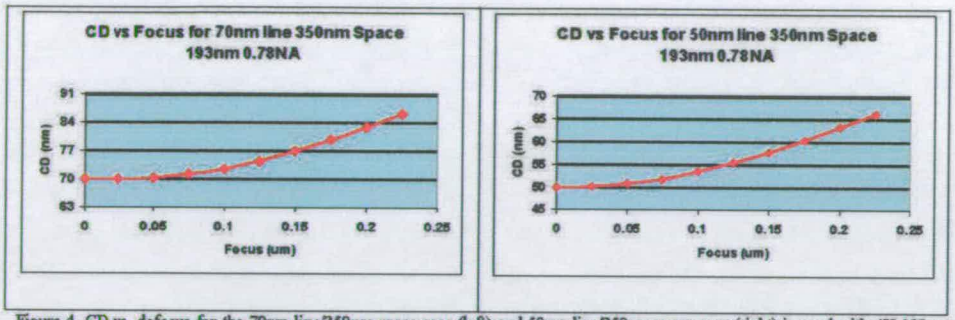

Figure 4. CD vs. defocus for the 70nm line/350nm space case (left) and 50nm line/350nm space case (right) imaged with 4X 193nm, 0.78NA, 0.3σ. Both are for the defect free cases.

4) DEFECT INSPECTION

Many of the mask inspection systems we use today are optically very different from the exposure tools the masks are used in. While they may use transmission, as we do for exposure, they may also add to this a reflected inspection. Another major difference is that they tend to be 1X imaging tools, whereas the exposure tools are in the main 4X reduction systems. Simulation of a 1X imaging system compared to a 4X system is complicated by the many more diffraction orders gathered in the 1X system. To compensate for this we can no longer simply take zero angle incident waves but must also include non-perpendicular incident waves [4]. The relative source positions of these should be calculated to take into consideration not only the wavelength being used but also the lens NA and the domain being studied.

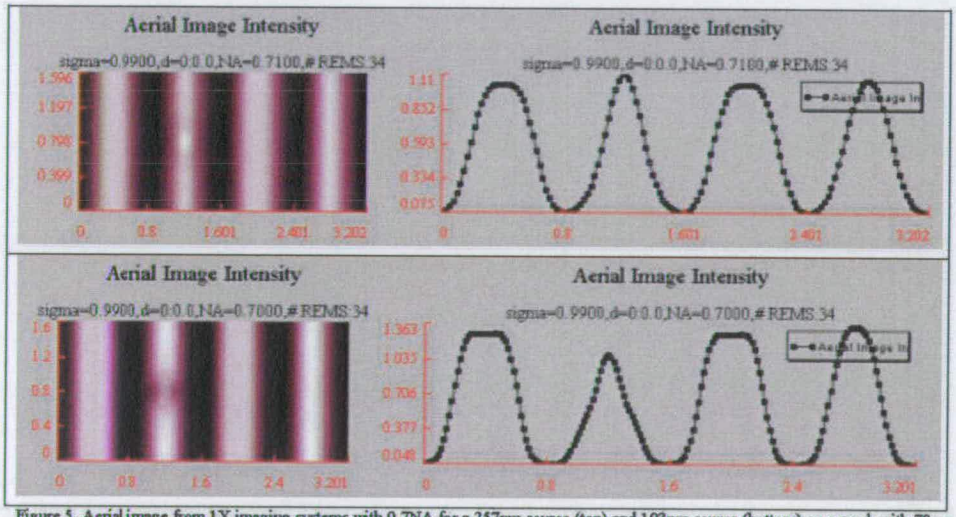

Figure 5. Aerial image from 1X imaging systems with 0.7NA for a 257nm source (top) and 193nm source (bottom) on a mask with 70nm line/130nm space and a 100nm defect in the middle of the shifted space.

Actual inspections of photomasks are further complicated by the use of non-actinic wavelengths. Some of the latest tools use solid-state sources emitting at 257nm [5]. Considering a transmissive imaging system, we have calculated the aerial image produced by this. We have assumed a NA of 0.7, partial coherence of 0.99 and the relevant incident orders of light (from the planes of incidence being restricted by periodicity). The aerial images for a 257nm system and 193nm illuminated system, for the 70nm line/130nm space, with 100nm centre defect are shown in figure 5. The figure shows a view of the aerial image intensity to the left and a cross section through the defect on the right. As can be seen the aerial image is not greatly disturbed by the defect in the 257nm system (top) but is much more greatly disturbed in the 193nm illuminated system.

Simulations were also made for the 70nmline/130nm space case with a 150nm defect at the edge of the shifted space. The optical systems were assumed to be the same and the aerial images are shown in figure 6. For the 257nm system the edge defect causes a much greater disturbance in the aerial image than for the centre defect, though again the 193nm illuminated system is more greatly effected.

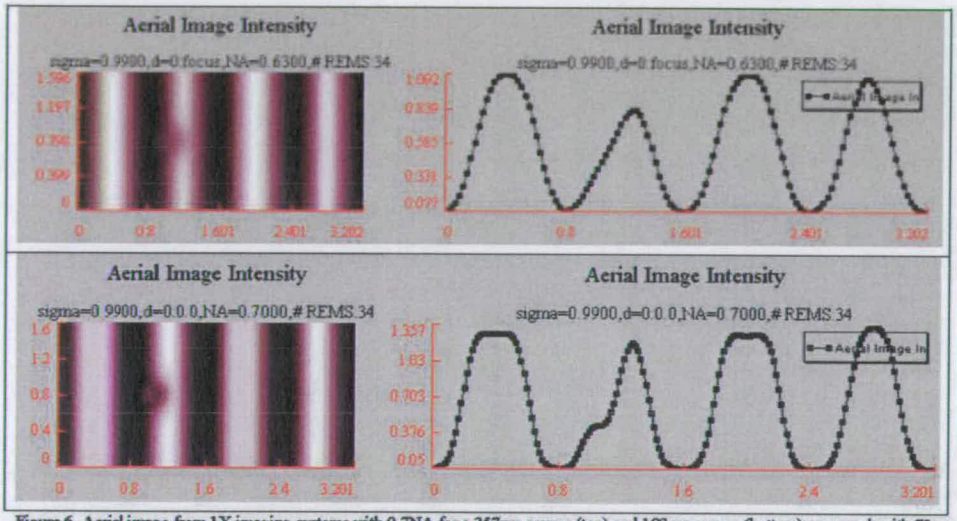

Figure 6. Aerial image from 1X imaging systems with 0.7NA for a 257nm source (top) and 193nm source (bottom) on a mask with 70nm line/130nm space and a 150nm defect at the edge of the shifted space.

To further explore the capability of the transmissive inspection systems simulations were run for both illumination wavelengths using higher NA lens settings. Figure 7 shows the aerial images for 70nm line/130nm space with 100nm centre defect for tools with 257nm source (top) and 193nm source (bottom). The left-hand plot shows a NA of 0.8 and the right hand a NA of 0.9 in each wavelength. It can be seen for the 257nm tool that increasing the NA to 0.9 does make the aerial image at the defect more prominent, however when compared to the 193nm source the difference is still significantly less.

5) DISCUSSION

The dimensions of the defects calculated in this work can be compared to the ITRS roadmap, a summary of which is shown in table 1. The roadmap calls for a defect limit of 100nm at the 130nm technology node, the work here indicated that defects up to 140nm were tolerable for the case studied here. At the 100nm technology node the ITRS value is 80nm, this compares to 100nm derived here. It should be noted that the cases studied here in no way cover all of the potentials for these nodes so it is easily possible that more sensitive cases exist. The aerial image has not been coupled into the resist in these studies, this

may also heighten the effects. One very interesting observation was that in all cases studied the most sensitive position for a defect is between the edge and centre of a shifted space, not at either extreme.

The 1X inspection simulations indicate that actinic inspection is significantly more sensitive than non-actinic inspection. This is especially evident in the case of defects in the centre of the shifted space where the difference in aerial image intensity between with defect and defect free positions is difficult to detect. The sensitivity of non-actinic inspection can be improved by increasing the NA of the inspection system.

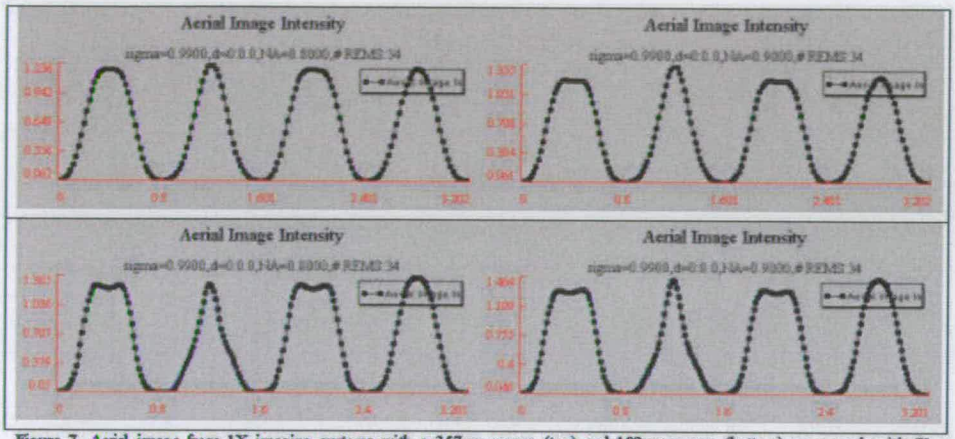

Figure 7. Aerial image from 1X imaging systems with a 257nm source (top) and 193nm source (bottom) on a mask with 70nm line/130nm space and a 150nm defect at the edge of the shifted space. For each wavelength the left-hand plot shows a NA of 0.8 and the right hand a NA of 0.9.

Year	*2001*	*2002*	*2003*	*2004*	*2007*	*2010*	*2013*
TECHNOLOGY NODE	*130nm*			*90nm*	*65nm*	*45nm*	*33nm*
Mask minimum image size	*360*	*320*	*280*	*240*	*180*	*128*	*92*
Defect size	*104*	*92*	*80*	*72*	*52*	*36*	*26*

Table 1. Summary of allowable mask defect size from the ITRS roadmap, 2000 update.

6) CONCLUSIONS

Simulation studies show that smaller defects at the centre of a shifted space than at the edge result in the limits of CD tolerance being reached. In semi-dense patterns the defects have greater effect at best focus than at the edge of the focus window, whereas in more isolated cases the defects have greater effect at defocus. The most sensitive position for a defect is not at the edge or centre of the shifted space but rather at a position between these two. Detection of defects in the centre of a shifted space is significantly more difficult in a non-actinic transmission inspection than in an actinic inspection. For defects at the edge of a shifted space the non-actinic inspection appears to be more likely to detect these features than for a centre defect.

REFERENCES

1. M.D. Levenson, N.S. Visanathan, R.A. Simpson, "Improving resolution in photolithography with a phase-shifting mask", IEEE Transactions on Electron Devices, Vol ED-29, No. 12, pp.1828-1836, 1982.
2. A. Wong, "Rigorous three-dimensional time-domain finite-difference electromagnetic simulation", Ph.D. dissertation, University of California at Berkeley, 1994.
3. C.K. Kalus, S. List, A. Erdmann, R.L. Gordon, M. McCallum, A. Semmler, "Benchmarking of available rigorous electromagnetic field (EMF) simulators for phase-shift masks applications", Microelectronic Engineering, pp.79-86, 2001.
4. T.V. Pistor, A.R. Neureuther, R.J. Socha, "Modeling oblique incidence effects in photomasks", SPIE 4000, pp.228-237, 2000.
5. D. Alles, P. Ter Beek, S.T. Juang, J.N. Wiley, K. Hsai, "Reticle inspection system using DUV wavelength and new alogorithm platform for advanced reticle inspection for 0.13-um technology node", SPIE 4066, pp.462-471, 2000.

Electrical CD Characterisation of Binary and Alternating Aperture Phase Shifting Masks

S. Smith, M. McCallum, A.J. Walton and J.T.M. Stevenson

Abstract—

Many of the recent advances in optical lithography have been driven by the utilisation of complex photomasks using Optical Proximity Correction (OPC) or phase shifting technologies. These masks are difficult and expensive to manufacture so the ability to test and characterise the mask making process is very important. This paper examines the issues involved in the use of relatively low cost Electrical Critical Dimension (ECD) measurement of mask features. Modified cross-bridge test structures have been designed to allow the on-mask measurement of dense and isolated, binary and phase shifted layouts. The results of electrical and Critical Dimension Scanning Electron Microscope (CD-SEM) testing of these structures are presented and indicate the lower variability associated with ECD measurements. In particular the adverse effect of phase shifting elements on the accuracy of SEM measurements is highlighted.

I. INTRODUCTION

Economic considerations mean that optical lithography is the first choice for mass production of Ultra Large-Scale Integrated (ULSI) circuits. As the drive for smaller and smaller feature sizes continues, techniques which allow imaging of features much smaller than the wavelength of the exposure light have become important [1]. These techniques include Optical Proximity Correction (OPC), off axis illumination, pupil filtering and the use of Phase Shifting Masks (PSM) [2].

Masks which utilise OPC and phase shifting techniques are more complex to manufacture than conventional masks and so the ability to test and characterise the mask is very important. Most schemes for mask metrology require either optical testing or, as geometries reduce, measurement with a CD-SEM system. Both of these techniques are expensive in terms of equipment and testing costs. A less expensive option would be to use electrical test structures such as the cross bridge linewidth structure. Binary and phase shift masks have been used to print test structures before [3]. This paper takes the concept a step further by placing test structures on the mask and measuring them in a similar manner to that described in reference [4]. The results from the on-mask test structures can be compared with measurements made on similar structures which will be printed using a different section of the photomask.

S. Smith, A.J. Walton and J.T.M. Stevenson are with the Department of Electronics and Electrical Engineering, Scottish Microelectronics Centre, The University of Edinburgh, Kings Buildings, Edinburgh, EH9 3JF, U.K. (e-mail: Stewart.Smith@ee.ed.ac.uk)

M. McCallum is with Nikon Precision Europe, Nikon Court, Kirkton Campus, Livingston, West Lothian, EH54 7DL

II. TEST STRUCTURES

The standard test structure used to measure the electrical critical dimension of a conducting track is the cross-bridge linewidth structure [5]. The cross bridge structure consists of two different sections. The first is a Greek cross [6] which is a type of van der Pauw, sheet resistance measurement structure [7], [8]. The second part is a bridge resistive structure which is used in conjunction with the value of sheet resistance (R_s) to extract the electrical linewidth [9].

A. Greek Cross Test Structures

The Greek cross is a four-terminal van der Pauw, sheet resistance test structure. It allows the measurement of the sheet resistance (R_S) of a conducting film with a constant thickness and uniform material resistivity. The method of extracting the sheet resistance from such a structure is described in reference [10]. In short, four Kelvin resistance measurements are performed, the results are averaged (R_{avg}) and the sheet resistance is calculated using

$$R_s = \frac{\pi R_{avg}}{\ln 2} \tag{1}$$

This equation can be used when the structure displays 90 degree rotational symmetry [11]. The error introduced by any asymmetry can be reduced by using a correction factor f, as described in references [10] and [11].

B. Bridge Linewidth Structures

Once a value of R_s for the conducting material is known then it can be used to calculate the linewidth of the bridge part of the test structure [5]. The method used to extract the ECD using a cross-bridge structure is described in reference [9]. Firstly the resistance of the bridge section (R_B) is found using a Kelvin measurement then the linewidth can be calculated using

$$W_B = \frac{R_s L_B}{R_B} \tag{2}$$

where L_B is the length of the bridge section.

The accuracy of the linewidth measurement depends mainly on the error introduced by the finite width of the voltage taps at either end of the bridge [4]. They have the effect of widening the line in these regions which makes the bridge seem shorter than it is. This can be minimised by following the design constraint that the bridge length L_B is much greater then the tap width [12].

C. PSM Test Structures

Cross-bridge test structures which were developed to investigate metal damascene interconnect processes have been adapted for use with alternating phase shifting masks. In the "dense" test structures the electrically measured line is surrounded by floating lines and phase shifting regions in a similar way to the AltPSM test sites described in reference [3]. This is illustrated in figure 1.

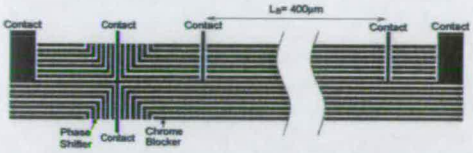

Fig. 1. Section of PSM test structure layout. The black areas are the chrome blockers while the shaded areas are regions of 180° phase shift. This is a structure with a linewidth of 1.5μm and a line to space ratio of 1:1.

The PSM layout contains test structures with on mask linewidths of 0.4, 0.5, 0.6, 0.7, 0.8, 0.9, 1.0, 1.1, 1.2 and 1.5μm. Bridge structures with line to space ratios of 1:1, 1:1.5, 1:2, 1:3, 1:5 and 1:10 were designed for each of the feature sizes. There are two sets of dense structures with different arrangements of the dummy lines around the Greek cross. The first set resemble figure 1, where the floating lines follow the shape of the cross, and these will be referred to as "L-Type" structures. In the second set the unmeasured lines run up to the vertical contact arms of the cross and stop short as they do in the bridge section of the structure. This set will be referred to as "I-Type" test structures. The full layout is a 14 × 10 array of test structures with probe pads which can be probed on-mask using a standard 2×n probe card. This includes two isolated linewidth structures for each feature size. A second layout has also been designed where the probe pads are scaled so that when the structures are printed using a 4× exposure tool the pads will be the same size as those designed for on-mask measurement. Figure 2 shows lines with a CD of 91nm which were printed in photoresist using the 0.4μm features on the photomask.

Fig. 2. SEM image of 91nm wide lines printed using a S202 scanner (0.6NA) and the phase shift mask used in this study.

The layout with the large pads has been repeated three times on the mask, once with the phase shifting elements removed to give binary structures. The version with the small pads for on-mask testing is repeated 24 times on the mask and again 8 of these are binary features. A picture of the mask can be seen in figure 3 along with a closeup of the layout for on-mask probing.

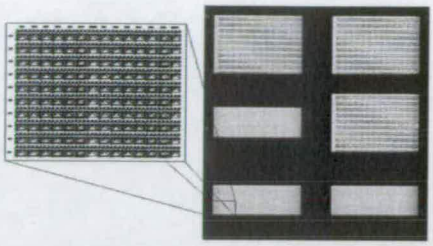

Fig. 3. Photograph of the actual phase shifting mask with a close up view of the layout of one of the sets of on-mask test structures.

III. Sheet Resistance Measurements

The Anti-Reflective (AR) coating of chromium oxide on the mask presents a challenge when electrically probing the devices [13]. Initial attempts to use a standard 2 × 4 probe card designed to probe aluminium pads were unable to make reliable electrical contact because the AR coating was too hard for the probe tips to penetrate. However, it was found that steerable probes on a manual probe station were able to contact the chromium. It should be noted that considerable force was required to make contact but no scratching of the pads was observed. Sheet resistance measurements were made on the Greek cross section of one of the isolated binary 1.5μm structures. The measurements were very noisy partly because the potentials were being measured using Source Monitor Units (SMUs) which did not have a high enough resolution for low voltages. The repeatability was significantly improved by using higher currents as can be seen in figure 4.

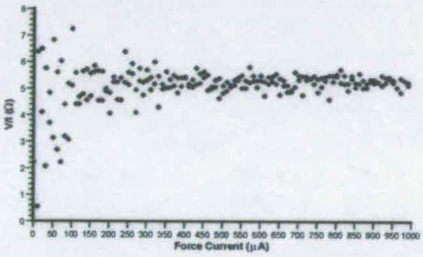

Fig. 4. Results of Kelvin measurements made on a chrome Greek cross structure as the force current was swept from 1μA to 1mA.

One interesting result was that although the repeatability at low currents was quite poor, a large number of measurements at a set force current typically resulted in almost the same mean value. Sets of 200 measurements were made over a short space of time at five force currents ranging from 10μA to 1mA. The mean value of V/I and the standard deviation calculated for each current setting is plotted in figure 5.

The results indicate that although the repeatability of the measurement improves with higher force currents

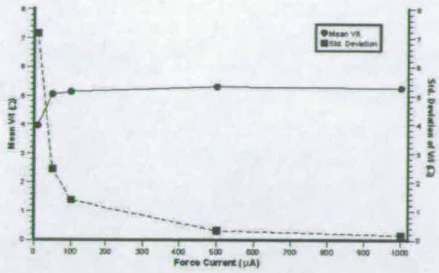

Fig. 5. Mean values and standard deviation of V/I versus force current for a chrome Greek cross structure.

these high currents do not appear to lead to joule heating and a change in resistance. As the repeatability of the measurement is almost the same at 500μA and 1mA it was decided that the lower current should be used for any further measurements as a precaution against damaging the structure under test.

The Greek cross part of the test structure was measured 200 times at four different orientations with a force current of 500μA and the results are presented in table I.

TABLE I

RESULTS OF KELVIN MEASUREMENTS MADE ON A GREEK CROSS TEST STRUCTURE WITH A FORCE CURRENT OF 500μA.

Orientation	Mean V/I (Ω)	$\sigma_{(V/I)}$ (Ω)	R_s (Ω/□)
+0°	5.30249	1.078	24.0328
−0°	5.36345	0.102	24.3091
+90°	5.23089	1.061	23.7083
−90°	5.40126	0.108	24.4804
Average	5.3245	-	24.1326

The measured sheet resistance of $24.13\Omega/\square$ is similar to a reported value of $19.4\Omega/\square$ for chrome without an AR coating [4]. The measurements in table I show a factor of ten difference between the standard deviations measured with forward and reverse currents. The reason for the difference in variability is not clear but it may be related to probe contact problems. However, it does seem that contact resistance significantly affects the measurement as the values of mean V/I obtained are lower for the orientations with a larger standard deviation.

The chromium oxide coating was removed by a very short etch in an aqueous solution of ceric ammonium nitrate and acetic acid. This meant that a test system using a probe card and semi-automatic probe station could then be used. This system uses a voltmeter with a higher resolution which providing more repeatable and precise measurements. However, isolated 1.5μm structures from one of the binary and one of the phase shifted layouts were tested first using the manual probe station to obtain further information about the effect of the measurement current on the results. Figure 6 shows the mean sheet resistance plotted against the force current while figure 7 shows the standard deviation.

There are a number of conclusions that can be drawn

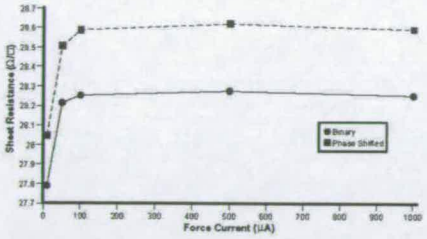

Fig. 6. Mean values of R_s against force current for chrome Greek cross structures.

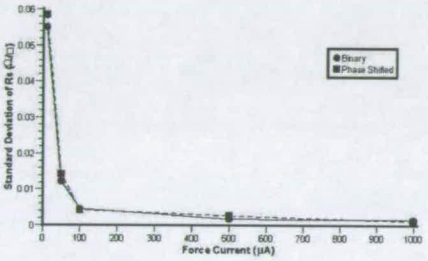

Fig. 7. Standard deviation of R_s against force current for chrome Greek cross structures.

from these results. Firstly the shapes of the curves are very similar to those in figure 5 indicating that a force current of 500μA could again be used to obtain repeatable results. However, the values of standard deviation are significantly lower than the previous results which suggests that most of the variability of the measurements made on the unetched structures was probably due to noise introduced by poor probe contacts. Secondly there is an offset of $0.344\Omega/\square$ (roughly 1.2%) between the average sheet resistances from the phase shifted and binary structures when measured with a current of 500μA. This may have been due to variation of the sheet resistance across the mask plate. The sheet resistances measured after the chromium oxide was removed were typically $4\Omega/\square$ higher than before which indicates there was some overetching of the chrome features.

Next, one complete set of structures (see figure 3) from the binary section and one from the phase shifted region were measured using the higher resolution system and the semi-automatic probe station. The sheet resistance measurements have been averaged together for each feature size (figure 8) and the standard deviation calculated (figure 9) to give some measure of the variation with pitch.

From figure 8 it can be seen that sheet resistance increases monotonically for designed feature sizes above 0.7μm. Similarly the variation of the sheet resistance decreases as the linewidth increases. The most interesting results are observed for the narrow, phase shifted, L-type structures. The mean sheet resistance increases as the feature size decreases as does the variation of R_s with

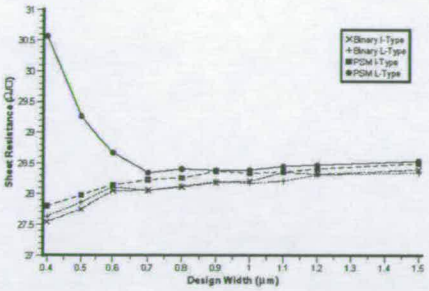

Fig. 8. Mean values of R_s against feature size for chrome Greek cross structures.

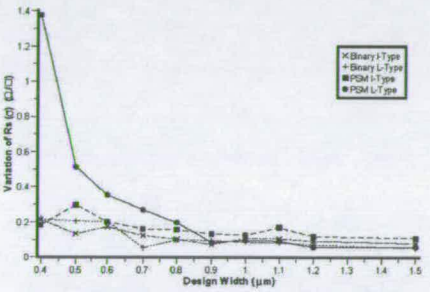

Fig. 9. Standard deviation of R_s against feature size for chrome Greek cross structures.

pitch. It is only on the L-type structures (see figure 1) that the phase shifting elements can significantly affect the extracted value of sheet resistance.

Figure 10 shows the average asymmetry factor F_A [10] plotted against the feature size. Provided F_A is less than 0.1, the correction factor f is insignificant and the sheet resistance can be calculated using equation (1). It is clear from figure 10 that there is no significant asymmetry in the binary and I-type phase shifted structures except for those with the smallest features. Even then the largest correction required to the value of R_S is only about 0.3%. The phase shifted L-type structures, however, show significant and systematic asymmetry. The maximum value of F_A is observed for the 0.4μm crosses and would require a 2.2% correction to the extracted sheet resistance. However, this effect cannot account for the high values of R_S measured with these structures. It is possible that the effect of etching the phase shifting elements on the geometry of these Greek crosses leads to current crowding and joule heating during measurement.

IV. Electrical Linewidth Measurements

Initial measurements of the resistance of a nominal 1.5μm wide track were performed using the manual probing system before the oxide was removed and the results are presented in table II.

It should be noticed that the standard deviations ob-

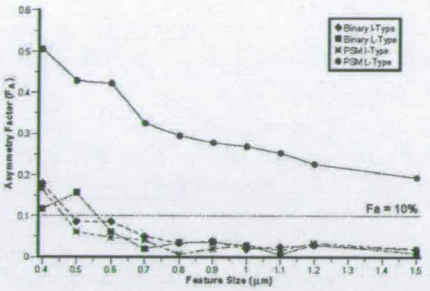

Fig. 10. Average Greek cross asymmetry factor F_A versus feature size for chrome structures.

TABLE II

Results of Kelvin measurements made on a bridge linewidth structure with a force current of 500μA.

Force Direction	Mean Resistance (Ω)	σ_R (Ω)
Forward	6730.22	2.4537
Reverse	6729.34	2.2709
Average	6729.78	-

served when making the bridge measurements are proportionately much smaller ($\approx$ 0.035%) than for the R_s measurements where σ was almost 20% for some measurements. This is probably because the voltages being measured are much higher for the bridge structures than for the crosses. Taking the average bridge resistance from table II and using it in equation (2) along with the average sheet resistance from table I gives an electrical linewidth (W_L) of 1.434μ m. The nominal value of linewidth was 1.5μm so the electrical width is about 4.4% less than this. If the individual values of R_s from each measurement orientation are used to calculate linewidth figures using the average bridge resistance it can be seen that the measurements which showed the best repeatability provide values of ECD closest to the nominal linewidth. The linewidth results and the standard deviations of the sheet resistances can be seen in table III.

TABLE III

Sheet resistance, standard deviation of R_s and linewidths for each Greek cross measurement orientation.

Orientation	Mean R_s (Ω/□)	σ_{R_s} (Ω/□)	W_L (μm)
+0°	24.0328	4.886	1.428
−0°	24.3091	0.462	1.445
+90°	23.7083	4.809	1.409
−90°	24.4804	0.489	1.455

There are two main sources for variability in electrical CD measurements, firstly the measurement of the resistance of the bridge itself and secondly the value of sheet resistance used in the linewidth calculation. The first can be minimised through the choice of measurement current and, as is clear from the results in table II, makes up a very small proportion of the measured resistance. The sheet resistance variability is more of a problem. The results presented in figures 8 and 9 indicate that the value

of R_S extracted from the structures and the variability of the measurement with pitch is a function of feature size. This is particularly clear for the measurements made on phase shifted L-type crosses. For this reason it was decided that the average of the sheet resistances extracted from the 1.5μm structures should be used. The values are 28.5$\Omega/\square$ for the phase shifted structures and 28.4$\Omega/\square$ for the binary structures.

CD-SEM measurement of these structures has also been performed and figure 11 shows the electrical and SEM measurement results for the L-type, isolated structures.

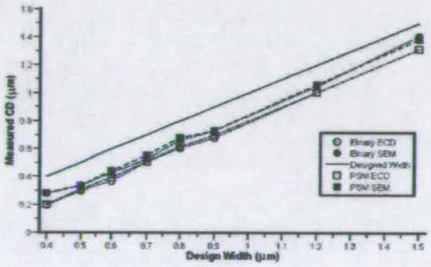

Fig. 11. Measured linewidth versus the designed CD for isolated bridge structures.

It is clear from these results that there is an offset between the electrical and SEM measurements. This is to expected as systematic differences of a similar size are common between electrical linewidth measurements and other CD metrology techniques [14], [15]. Plotting the data in this way makes it difficult to visualise the offset because of the large range of widths. Figure 12 shows the results of subtracting each of the measured widths from the drawn width.

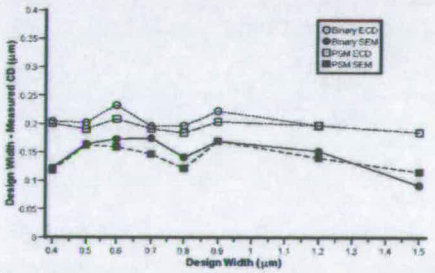

Fig. 12. Designed linewidth minus the measured CD plotted against the designed width for isolated bridge structures.

This identifies the offset between the electrical and SEM measurements which varies from a maximum of ~0.08μm down to a minimum of ~0.02μm. However, there is no obvious trend with feature size. The same operation has been performed with the CD measurements of the dense linewidth structures with a mark to space ratio of 1:2 and the results are presented in figure 13.

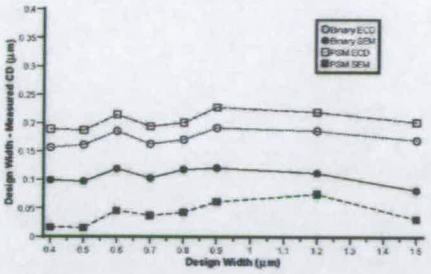

Fig. 13. Designed linewidth minus the measured CD plotted against the designed width for 1:2 dense bridge structures.

The most important point to notice here is the offset between the electrical and SEM results for the phase shifted structure which is about twice that observed for the binary structures. For CD-SEM linewidth measurement the threshold selected to define the edge of the feature has a systematic effect on the extracted width. It is possible that the presence of the alternating phase shifting elements affect the SEM image so that the tracks appear significantly wider than expected. Unfortunately no SEM images are available of the phase shifted structures but figure 14 shows a typical image obtained from the binary section of the mask. Charging of the mask in the SEM chamber meant that the images obtained had poor contrast which is undesirable when attempting to make accurate CD measurements.

Fig. 14. SEM image of a nominally 0.7μm wide binary feature.

The results presented in figures 12 and 13 suggest that the difference between the measured and designed width is not a function of the linewidth. However, if the dense structure results are plotted as a function of the mark to space ratio for a certain linewidth it becomes clear that there is a significant proximity effect on the width of the bridge resistor. Figure 15 shows the electrical and SEM CD results for dense 0.4μm structures.

The difference between the designed and measured widths increases as the mark to space ratio becomes smaller. This means that the measured width of the line decreases as the spacing between it and the surrounding dummy tracks increases.

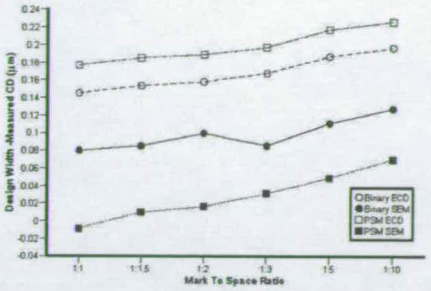

Fig. 15. Designed linewidth minus the measured CD plotted against mark to space ratio for 0.4μm dense bridge structures.

V. Conclusions

The preliminary measurements indicated that it is possible to probe test structures on chrome masks with anti-reflective coatings. However, suspected probe related problems make the measurements less repeatable than when probing the etched chrome pads.

The measurements made on Greek cross structures show that the variability of the extracted sheet resistance is reduced by increasing the size of the cross, as in reference [16]. Future on-mask test structure layouts should use very large Greek crosses, or possibly box crosses, for R_S extraction rather than following the minimum feature size of the bridge section.

It is clear that the etching of the phase shifting elements has a strong effect on the geometry of the L-type cross structures. This leads to large errors in the very narrow crosses which cannot be removed through the use of the correction factor f. Further work will include the use of an Atomic Force Microscope (AFM) to investigate these structures in an attempt to fully explain these results.

The electrical linewidth measurements show that the tracks are significantly narrower than the designed width and this may be partly due to the etching process used to remove the anti-reflective coating. There is also a systematic offset between binary and phase shifted dense tracks. Finally there is a proximity effect caused by the dummy tracks in the dense structures which makes the closely packed lines wider than those that are more generously spaced.

Differences have been demonstrated between CD-SEM and electrical measurements with the electrical results being more repeatable. As expected there is a systematic offset between the electrical and SEM results obtained from the binary structures. What was unexpected was that the phase shifted lines, which appeared to be electrically narrower than the binary structures, were measured on the CD-SEM system as being significantly wider. This may be due to the phase shifters causing confusion about the position of the line edge.

Future work will include AFM scans of these structures which should help identify the reasons for the differences between the electrical and SEM measurements. The mask will be used to print test structures which will also be measured electrically. These results will be compared with on-mask measurements to obtain information about the mask error factor (MEF).

Acknowledgements

The authors would like to acknowledge the support of EPSRC (GR/L81000), Nikon and International SEMATECH. We would also like to thank Paul Harris and Alan Lissimore of Nikon for their help with printing and metrology.

References

[1] T. Terasawa, "Subwavelength lithography (PSM,OPC)," in *Design Automation Conference 2000*, 2000, pp. 295–300.

[2] B. J. Lin, "Phase-shifting masks gain an edge," *IEEE Circuits and Devices Magazine*, vol. 9, pp. 28–35, March 1993.

[3] B. J. Lin, D. J. Samuels, and C. A. Spence, "Single-level electrical testsites for phase-shifting masks," in *Integrated Circuit Metrology, Inspection and Process Control VI*, 1992, vol. 1673, pp. 221–228.

[4] M.W. Cresswell, M. Gaitan, R.A. Allen, and L.W. Linholm, "A Modified Sliding Wire Potentiometer Test Structure for Mapping Nanometer-Level Distances," in *Proceedings of IEEE International Conference on Microelectronic Test Structures*, Kyoto, Japan, March 1991, pp. 129–134.

[5] M.G. Buehler, S.D. Grant, and W.R. Thurber, "Bridge and van der Pauw Sheet Resistors For Characterizing the Line Width of Conducting Layers," *J. Electrochemical Soc - Solid State Technology*, vol. 125, no. 4, pp. 650–654, April 1978.

[6] W. Versnel, "Analysis of the Greek cross, a Van der Pauw Structure with Finite Contacts," *Solid State Electronics*, vol. 22, no. 11, pp. 911–914, 1979.

[7] L.J. van der Pauw, "A Method of Measuring Specific Resistivity and Hall Effects of Discs with Arbitrary Shape," *Phillips Research Rep.*, vol. 13, pp. 1–9., Jan 1958.

[8] L.J. van der Pauw, "A Method of Measuring the Resistivity and Hall Coefficient on Lamellae of Arbitrary Shape," *Philips Technical Review*, vol. 59, no. 8, pp. 220–224, 1958.

[9] "Standard Test Method for Determining the Average Electrical Width of a Straight Thin-Film Metal Line [Metric]," Tech. Rep. F1216M-96, American Society for Testing and Materials, 1996.

[10] M.G. Buehler and W.R. Thurber, "An Experimental Study of Various Cross Sheet Resistor Test Structures," *J. Electrochemical Soc - Solid State Technology*, vol. 125, no. 4, pp. 645–650, April 1978.

[11] S. Smith, A.J. Walton, and M. Fallon, "Investigation of Optical Proximity Correction (OPC) and Non-Uniformities on the Performance of Resistivity and Linewidth Measurements," in *Proceedings of IEEE International Conference on Microelectronic Test Structures*, Goteborg, Sweden, March 1999, pp. 161–166.

[12] G.P. Carver, R.L. Mattis, and M.G. Buehler, "Design Considerations for the Cross-Bridge Sheet Resistor," Tech. Rep. NBSIR 82-2548, National Bureau of Standards, Washington, DC, 1982.

[13] M.W. Cresswell, ," Private communication.

[14] R.A. Allen, P. Troccolo, J.C. Owen, J.E. Potzick, and L.W. Linholm, "Comparisons of measured linewidths of submicrometer lines using optical, electrical, and SEM metrologies," *Proceedings of the SPIE*, vol. 1926, pp. 34–43, 1993.

[15] L.W. Linholm, R.A. Allen, M.W. Cresswell, R.N. Ghoshtagore, S. Mayo, H.A. Schafft, J.A. Kramar, and E.C. Teague, "Measurement of Patterned Film Linewidth for Interconnect Characterization," in *Proceedings of IEEE International Conference on Microelectronic Test Structures*, Nara, Japan, March 1995, pp. 23–26.

[16] M.I. Newsam, A.J. Walton, and M. Fallon, "Numerical Analysis of the Effect of Geometry on the Performance of the Greek Cross Structure," in *Proceedings of IEEE International Conference on Microelectronic Test Structures*, Trento, Italy, March 1996, pp. 247–252.

Electrical Dimension Characterisation of Binary and Alternating Aperture Phase-Shifting Masks

Martin McCallum, Stewart Smith[†], Alan Lissimore,

Anthony J.Walton[†] and J.Tom M. Stevenson[†]

Nikon Precision Europe GmbH, Nikon Court, Kirkton Campus, Livingston EH54 7DL, UK

[†]School of Engineering and Electronics, SMC, University of Edinburgh, King's Buildings, Edinburgh EH9 3JF, UK

ABSTRACT

This paper presents the use of specially designed electrically testable structures to measure and characterise linewidths on both binary and alternating aperture phase-shifting masks (altPSM). The technique behind the use of these modified cross-bridge structures is explained together with the specific designs used to characterise both dense and isolated features. The practicality of measuring masks with and without anti-reflective chromium dioxide are discussed and the the difference in the repeatability of the measurements is presented. CD SEM measurements of these features are compared with those obtained electrically and an excellent correlation between the electrical dimension (ECD) and the dimension measured both on mask and wafer by SEM is shown.

1) INTRODUCTION

In lithography today we are rapidly developing new exposure tool systems that are using lower and lower wavelengths of light to print the features that are required by today's advanced IC devices. However, reducing the wavelength by itself is not enough and so to help in the drive to smaller geometries we are also utilising other methods that involve very complicated photomasks using techniques such as Optical Proximity Correction (OPC) and phase-shifting. These photomasks obviously also require very small features to be clearly patterned and are consequently difficult and expensive to manufacture. Hence, an accurate and robust capability to test and characterise the mask making process is very important. However, as device manufacturers know, small dimensions are not easy to accurately measure using conventional optical measurement tools. As a result tools such as SEMs are employed to achieve the resolution and accuracy required. These tools are prohibitively expensive and also come with technical problems. One of the major issues with mask metrology is our wish to measure conductive features on an insulating base. This situation is bearable on silicon but exceedingly difficult to deal with on photomasks. This paper examines the issues involved in the use of relatively low cost Electrical Critical Dimension (ECD) measurement of mask features. This technique has the twin advantages that it requires relatively low cost equipment and actually requires a patterned conductor on an insulator.

2) METHOD

To electrically test dimensions we chose to utilise a crossbridge linewidth structure [1] on a 4× mask for use on a Nikon step and scan DUV system. The crossbridge structure consists of two different sections. The first is a Greek cross [2] which is a type of van der Pauw, sheet resistance (R_s) measurement structure [3,4]. The second part is a bridge structure which is used, in conjunction with the value of sheet resistance obtained from the Greek cross, to extract the electrical linewidth [5].

Cross-bridge test structures, which were originally designed to investigate metal damascene interconnect processes [6], were used as the basis for the on mask patterns. These could be used directly for the binary patterns but some adaptation was required for the altPSM patterns. In the "dense" test structures the electrically measured line is surrounded by floating lines and phase shifting regionsand is illustrated in Figure 1 [7].

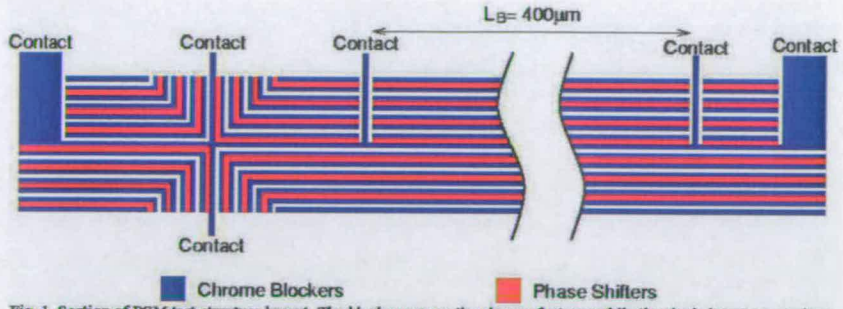

Fig. 1. Section of PSM test structure layout. The black areas are the chrome features while the shaded areas are regions of 180° phase shift. This is a structure with a linewidth of 1.5µm and a line to space ratio of 1:1.

The test structure layout contains test structures with on mask linewidths of 0.4, 0.5, 0.6, 0.7, 0.8, 0.9, 1.0, 1.1, 1.2 and 1.5µm. Bridge structures with line to space ratios of 1:1, 1:1.5, 1:2, 1:3, 1:5 and 1:10 were designed for each of the feature sizes. There are two sets of dense structures with different arrangements of the dummy lines around the Greek cross. In the first set the floating lines follow the shape of the cross, and these will be referred to as "L-Type" structures. In the second set the unmeasured lines run up to the vertical contact arms of the cross and stop short as they do in the bridge section of the structure. This set will be referred to as "I-Type" test structures. Both of these types are shown in figure 2.

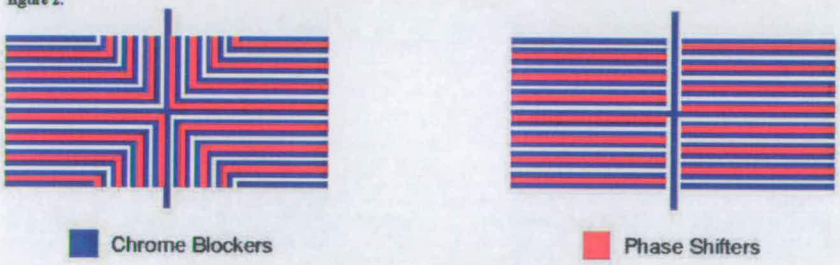

Fig. 2. Layout of the L-type (left) and I-type (right) Greek cross structures.

The module layout is a 14 × 10 array of test structures with probe pads which can be probed using a standard 2 × n probe card. This includes two isolated linewidth structures for each feature size. Two modules were produced: one with pads sized for on-mask probing and one where the probe pads are scaled so that when the structures are printed using a 4× exposure tool the pads will be the same size as those designed for on-mask measurement. The layout with the large pads has been repeated three times on the mask, once with the phase shifting elements removed to give binary structures. The version with the small pads for on-mask testing is repeated twenty four times, in three blocks of eight, where one set contains binary structures. A picture of the mask can be seen in figure 3 along with a close-up of the layout for on-mask probing.

The chrome layer on the mask was written on a variable shaped e-beam tool. The phase-shifting layer on a laser based optical tool. Phase etch was performed using an ICP etch tool. The phase-shifting layer was designed with an overlap of 200nm over the chrome features.

The SEM used to measure the mask was a modified Hitachi S-7080. The wafers were measured on a Hitachi S-8840 SEM. Electrical measurements from both automated and manual probe stations were measured using an HP-4145B, HP 4062B and Solatron microvoltmeter.

The wafer exposures were performed using a Nikon S-204B step and scan tool with an NA of 0.68 and partial coherence of 0.4. The wafers were coated in 400nmm of Shipley UV210 resist and developed in 0.26N developer on a DNS 200B track interfaced to the exposure tool.

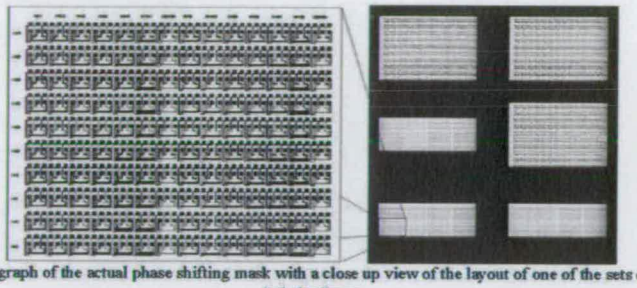

Fig. 3. Photograph of the actual phase shifting mask with a close up view of the layout of one of the sets of on-mask test structures.

3) RESULTS

3.1) Sheet resistance Measurement

The Anti-Reflective (AR) coating of chromium oxide on the mask presents a challenge when electrically probing the devices [8]. Initial attempts to use a standard 2 × 4 probe card designed to probe aluminium pads was unable to make reliable electrical contact because the AR coating was too hard for the probe tips to penetrate. However, it was found that steerable probes on a manual probe station were able to pierce the AR coating and contact the underlying chromium. It should be noted that considerable force was required to make contact but no scratching of the pads was observed. Sheet resistance measurements were made on the Greek cross section of one of the isolated binary 1.5µm structures. The measurements were very noisy partly because the potentials were being measured using Source Monitor Units (SMUs) which did not have a high enough resolution for low voltages. The repeatability was significantly improved by using higher currents as can be seen in Fig. 4.

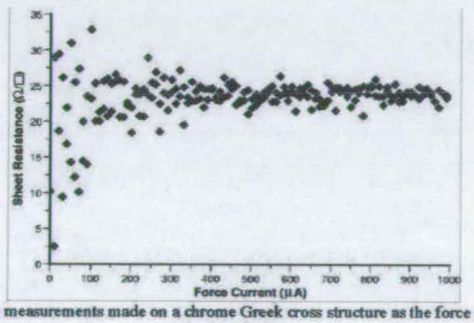

Fig. 4. Results of Kelvin measurements made on a chrome Greek cross structure as the force current was swept from 1µA to 1mA.

One interesting result was that although the repeatability at low currents was quite poor, a large number of measurements at a set force current typically resulted in almost the same mean value. Sets of 200 measurements were made over a short space of time at five force currents ranging from 10μA to 1mA. The mean values and standard deviations of sheet resistance calculated for each current setting are plotted in figure 5.

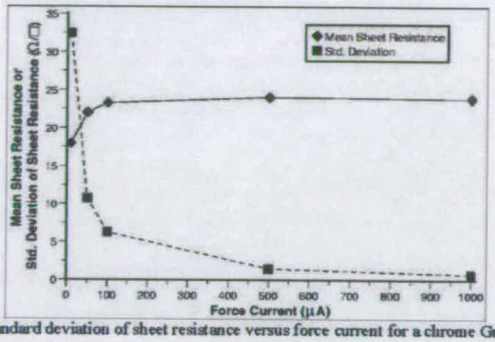

Fig. 5. Mean and standard deviation of sheet resistance versus force current for a chrome Greek cross structure.

The results indicate that although the repeatability of the measurement improves with higher force currents these high currents do not appear to lead to joule heating and a change in resistance. As the repeatability of the measurement is almost the same at 500μA and 1mA it was decided that the lower current should be used in any further measurements as a precaution against damaging the structure under test. The measured sheet resistance of 24.13Ω/□ is similar to a reported value of 19.4Ω/□ for chrome without an AR coating [8].

The chromium oxide AR coating was then removed by a very short etch in an aqueous solution of ceric ammonium nitrate and acetic acid. This meant that a test system using a probe card and semi-automatic probe station could then be used. This system uses a voltmeter with a higher resolution which provided more repeatable and precise measurements.

Next, one complete set of structures (see figure 3) from the binary section and one from the phase shifted region were measured using the higher resolution system and the semi-automatic probe station. The sheet resistance results obtained from the dense I and L-type test structures have been averaged together for each feature size and are presented in figure 6.

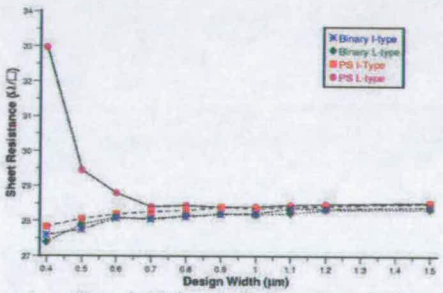

Fig. 6. Mean values of R_S against feature size for dense chrome Greek cross structures.

Ideally sheet resistance (R_s) should be insensitive to feature size and the variation for structures with a nominal width of more than 0.7µm is small. For example, the difference between the mean sheet resistance extracted from the phase shifted I-type structures with a cross arm width of 0.7µm and those that are 1.5µm wide is ~0.25Ω/□ which is less than 1%. The narrower structures show much more variation with size, in particular the sheet resistances extracted from the phase shifted L-type structures show a sharp increase as dimensions reduce. At present the reason for this is not clear but it is only in the L-type structures that the phase shifting elements surround the centre of the Greek cross as can be seen in figure 1. The fabrication of the phase shifters may be affecting the geometry of the cross leading to problems with the measurements. Figure 7 shows the average asymmetry factor F_A plotted against feature size. F_A is a figure representing the difference between measurements made on a cross structure at different orientations and is used to calculate a correction factor which is applied to the calculated sheet resistance to correct for asymmetry [9].

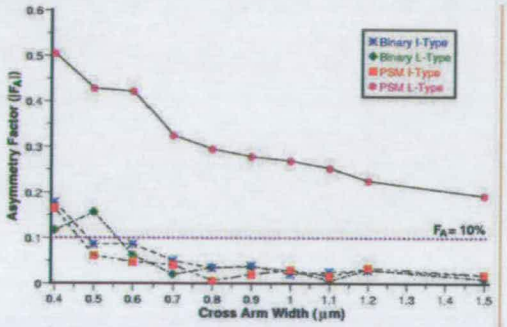

Fig. 7. Average Greek cross asymmetry factor $|F_A|$ versus feature size for chrome structures.

Provided that F_A <10.74% the correction factor approaches unity and does not need to be used. Figure 7 shows that F_A is negligible for binary and I-type phase shifted cross structures with cross arms wider than 0.7µm. Even the narrowest of these structures only requires correction of about 0.3% to the value of R_S. The results from the L-Type phase shifted structures confirm that these structures are not symmetrical and that correction factors should be applied. The sheet resistance results for these structures that are plotted in figure 8 have been corrected according to the method described in reference [10] and this has been effective for the structures wider than 0.7µm. However, asymmetry correction cannot account for the high values of sheet resistance encountered in the narrower crosses. The effect of the phase shifting elements on these structures may have led to current crowding and joule heating in the narrow tracks during measurement. Alternatively these structures may no longer have the correct geometry to be considered as van der Pauw structures and in this case the results should be disregarded.

In addition to the extraction of mean sheet resistance for all the structures with the same nominal feature size, as shown in figure 6, it is possible to investigate the variability of the measurements across the range of different mark to space ratios by taking the standard deviation. The results of these calculations are presented in figure 8.

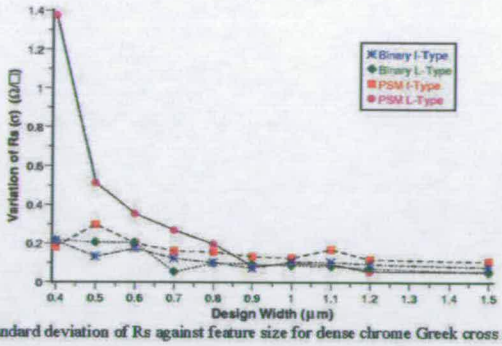

Fig. 8. Standard deviation of Rs against feature size for dense chrome Greek cross structures.

It would be expected that the variation of the sheet resistance between different structures of the same size would reduce as the cross arm width is increased. Reference [11] shows that larger Greek cross structures are less sensitive to short range non-uniformity in the resistivity of the conducting film being measured. Large structures effectively extract the average sheet resistance for the material.

3.2) Linewidth measurements

Initial measurements of the resistance of a nominal 1.5μm wide track were performed using the manual probing system before the chromium oxide was removed and the results are presented in table II.

TABLE II. Results of Kelvin measurements made on a bridge linewidth structure with a force current of 500μA.

Force Direction	Mean Resistance (Ω)	σ_R (Ω)
Forward	6730.22	2.4537
Reverse	6729.34	2.2709
Average	6729.78	-

The standard deviations observed when making the bridge measurements are proportionally much smaller (~0.035%) than for the Rs measurements where σ was almost 20% in some cases. This is probably because the voltages being measured are much higher for the bridge structures than for the crosses. The electrical linewidth W_L is calculated by taking the average bridge resistance R_B from table II and using it in:

$$W_L = \frac{R_S L_B}{R_B}$$

where L_B is the length of the bridge section and R_S is the average sheet resistance from table I. The result of this calculation is that W_L = 1.434μm and the nominal value of linewidth was 1.5μm so the electrical width is about 4.4% less than this. If the individual values of R_S from each orientation are used to calculate linewidth figures using the average bridge resistance it can be seen that the measurements which showed the best repeatability provide values of ECD closest to the nominal linewidth. The linewidth results and the standard deviations of the sheet resistances can be seen in table III.

There are two main sources for variability in ECD measurements, firstly the measurement of the resistance of the bridge itself and secondly the value of sheet resistance used in the linewidth calculation. The first can be minimised through the choice of measurement current and, as is clear from the results in table II, makes up a very small proportion of the measured resistance. The sheet resistance variability is more of a problem. It was shown in section 3.1 that the value of R_S extracted from the cross structures was a function of the feature size and it was also found that the

repeatability of the measurements improved as the nominal cross arm width was increased. For this reason it was decided that the average of the sheet resistances extracted from the 1.5μm structures should be used in the calculation of ECD. These values are 28.5Ω/□ for the phase shifted structures and 28.4Ω/□ for the binary structures.

TABLE III. Sheet resistance, standard deviation of R_S and linewidths for each Greek cross measurement orientation.

Orientation	Mean R_S (Ω/□)	σR_S (Ω/□)	W_L(μm)
+0°	24.0328	4.886	1.428
-0°	24.3091	0.462	1.445
+90°	23.7083	4.809	1.409
-90°	24.4804	0.489	1.455

To assess the capability of the electrical measurements against a more standard methodology, the mask was measured on a CD SEM. It was noticed during this measurement that care must be taken to ensure that structures being measured, especially during repeated measurement, do not build up a charge. With an isolated feature on an insulator such as this charge up is rapid and undoubtedly influences accuracy. The altPSM mask showed considerably more charging than the binary mask, probably due to the exposed chrome where the CrO_2 ARC was removed by the phase well etch.

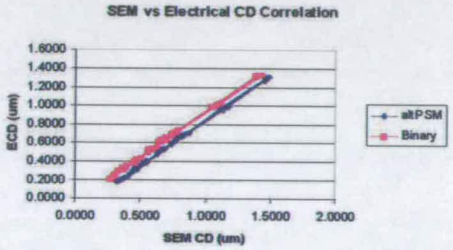

Fig. 9. Comparison of SEM CD (left) and ECD (right) for the binary and altPSM patterns.

The correlation of electrical to SEM measured linewidths is show in figure 9. The correlation for both binary and altPSM features can be seen to be very good. Analysis of this correlation gave an R^2 fit of 0.999 for both binary and altPSM, the covariance of these were 0.112 and 0.118 respectively, indicating that the spread of the fit was small.

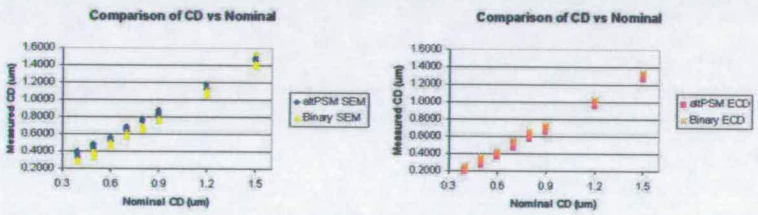

Fig. 10. Comparison of SEM CD (left) and ECD (right) to drawn linewidth for the binary and altPSM mask patterns.

It can be seen from figure 9 that there is an offset between the electrical and measured CDs. In this case the offset for the binary patterns was 63nm whereas for the altPSM it was 165nm, a difference of 82nm. The reason for this difference is not clear as the chrome layer for both binary and altPSM were written on the same tool at the same time.

One possibility is that this could be related to SEM metrology. If we examine the actual CDs we can see an average difference between binary and altPSM patterns of 16nm in ECD and 66nm in SEM measuremens. For binary structures the average CD from the SEM is considerably smaller than for altPSM suggesting the source to be SEM metrology of altPSM structures. The results for SEM and ECD measurements are shown in figure 10.

Analysis of the data by nominal dimension is shown in figure 11 for both binary and altPSM patterns. Good linearity can be seen for all mask dimensions from 1.5μm to 0.4μm. A very good result for linearity through all duty cycles was also achieved as can be seen in figure 12.

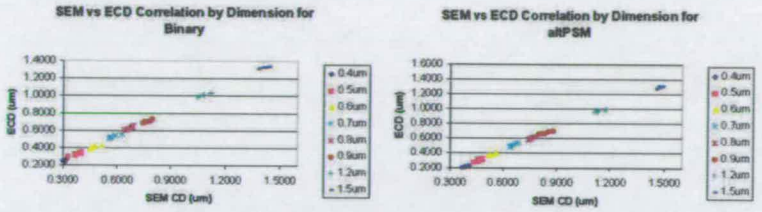

Fig. 11. Comparison of SEM and ECD, grouped by nominal dimension, for the binary (left) and altPSM (right) patterns.

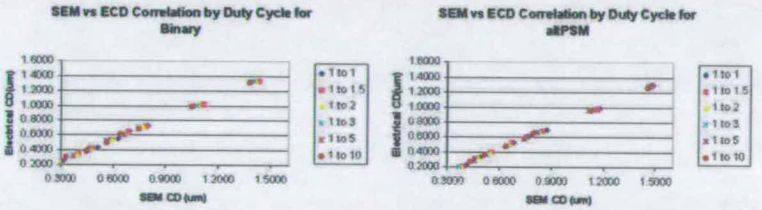

Fig. 12. Comparison of SEM and ECD, grouped by duty cycle, for the binary (left) and altPSM (right) patterns.

Some initial wafer exposures were made and dimensions measured on a CD SEM compared to the mask SEM and ECD measurements for the altPSM patterns. Figure 13 shows the relationship. Analysis of this data gives a correlation of 0.995 for both wafer to mask SEM and for wafer to mask ECD.

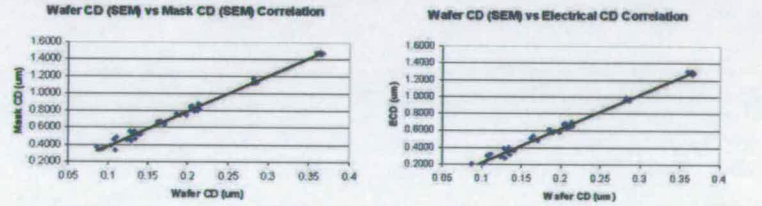

Fig. 13. Wafer CD SEM measurement vs Mask SEM measurement (left) and mask ECD measurement for the altPSM patterns.

4) CONCLUSIONS

The initial measurements indicate that it is possible to probe test structures on chrome masks with anti-reflective coatings. However, it is suspected that probe related problems make the measurements less repeatable than when probing directly onto chrome pads where the AR coating has been removed.

Measurements made on Greek cross structures show that the variability of the extracted sheet resistance is reduced by increasing the size of the cross. It is clear that the etching of the phase shifting elements has a strong effect on the geometry of the L-type cross structures and this leads to large errors in the very narrow crosses which cannot be removed through the use of the correction factor F_A. Future on-mask test structure layouts should use large Greek crosses, or possibly box crosses, for R_S extraction rather than following the minimum feature size of the bridge section. In addition these should be isolated structures as there is no need to use phase shifting elements (which can affect the geometry of the cross) as relatively large features are being printed.

An excellent correlation was made between mask CD SEM measurements and mask ECD measurements for both binary and altPSM patterns. Differences have been demonstrated between CD-SEM and electrical measurements. As expected there is a systematic offset between the ECD and SEM results obtained from the binary structures. What was unexpected was that the phase shifted lines, which appeared to be electrically narrower than the binary structures, were measured on the CD-SEM system as being significantly wider. As both patterns were written on the same tool at the same time and the flourine based etch used to create the phase well does not significantly etch chrome, it is thought that this offset probably originated in the mask CD SEM measurement. In SEM linewidth measurement the threshold selected to define the edge of the feature has a systematic effect on the extracted width. It is likely that the presence of the phase well affects the SEM image so that the tracks appear significantly wider than expected. Charging of the mask in the SEM chamber also affects the measurement of linewidth leading to poor contrast and long testing times. A significant challenge remains in establishing if test structures can be relied upon to give sufficient accuracy while the anti-reflective insulation chromium dioxide remains on the mask. For manufacture and use in altPSM masks though avenues may exist where this can be overcome through judicious use of the patterns used to form and then etch the phase well.

ACKNOWLEDGEMENTS

The authors would like to acknowledge the support of EPSRC (GR/L81000), Nikon and International SEMATECH. We would also like to thank Paul Harris of Nikon for his help with printing and metrology.

REFERENCES

[1] M.G. Buehler, S.D. Grant, and W.R. Thurber, "Bridge and van der Pauw Sheet Resistors For Characterizing the Line Width of Conducting Layers," J. Electrochemical Soc - Solid State Technology, vol. 125, no. 4, pp. 650-654, April 1978.

[2] J.M. David and M.G. Buehler, "A Numerical Analysis of Various Cross Sheet Resistor Test Structures," Solid-State Electronics, vol. 20, pp. 539-543, 1977.

[3] L.J. van der Pauw, "A Method of Measuring Specific Resistivity and Hall Effects of Discs with Arbitrary Shape," Phillips Research Rep., vol. 13, pp. 1-9., Jan 1958.

[4] L.J. van der Pauw, "A Method of Measuring the Resistivity and Hall Coefficient on Lamellae of Arbitrary Shape," Philips Technical Review, vol. 59, no. 8, pp. 220-224, 1958.

[5] "Standard Test Method for Determining the Average Electrical Width of a Straight Thin-Film Metal Line [Metric]." Tech. Rep. F1216M-96, American Society for Testing and Materials, 1996.

[6] C.M. Peyne, A. O'Hara, J.T.M. Stevenson, J.P. Elliott, A.J. Walton, and M. Fallon, "Test Structures for Characterising a Damascene Interconnect Process," in Proceedings of IEEE International Conference on Microelectronic Test Structures, Monterey, CA, USA, March 1997, pp. 151-155.

[7] M. McCallum, S. Smith, A.J. Walton, J.T.M. Stevenson, "Electrical CD characterisation of binary and alternating phase shift masks", Proceedings of IEEE International Conference on Microelectronic Test Structures, Cork, April 2002, pp 7-12.

[8] M.W. Cresswell, ," Private communication.

[9] M.W. Cresswell, M. Gaitan, R.A. Allen, and L.W. Linholm, "A Modified Sliding Wire Potentiometer Test Structure for Mapping Nanometer-Level Distances," in Proceedings of IEEE International Conference on Microelectronic Test Structures, Kyoto, Japan, March 1991, pp. 129-134.

[10] M.G. Buehler and W.R. Thurber, "An Experimental Study of Various Cross Sheet Resistor Test Structures," J. Electrochemical Soc - Solid State Technology, vol. 125, no. 4, pp. 645-650, April 1978.

[11] M.I. Newsam, A.J. Walton, and M. Fallon, "Numerical Analysis of the Effect of Geometry on the Performance of the Greek Cross Structure," Proceedings of IEEE International Conference on Microelectronic Test Structures, Trento, Italy, March 1996, pp. 247-252.

Test Structures for CD and Overlay Metrology on Alternating Aperture Phase-Shifting Masks

S. Smith, M. McCallum†, A.J. Walton, J.T.M. Stevenson,
P.D. Harris†, A.W.S. Ross, A.C. Hourd‡and L. Jiang

School of Engineering and Electronics, Scottish Microelectronics Centre, The University of Edinburgh, Kings Buildings, Edinburgh, EH9 3JF, U.K. Email: Stewart.Smith@ee.ed.ac.uk

†Nikon Precision Europe, Nikon Court, Kirkton Campus, Livingston, West Lothian, EH54 7DL, U.K.

‡Compugraphics International Ltd., Eastfield Industrial Estate, Glenrothes, Fife, KY7 4NT, UK

Abstract— **The ability to test and characterise advanced photomasks for verification and process control is increasingly important and this paper builds on previous work in this area which left a number of unanswered questions. Atomic force and scanning electron microscope measurements are used to explain anomalies in previously presented electrical test results. In addition, a new test structure has been developed to measure an important parameter in alternating aperture phase shifting masks; the alignment between the chrome blocking features and the phase shifting regions etched into the quartz substrate. Simulation results are presented which demonstrate the capability of the test structure when used in a progressional offset array.**

I. Introduction and Background

Present advances in optical lithography have been achieved using techniques such as optical and process correction (OPC) and phase-shifting technologies. The photomasks using these methods are extremely expensive and complex to manufacture, which makes the ability to test and characterise the mask writing process very important. Typically the measurement and verification of advanced photomasks is achieved with optical or critical dimension scanning electron microscope (CD-SEM) methods that require expensive equipment. A cheaper, more repeatable and potentially much faster option would be to use well understood electrical test structures.

Previous work [1], [2] has described the design of an alternating aperture phase shifting mask, which includes a set of cross-bridge test structures [3]. These can be used to measure both the sheet resistance of the chrome blocking material and the electrical critical dimension (ECD) of the features on the mask. These results have also been compared with CD-SEM measurements and the following conclusions were drawn:

- The chromium is normally covered with a layer of chrome oxynitride which acts as an anti-reflective coating (ARC). This caused problems with electrical measurements which were solved by removing the layer.
- The variability of the sheet resistance measurements can be improved by increasing the dimensions of the test structures. The worst problems were found in some of the phase shifted Greek cross structures where the etching of the phase shifters adversely affected the symmetry of the measurement.
- The ECD was generally less than the designed linewidth and, in addition, the phase shifted structures were found to be electrically narrower than the binary structures.
- CD-SEM results showed the opposite, with the binary structures appearing narrower than the phase shifted structures with the same design width.
- Problems with charging of the sample in the CD-SEM led to low contrast and long testing times.
- The electrical measurements demonstrated much better repeatability than the CD-SEM.

The purpose of this paper is to answer a number of questions which were raised by the previous work and also to describe the development of a new test structure which will enable the measurement of any overlay error between the chrome features and the phase shifting elements.

II. Test Mask Measurements

The following issues have been raised by previous work on electrical test structures for phase-shifting mask characterisation [1], [2]:

1. How does the etching of the phase shifting elements affect the geometry of the narrow Greek cross structures?
2. Why do the the phase shifted lines appear to be electrically narrower than the binary structures but seem wider when measured with the CD-SEM?
3. Does the CD-SEM measurement technique which is used have an impact on the effect mentioned above?

A. Greek Crosses

There are two types of Greek cross included on the test mask, each with a different arrangement of dummy lines, and these are illustrated in figure 1.

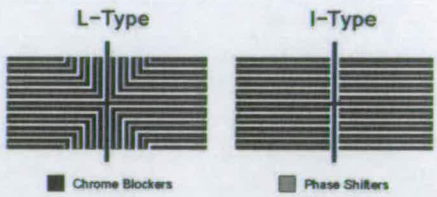

Fig. 1. Sections of the test structure layout showing the phase shifted Greek cross layout.

The L-type structures displayed significant asymmetry when electrically measured and, as dimensions reduced, an increase in the value of sheet resistance was observed. This approached 20% of the value measured on the other types of Greek cross structure of that size. These devices were imaged with an atomic force microscope (AFM) to help determine the geometry of the structures and to explain the observed effect.

The phase shifting mask is fabricated in a two stage process. First of all the chrome layer is patterned to form the blocking features and then the phase shifting areas are etched into the quartz substrate. The phase shifting regions overlap with the chrome features by 0.2μm and the ARC covering the metal is removed by the phase shifter etch process. A close up schematic diagram of the centre of a phase shifted, L-type Greek cross is shown in figure 2.

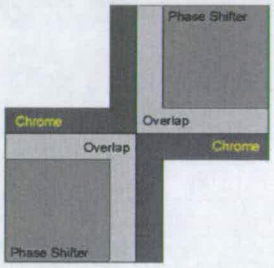

Fig. 2. Schematic layout of the centre of an L-type, Greek cross structure with arm width of 0.4μm.

It is understood that the process which is used to etch the phase shifting elements into the quartz will also etch the chrome oxynitride ARC, exposing the metal under the overlap. This process should not affect the geometry of the test structures but this mask has undergone a further processing step to remove the ARC which was causing probe contact problems during electrical test. This was achieved with a blanket wet etch in an aqueous solution of ceric ammonium nitrate and acetic acid. This etchant solution will also etch chrome and so it seems likely that the areas of metal exposed by the fabrication of the phase shifters will also be partly etched.

A.1 Measurements

Tapping mode AFM measurements were made on a Greek cross structure with the layout shown in figure 2. A 2400 × 2400nm scan of the centre of the cross is shown in figure 3.

It is possible to extract a cross sectional profile of the structure by taking a single line of the raw AFM data. This has been done at the positions marked "Line 1" and "Line 2" on figure 3. The data is scaled to give the correct range of heights and to remove artifacts such as slope. The results of this operation are presented in figure 4

It is clear from this graph that the etching of the phase shifter elements and the removal of the ARC has had a significant effect on the geometry of the metal features. The areas of chrome which were not protected by the ARC during the wet etch have been partially etched while the areas which were covered are less affected. The measurement of sheet resistance with a Greek cross depends on assumptions about the geometry of the structure [4], [5], which state that the material should be homogeneous in thickness. The results shown in figure 4 indicate that this is not the case for these L-type Greek cross structures. The sheet resistance results presented in [2] showed that there was an error in the values of R_s extracted from the narrowest L-type crosses which could not be corrected for by using the method described in [6]. The asymmetrical etching of these structures becomes more apparent as the dimensions reduce because the overlap between chrome and phase shifted areas has a constant width. The larger crosses are less affected by this effect and, although the asymmetry is still significant, it is possible to correct for it and extract an accurate sheet resistance.

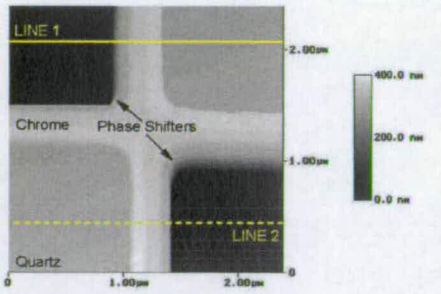

Fig. 3. 2×2μm AFM scan of a 0.4μm phase shifted Greek cross.

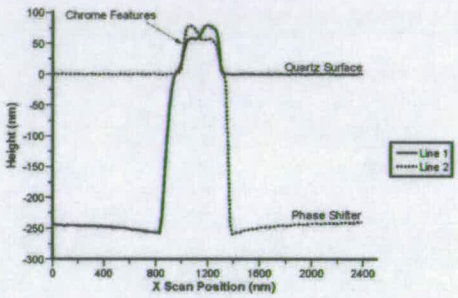

Fig. 4. AFM profiles extracted from figure 3.

A.2 Simulations

Current flow simulations using the 3-dimensional interconnect simulator Raphael [7] were performed in order to gain insight into the effects of the asymmetric geometries found in these structures. A plan view of a simulated

Greek cross corresponding to the test structure shown in figure 3 can be seen in figure 5.

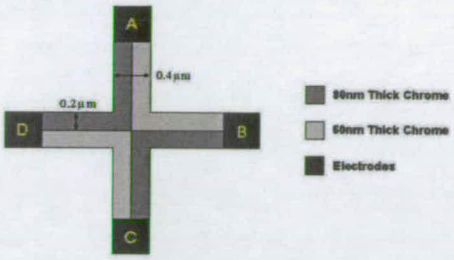

Fig. 5. Plan view of simulated Greek cross structure.

The thickness of the "unetched" chrome was set to 80nm while the "etched" chrome, corresponding to the overlap in figure 2, is 60nm thick. These values were derived from the AFM measurements presented in the previous section. The resistivity of the chrome was set to $2.3\mu\Omega$-m in order to give a sheet resistance ($\sim 28.5\Omega/\square$) for the un-etched chrome which is similar to the results of electrical measurements made on the mask.

In the simulations, a current is forced between two adjacent electrodes, A to B for example, and the voltage between the other two electrodes is measured. The simulation is then repeated with the current being forced at right angles to the first measurement, i.e. from A to D. The two results can be used to calculate both an estimate of the sheet resistance R_S and a figure for the asymmetry of the structure F_A [6]. A number of simulations were performed using cross structures with arm widths varying from 0.4μm to 1.5μm. The dimensions of the thinner material, representing the overlap of the phase shifter in the real structures, are fixed with a width of 0.2μm. The sheet resistance results from the simulations are presented in figure 6.

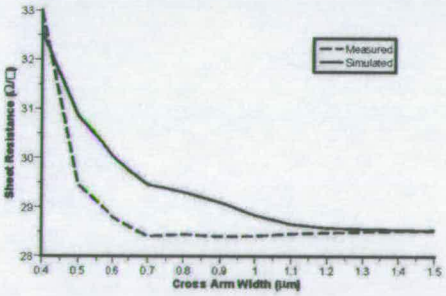

Fig. 6. Sheet resistance versus Greek cross arm width.

Although the results obtained from simulated structures with the largest and smallest dimensions are similar to the measurement results the simulations tend to overestimate the sheet resistance measured for the other cross arm widths. This is probably due to the fact that the simulated structures do not include elements of the real structure geometry such as the sidewall slopes and corner rounding seen in the AFM profiles. However the simulated structures do seem to model the asymmetry, caused by the phase shifter overlap, more successfully as can be seen from the asymmetry factor results in figure 7.

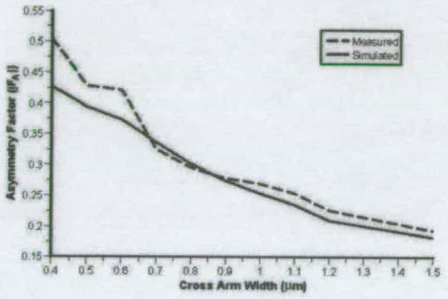

Fig. 7. Asymmetry factor (F_A) versus Greek cross arm width.

B. Bridge Structures

The results of AFM scans of the test structures can also help to explain some of the effects observed with the electrical linewidth measurements. Figure 8 shows AFM profiles of two bridge structures, one phase shifted and one binary. The results have been overlapped so that any difference in cross-section between the lines can be seen.

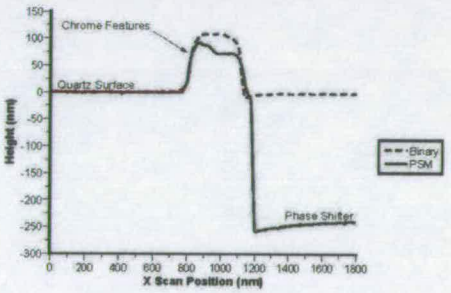

Fig. 8. AFM profiles comparing phase shifted and binary bridge structures.

It is clear from figure 8 that the cross sectional area of the phase shifted track is smaller than that of the binary line. This means that it will appear electrically narrower as was observed in [1], [2].

Unfortunately, this mechanism cannot explain the results obtained from the CD-SEM where the phase shifted

lines appeared to be wider than the binary features. This can be observed in a SEM image of part of a phase shifted test structure such as figure 9.

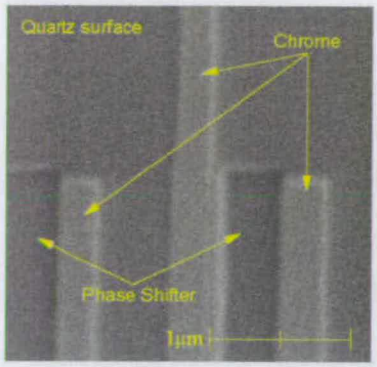

Fig. 9. SEM image of part of a phase shifted test structure with 0.4μm nominal feature size.

The intensity of the SEM signal is dependent on the number of electrons scattered by the sample surface. Metal surfaces and the edges of features scatter more of the electron beam and so these appear brighter in the SEM image. Figure 9 shows that the sidewall of the etched phase shift element gives a stronger signal than the edge of the chrome feature and makes the phase shifted line appear wider. Figure 10 shows typical intensity profiles taken over the three phase shifted lines and the single binary line shown in 9.

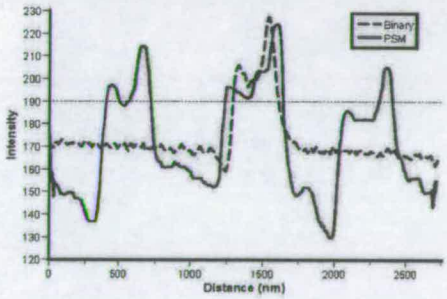

Fig. 10. SEM image intensity versus distance. The intensity has an arbitrary scale and is derived from figure 9.

A CD-SEM measurement is made by setting a threshold for the intensity and measuring the distance between two pints in the intensity profile at that threshold level. Using the profiles in figure 9 and an arbitrary intensity level of 190 the apparent widths of the middle features are ~400nm for the phase shifted line and ~310nm for the binary line. These results compare well with the CD-SEM results presented in previous papers where the offset between binary and phase shifted line widths was about 80-90nm for 0.4μm features. It is possible that the method used to extract the CD-SEM values could be altered in order to improve the measurement of phase shifting masks. For example, the thresholds could be defined at a different level for the side of the chrome feature which is affected by the phase shifter.

III. Alignment Test Structures

As has been described above, the phase shifting elements are fabricated by etching into the quartz (synthetic fused silica) substrate. The etch depth required depends on the wavelength of the light intended to be used with the mask, λ, and the refractive index of the substrate material. The etch depth required to give 180° phase shift is calculated using [8]

$$d = \frac{\lambda}{2(n-1)} \tag{1}$$

If the mask is intended for use with 248nm deep ultraviolet (DUV) illumination and $n_{quartz} = 1.51$ then the phase shifter depth should be ~243nm. The removal of this material will change the effective capacitance between two chrome lines on the mask. This effect can be used in a test structure to allow the measurement of the overlay between the chrome layouts and the phase shifters. Simulations of simple capacitive structures have been performed using the two-dimensional interconnect analysis software Raphael [7]. The simulated structure consists of two or more electrode elements on a quartz substrate with a gap between which represents the phase shifter. The actual test structure on the mask will be an interdigitated capacitor with hundreds of electrode fingers so the simulation should accurately model the lateral capacitance between two elements. Errors in this value will be introduced by fringe effects if there are too few electrodes and this is indicated by the results in table I.

TABLE I
Results of simulations of capacitive structures with different numbers of electrodes.

Number of electrodes	Capacitance between adjacent electrodes
2	2.894412×10^{-17} Fμm^{-1}
3	2.166128×10^{-17} Fμm^{-1}
4	2.129511×10^{-17} Fμm^{-1}

It was decided that the simulated structure with 4 metal electrodes should be used as this should give an accurate estimation of the capacitance without the use of a complex simulation. Unlike the normal alternating aperture structures on the mask, these capacitive test structures will have phase shifting elements between each pair of fingers. In addition there will be no overlap between the metal

features and the phase shifters when they are correctly aligned. This means that any misalignment will cause a reduction in the amount of quartz being etched between the electrodes. The simulation areas for three different alignments are illustrated in figure 11.

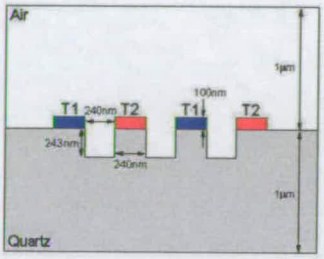

(a) No offset

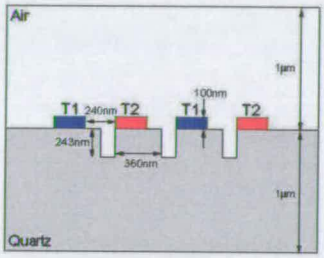

(b) Offset=120nm

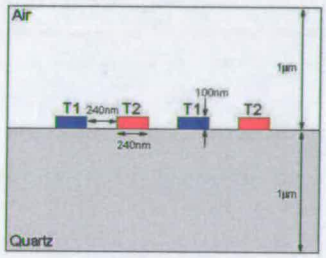

(c) Offset=240nm

Fig. 11. Examples of simulation areas used to model an interdigitated capacitor structure on a phase-shifting mask.

The four metal electrodes in the simulated structure are connected either to 1V (T1) or ground (T2), and so there are effectively three lateral capacitances. The offset was varied from -240nm to +240nm and the capacitance between T1 and T2 was extracted. The results of the simulations are presented in figure 12.

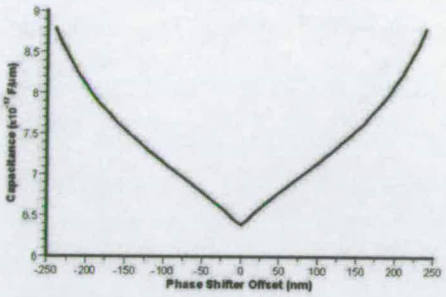

Fig. 12. Simulated capacitance plotted against phase shifter alignment.

The simulation results suggest that a progressional offset technique (POT) [9], [10] could be used to extract the degree of alignment error between the metal and the phase shifter elements. An array of the capacitive test structures would be fabricated on the mask with different amounts of in built misalignment. The test structure with the lowest capacitance would then indicate the actual misalignment. The next test mask to be fabricated will include a number of POT arrays consisting of nine capacitor structures with built in overlay errors ranging from -200nm to +200nm. The test structures have the same designed feature sizes as the simulations and contain a total of 2000 capacitor elements, each being 1000μm long. The simulation data can be used to estimate the actual capacitance of the test structures, assuming there is no misalignment, and this is shown in figure 13.

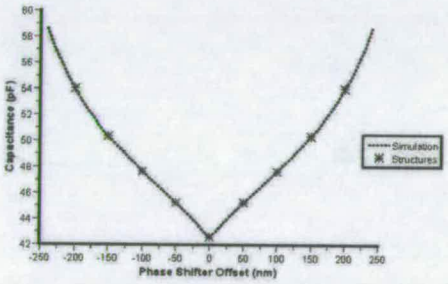

Fig. 13. Estimated capacitance of alignment test structures derived from simulation data in figure 12.

If there is an actual offset between the chrome features and the phase shifting elements then the results will be shifted away from zero and it should be possible to extract the value of the overlay error.

IV. Conclusions and Further Work

AFM scans were made of phase shifted, L-type, Greek cross test structures in an attempt to explain the results of sheet resistance measurements. The AFM results indicate that the removal of the anti reflective material during the fabrication of the phase shifting elements led to the metal features being etched during a further processing stage which removed all of the ARC. The result of this is that the structure is extremely asymmetrical and does not have the homogeneous thickness required of a van der Pauw structure. This effect depends on the overlap between the chrome and the phase shifters and, as the width of this was constant on the original test mask, the errors introduced increase as the dimensions are reduced. Simulations of these structures did not provide accurate modelling of the sheet resistance measurements across the whole range of features sizes. However, they did confirm that the geometry of the narrow, L-type, phase shifted structures causes measurement errors which cannot be corrected for using the normal asymmetry correction methods as was observed in previous papers.

AFM measurements of narrow bridge CD structures have also shown that the effect of etching the ARC has reduced the cross sectional area of the phase shifted structures leading to an error in electrical linewidth measurements. The phase shifted structures appear electrically narrower than the binary structures of the same nominal feature size because of this effect. Similar insight into the CD-SEM results was obtained from examining SEM images of binary and phase shifted structures. The effect of the phase shifter element is to make the chrome lines appear wider than the binary features of the same size. The next test mask will not require the removal of the ARC in order to perform the electrical measurements. This should reduce the effects of charging during CD-SEM measurement and allow further analysis of this problem.

A new electrical test structure based on an interdigitated capacitor has been developed which should allow the extraction of the misalignment between the chrome features and the phase shifted regions. Simulations of the structure have shown that it is suited for use in a POT array which allows the extraction of overlay error without the need for calibration of the capacitance measurement. A set of nine test structures with built in misalignments have been included in the layout for the next test mask. These will be measured when available in order to confirm the simulation results.

Acknowledgements

The authors would like to acknowledge the support of EPSRC (GR/S12838/01), Nikon and Compugraphics.

References

[1] S. Smith, M. McCallum, A.J. Walton, and J.T.M. Stevenson, "Electrical CD Characterisation of Binary and Alternating Aperture Phase Shifting Masks," in *Proceedings of IEEE International Conference on Microelectronic Test Structures*, Cork, Ireland, April 2002, pp. 7–12.

[2] S. Smith, M. McCallum, A.J. Walton, J.T.M. Stevenson, and Alan Lissimore, "Comparison of Electrical and SEM CD Measurements on Binary and Alternating Aperture Phase-Shifting Masks," *IEEE Transactions on Semiconductor Manufacturing*, vol. 16, no. 2, pp. 266–272, May 2003.

[3] M.G. Buehler, S.D. Grant, and W.R. Thurber, "Bridge and van der Pauw Sheet Resistors For Characterizing the Line Width of Conducting Layers," *J. Electrochemical Soc - Solid State Technology*, vol. 125, no. 4, pp. 650–654, April 1978.

[4] L.J. van der Pauw, "A Method of Measuring Specific Resistivity and Hall Effects of Discs with Arbitrary Shape," *Philips Research Rep.*, vol. 13, pp. 1–9., Jan 1958.

[5] L.J. van der Pauw, "A Method of Measuring the Resistivity and Hall Coefficient on Lamellae of Arbitrary Shape," *Philips Technical Review*, vol. 59, no. 8, pp. 220–224, 1958.

[6] M.G. Buehler and W.R. Thurber, "An Experimental Study of Various Cross Sheet Resistor Test Structures," *J. Electrochemical Soc - Solid State Technology*, vol. 125, no. 4, pp. 645–650, April 1978.

[7] Avant!, *Raphael Reference Manual, Release 2000.2*, 2000.

[8] M. D. Levenson, N. S. Viswanathan, and R. A. Simpson, "Improving Resolution in Photolithography with a Phase-Shifting Mask," *IEEE Transactions on Electron Devices*, vol. ED 29, no. 12, pp. 1828–1836, December 1982.

[9] J.A. Serack, A.J. Walton, and J.M. Robertson, "A Novel Device Structure for Studying Gate and Channel Edge Effects of IGFETs," in *Proceedings of IEEE International Conference on Microelectronic Test Structures*, Long Beach, USA, Feb 1988, pp. 67–72.

[10] A.J Chester, A.J. Walton, and P. Tuohy, "An Experimental Investigation of EEPROM Reliability Issues Using the Progessional Offset Technique," in *Proceedings of IEEE International Conference on Microelectronic Test Structures*, San Diego, USA, March 1994, pp. 218–222.